Size Regulation and Nonequilibrium Growth of Biological Tissues

by

Ojan Khatib-Damavandi

A dissertation submitted in partial fulfillment
of the requirements for the degree of
Doctor of Philosophy
(Physics)
in The University of Michigan
2019

Doctoral Committee:

Professor David K. Lubensky, Chair
Associate Professor Xiaoming Mao
Professor Mark Newman
Assistant Professor Qiong Yang
Professor Robert M. Ziff

"It is the unknown that excites the ardor of scholars, who, in the known alone, would shrivel up with boredom."

– Wallace Stevens

Ojan Khatib-Damavandi
ojan@umich.edu
ORCID iD: 0000-0002-1540-648X

To Maman Kooki,
who climbed the stairs with me despite her weak heart

Acknowledgments

There is no doubt in my mind that I could not have made it to this stage in my life if it weren't for the support and sacrifices of many wonderful people whom I've had the privilege of knowing. I would like to start by thanking my mother, the strongest person I know. She sacrificed a lot so I could focus on my studies; I appreciate you very much, mom. It would be negligent of me not to thank my grandmother as well, who was like a second mother to me. She was also one of the most giving persons I have ever known and will ever meet, and even though she passed away a few years ago, her presence in my life is undeniable.

I would like to thank my father. Exactly five years ago, I moved to the USA from Iran, and indisputably, his presence has been pivotal in anchoring me whenever I became close to feeling lost. Before moving here, I had almost no relationship with my siblings other than occasional summer visits. I wish I had, because they are amazing! Especially, my loving sister, whose support has given me the strength to keep going, against all the odds.

I would like to thank some old friends and some new ones. First of all, Arvin, my oldest and best friend. Our friendship has seen the test of time. He has always been there for me, from the moment I saw him in the fifth grade. And even now that we are ten thousand kilometers away, he is still present, despite his often terrible internet connection; for the 100th time Arvin, change your mobile service! I would like to thank Mahan and AmirAli who made college much more fun than it had any right to be. I would like to thank Marios, the first person I talked to when I arrived in Ann Arbor, my first friend in the US, and the best thesis buddy I could wish for; thank you for all the great memories! I would like to thank Christine, who has helped me overcome my anxieties and come out of my shell; I am forever grateful for your help! I would like to thank Michael, the Superman himself; going to the movies and chatting about Tolkien or Shakespeare over coffee with you has been very delightful.

Michael is also responsible for introducing me to dancing, which brings me to the folks at Swing Ann Arbor. They are an amazing group of people brought together by their love for Lindy Hop and Swing Jazz, and I am grateful that they have accepted me with open arms as one of their own. In particular, I would like to thank Val, who is not only one of the most compassionate people I've known, but also an awesome person to be friends with;

knowing you has been a real pleasure, Val! (Also, learning St. Louis shim sham with you was a blast!) I would also like to thank Katie for the super fun practices. Last but not least, special thanks to Sarah and Connor for being fantastic teachers; most of what I know about swing dancing, I owe to you guys!

Of course, I am forever indebted to my advisor, Prof. David Lubensky, who has taught me so much of what I know about different areas of physics. He has always provided great support when I needed it and I am grateful to him. Prof. Bob Ziff, my first advisor, has been a great mentor, and I greatly appreciate his support when I decided to transition to biological physics. To all the members of my dissertation committee, Profs. Bob Ziff, Mark Newman, Xiaoming Mao and Qiong Yang, I am thankful for being on my committee and for your helpful comments on my thesis. I would also like to thank Prof. Wolfgang Lorenzon for his mentorship during my Lead GSI tenure with him. And finally, special thanks to Prof. Pierre Leopold and his lab who have been wonderful hosts during my visits, and in particular Dr. Parisa Kakanj who taught me many things about biology with patience.

Lastly, I would like acknowledge support from NSF Graduate Research Fellowship for supporting my PhD studies and providing funds for my research so that I would not have to teach and could focus on my research and collaboration.

Of course, this is by no means a complete list and I apologize if I left anyone out. To all my friends, family and colleagues, I appreciate you!

Table of Contents

List of Figures

Figure

List of Appendices

Abstract

Growth is one of the most profound concepts in biology, shared among all living organisms from bacteria to human beings, and has had a long history in physics as well. One of the major open questions in biology regarding growth is how organs in a growing animal regulate and coordinate their sizes to ensure proper body proportions. In this thesis, we study size coordination and growth regulation in biological tissues from multiple angles using phenomenological models borrowed from nonequilibrium statistical physics, control theory and the theory of elasticity as well as image processing algorithms to analyze biological data. Motivated by a recent observation in the fruit fly *Drosophila* that a single hormone secreted by the developing organs is instrumental in keeping the bilateral symmetry of the fly wings, we first investigate coordination between left and right organs via chemical signaling. We show that there are limits to the ability of the signal to ensure successful left/right symmetry, suggesting that organ sizes are primarily set autonomously. We then discuss an experimental collaboration with the biology lab of Pierre Leopold in France. We explain our efforts in mounting and imaging adult *Drosophila* wings, and developing image processing algorithms to automate the wing segmentation to measure wing size asymmetry. We also outline a code based on the Procrustes analysis to quantify shape asymmetry and see whether or not wing shape is also affected in response to mutations that cause an increase in size asymmetry between left/right wings. Finally, inspired by our analytical conclusion that final organ sizes are primarily set autonomously despite growth being an intrinsically noisy process, we look at noisy growth of individual tissues subject to mechanical feedbacks to understand what the implications of noise are in a growing tissue. We show that even the simplest model of noisy tissue growth exhibits a surprisingly rich behavior. For instance, we find that the growth displays power law correlations, and soft modes that lead to large variations in the size of marked clones of cells. Our models set the stage for future experimental and theoretical studies of nonequilibrium tissue growth in biology and physics alike.

CHAPTER 1
Introduction

Why might a theoretical physicist study biology? I would say, because there is a certain kind of beauty in biology, the kind that is not only aesthetically pleasing but also fascinating and almost magical. So, it is only natural for our curious minds to draw us towards understanding animate objects the same way that it draws us to understanding, say, the nature of gravity. In other words, studying biology as a theoretical physicist merely means approaching biological questions with a physicist's mindset.

This is indeed an exciting era for theoretical physicists to work on biological problems. Nowadays, the advancements in imaging, molecular biology and genetics have granted us the power to manipulate different model organisms such as the fruit fly *Drosophila melanogaster*, the roundworm *Caenorhabditis elegans*, and the zebra fish *Danio rerio* among others in order to study the functions of different genes and proteins, cellular processes, interactions between cells and their surroundings, and so on, thus providing us with an ever expanding library of biological data and questions to tackle.

Although given the complexity of living systems, it might seem as though our only contributions to biology can be in doing numerical simulations or detailed modeling of biological processes that involve a large parameter space of interacting components (e.g. [7]), there is arguably great value in taking a phenomenological approach by building simple *generic models* that attempt at describing the system in a coarse-grained manner.

It is well established that living organisms are complex, i.e. they are greater than the sum of their parts. This means that for example by mixing up all the content found inside a cell, we would most likely make goo and not a cell! Therefore, a detailed microscopic model probably will not give us a good intuition about biological principles that cause these molecules to self-organize into a living system, and more importantly will likely not be tractable analytically at all, forcing us to resort to numerical studies. However, all hope is not lost, because not all details matter 'equally' and we can indeed gain insight into a system without knowing every single detail about that system.

Two famous examples of the power of generic models include Michaelis-Menten kinetics

[8] and pattern formation by Turing instability [1] [9]. Michaelis and Menten were able to explain the saturation of the production rate in an enzyme driven reaction by proposing an intermediate reaction where enzyme binds the substrate into a complex, the existence of which was proven thirty years later [10].

To explain the pattern formation in animal development, Alan Turing proposed that by having a two component reaction-diffusion system where one component diffuses more slowly that the other, instability driven patterns can arise. He called these diffusing chemicals morphogens. Even though he did not take into account the complex interaction between morphogens and cells, the idea that patterns can form from diffusing molecules was revolutionary and has since been attributed to different cases of pattern formation in different animals [11].

These two examples highlight three features that distinguish such phenomenological models from microscopically detailed models: (i) These models are not specific to any particular system (Michaelis-Menten kinetics does not apply just to one particular reaction, and even more so, Turing's model applies to the process of pattern formation in general). (ii) They rely on mainly macroscopic observables and only a minimal set of microscopic details. (iii) Their basic assumptions predict the necessary existence of an unobserved detail[2]. Moreover, the fact that coarse-grained models can work attests to an inherent simplicity and universality at the heart of the complexity and messiness of biology: many fundamental components, processes and interactions are shared among most living beings. Simple toy models have indeed uncovered motifs that are repeated in different systems. Examples include robustly achieving a desired steady state through negative integral feedback [12, 13] and exhibiting multistability via positive feedback [14, 15]. All in all, it is valuable to strive for a simple phenomenological approach that gives us the power to tackle fundamental questions about biology that are not necessarily specific to a certain organism and make general predictions about biological mechanisms.

An area where this phenomenological approach can be particularly helpful is developmental biology. What is fascinating about development is that it is a purely emergent phenomenon. In other words, there is nothing in the DNA that explicitly tells the animal how it should look like. Genes in the DNA are responsible for the production of different proteins and the interactions between them, effectively determining cell-cell communica-

[1] Notably, both cases happened before much was known about the microscopic details of biological processes. For reference, Watson and Crick discovered the double helix structure of DNA in 1953.

[2] Note that we are not claiming that heavily detailed models do not have predictive power. However, such models often become black boxes with results that are hard for humans to interpret. For instance, it often is not easy to know by looking at a detailed model what sort of parameter changes lead to qualitatively different behaviors.

tions. From the ensuing spatio-temporal network of interactions on different scales emerges a self-organized living organism. Then, clearly studying each individual part will not provide a satisfying and sufficient answer to, say, how a chicken emerges from an egg. Thus, developmental biology is an exciting area for physicists to employ phenomenology in order to gain insight into the most basic biological principles that are required for proper animal development.

One of the central questions in developmental biology is how organs regulate and set their sizes leading to an exceptionally well-proportioned animal. This is in fact the question from which this thesis was born. To answer this question, we teamed up with the biology lab of Pierre Leopold at the Curie Institute (previously at the University of Nice) in a collaboration and used phenomenological models to address the problem of growth and size regulation in development. Before delving more deeply into our findings, it is important to give some background on organ size determination and tissue growth.

1.1 Organ Size Control

Leonardo da Vinci created the Vitruvian Man circa 1487, a drawing that underlined the proportional relationship of different parts of human anatomy, echoing da Vinci's idea of a universal design. He was most likely not the first to notice how well-proportioned and symmetrical body parts are, but perhaps the first to attempt at quantifying this symmetry. Since him, scientists have consistently shown interest in symmetry and proportionality in nature. For instance, it is well known that the golden ratio shows up in different parts of nature such as the spiral patterns in seashells or the patterns of seeds in a sunflower. Notably, one of the early comprehensive quantitative studies of proportionality of growth was done by D'Arcy Thompson in his momentous book, *On Growth and Form* [16], which is now hailed for its fundamentally physical and mathematical approach to the problem of growth, something rather unheard of at the time of its publication in 1917. In the more recent years, advancement of experimental techniques has lead to a renewed interest in understanding the principles behind the observed symmetries and size control in biology.

As one would expect, size control is not limited to the scale of organs but exists at even subcellular scales. For instance, some organelles inside a cell alter their sizes based on the cell size [17]. Indeed, changes in organelle size can be indicative of disease progression, which suggests that sizes of subcellular structures can be functionally important. Cell size has been shown to scale with the genome size [18]. While cells of different types show a very wide range of sizes (for instance, in humans, blood cells are about 10 μm while neurons can be larger than 1 meter in length [19]), cells of a given type in a given organism must regulate

their sizes to ensure functionality. Cell size is mainly regulated by a balance between cell growth and division [20]. There have been several signaling pathways and genes identified that regulate cell growth and proliferation in developing organisms [21,22]. Yet interestingly, cell size is regulated both autonomously [23] and non-autonomously in organs [24]: While in some organisms like *C. elegans* cell number and size determines the size of the organism, in most animals cell size and number are regulated by the size of the organ, which is often determined by other factors, so that repressing cell division for instance would lead to larger cells such that the organ size is untouched [19, 24]. Organ and body size regulation by extrinsic and intrinsic mechanisms such as nutritional signals, growth factors, morphogens, and local cell-cell interactions have been studied in different organisms [21, 24–27].

Even though many of the molecular components that are involved in size control are known today, it is still not clear how these components collectively lead to a well-proportioned animal. When talking about a well-proportioned organism, perhaps the first thing that comes to mind is the existence of some kind of symmetry, be it bilateral symmetry as in butterflies or human face, dihedral symmetry as in starfish and so on. For instance, it is widely reported in the fruit fly *Drosophila* that the left and right wings of the same fly do not defer in size by more than about 1% [1,28,29] (Fig. 1.1A). Similarly, it has been measured that vein patterns in the wing are reproducible to within a single cell size, suggesting high symmetry in shape in addition to size [30]. The small asymmetry is due to intrinsic and environmental variations that commonly occur during development, and is called *fluctuating asymmetry* (FA). FA is a measure of deviations from perfect symmetry where a particular symmetry is expected [31]. Organisms seem to buffer fluctuations very well leading to a low FA. Importantly, variations between different individuals are significantly higher that the intra-individual variability [32].

FA is a manifestation of the fact that most processes in biology are noisy. Stochasticity stems from the fact that processes inside a cell involve discrete and thus inherently random reactions. Indeed, gene expression is a stochastic process [33]. One of the major consequences of noise is the phenomenon of translational bursting wherein proteins are produced in pulses [34, 35]. Bursting at the level of RNA transcription has also been observed in bacteria and mammalian cells [36,37]. Another example of a noisy process is protein partitioning, meaning daughter will likely not get the same number of proteins [38]. Cell division also involves a level of stochasticity [39].

Yet the high level of symmetry and reproducibility observed in organisms implies that there are regulatory mechanisms to buffer noise. A question remains, however: Do organs autonomously attenuate noise and reach the correct final form, or do they somehow communicate with each other as they grow? Classic transplantation experiments have indeed shown that organs have at least a rough idea of what size they want to be. A limb transplanted

from a salamander onto another salamander retains the same growth rate as the donor and can end up with a different size than the recipient [40]. Dissected wing tissues from a larva that are cultured inside the gut of an adult fly end up with similar sizes to the uncultured wing tissue even though they grow in very different environment that lacks many of the developmental signals that the wing would receive inside a larva [41]. Similarly, baby rat kidneys cultured in the bodies of adult rats autonomously grow to wild type size [42]. These experiments suggest that organs have an idea of the size they want to be, which we call the *target size*.

It is noteworthy, however, that some animals never stop growing but organ growth slows down with aging. This pattern of growth is called *indeterminate growth* [24]. For instance, most fishes such as the zebra fish fall into this category. Even in animals with determinate growth, there could be parts of the body that never cease to grow, e.g. nose and ears in humans [43].

In animals with determinate growth, the existence of a target size notably does not exclude the possibility and need for some kind of a feedback mechanism. For instance, in the case of flies, the transplantation experiment has an error of about 10%. Even accounting for experimental errors, is having an autonomous idea of a final size enough to ensure the observed 1% asymmetry? Moreover, there have been experiments that show that at least in response to extreme growth disturbance of one organ, other organs modulate their growth and developmental timing is slowed down for the affected organ to 'catch up' [44–46].

Another piece of the puzzle was discovered in 2012 independently by the labs of Pierre Leopold (our collaborator) and Maria Dominguez, who found that a single gene in *Drosophila* called *dilp8* is responsible for inducing a delay in pupariation (the point at which growth stops and the fly starts transitioning from larval to pupal stage), thus allowing imaginal discs (larval precursers to adult fly organs) to reach proper sizes [1,47]. The way it works is that a disc whose growth is in some way impaired secretes the hormone Dilp8, which in turn down-regulates ecdysone, the hormone that promotes transitioning from larva to pupa. Moreover, it was discovered that knocking out *dilp8* causes a significant increase in adult wing area FA (Fig. 1.1B) [1]. Later experiments further confirmed that Dilp8 slows down the growth of discs at least in response to severe growth perturbation to one disc [46]. The question that remains is whether *dilp8* plays any role in disc size coordination in normal physiological conditions, where there are no growth perturbations such as neoplastic growth [47], damages to a disc [48], or inhibiting disc growth by knocking down ribosomal proteins [46], all of which are known to trigger stress responses from the cells. There is indeed some experimental evidence that hints at the possibility of feedback in normal conditions. Boone et al. have found that other than being involved in stress response pathways, *dilp8* is also a target of

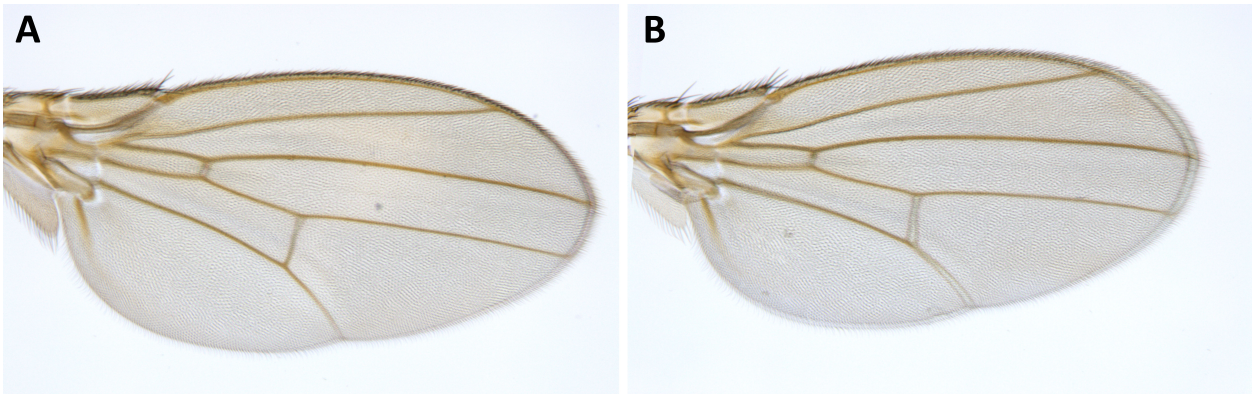

Figure 1.1: Left and right wing of the same fruit fly overlayed. Preparation and imaging of wings are discussed in Chapter 3. (A) Wings of a wild type fly. It is really hard, if at all possible, to see a difference in most wild type pairs. (B) Wings of a *dilp8*–/– fly. Here, the difference is more pronounced and clearly visible. There are some pairs with even more area difference (see e.g. [1, 2]).

the transcription co-activator yorkie (Yki) [2]. Yki is known to promote growth of imaginal tissues. On the other hand, ecdysone, which is down-regulated by Dilp8, is known to promote growth of imaginal discs [49].

This all suggests that Dilp8 may be involved in a feedback loop, as its secretion rate is a readout of disc growth rate and it can also inhibit the growth rate by down-regulating ecdysone. There are other unanswered questions as well. For example, it is not known if wings in *dilp8*–/– mutants have a higher FA in shape compared to wild type flies. Also, there is no information yet regarding the FA distribution in different genotypes. Is the FA distribution in *dilp8*–/– mutants just wider than in wild type or, say, it has a longer longer tail? We address these open questions about *dilp8* further in Chapter 3.

What is exciting about Dilp8 in a broader sense than its specific function in *Drosophila* is that it suggests that organ size coordination may be achievable via a single endocrine signal. Therefore, inspired by the example of *Drosophila*, we asked a general question: What are the possible mechanisms of organ size coordination using a single coordination signal? To answer this question we built a phenomenological model of noisy growth of organs and studied different coordination scenarios and their consequences. A crucial difference between our model of organ growth and those that have come before is the existence of a target size. Previous models have usually included a decaying growth rate [50], so even though the dynamics reaches a fixed point, this fixed point is dependent on initial conditions, whereas our model includes a target size independent of other parameters as a fixed point. This target size can indeed depend on local patterning genes or systemic and nutritional signals [21, 25], which we do not include in our model for simplicity.

In Chapter 2 we demonstrate that there are severe limitations in coordination using a single chemical signal. In particular, we show that a feedback on growth rate (as seems to be the case in flies) is also the most viable form of feedback but that it fails at correcting possible errors in target sizes, i.e., if organs infer their individual target sizes incorrectly, feedback cannot help improving the organ symmetry in adults. This unfortunate conclusion suggests that organs may have autonomous error correcting mechanisms that help them to individually specify their sizes properly. We were then motivated by this conclusion to look at growth of individual tissues and understand how they locally regulate their growth. We discuss this in the next section.

1.2 Growth of Biological Tissues

In the previous section, we suggested the idea of a target size that each organ can reach independently of others. This immediately begs the question: how does a growing tissue autonomously stop growing? In the past several years, there has been a large body of work dedicated to this very question. A major step towards answering this question was taken by Boris Shraiman in 2005, who proposed a mechanism for growth regulation via mechanical feedbacks [51]. Then, it can be inferred that a morphogen gradient would lead to growth arrest if cells at the boundary an epithelial tissue (a 2D layer of cells, e.g. wing disc in fruit fly larvae) stop proliferating once the morphogen level they see drops below a certain threshold. The reason is that the arrest of cell proliferation will lead to a build up of mechanical stresses in the middle of the tissue. If this stress field then feeds back on the growth rate, after some time the growth completely stops [24]. This hypothesis also suggests that the length scale of organ sizes might be determined by the length scale of the morphogen gradients. There have been many experimental, analytical and computational studies ever since to examine this hypothesis, including whether or not mechanical feedback can lead to a unique final size (e.g. [52–54]). One notable example is a study by Ranft et al., who showed that in a growing elastic solid, if the tissue responds to mechanical stresses by cell division or death, the stress tensor relaxes so that the tissue effectively acts like a viscoelastic fluid on long time scales [6].

But given that growth is intrinsically noisy, what are the implications of noise for tissue growth? If a tissue is to reach a specific target size with a high precision, it must be able to buffer noise in growth. It turns out that this question has not been explored in great depth before. In particular, not much is known about the interplay between stochasticity and mechanical feedback in growing tissues. Ranft et al. have briefly looked at noisy dynamics of tissues at homeostasis, the state at which cell division and death balance each other out,

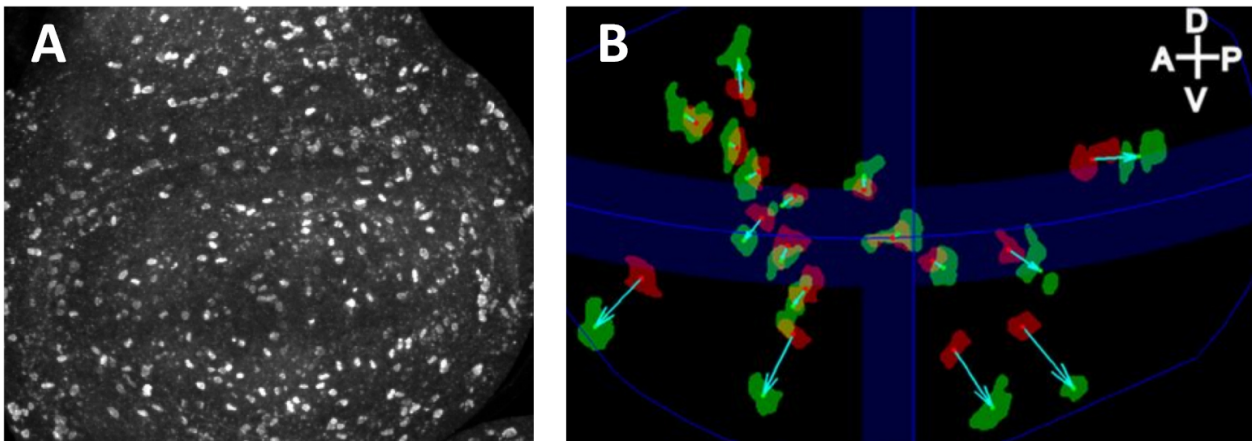

Figure 1.2: Signatures of noisy tissue growth (A) Taken from [3]; mitotic cells in *Drosophila* wing disc show clumping. (B) Taken from [4]; dynamics of clones in *Drosophila* wing disc. Each clone at n earlier time point (red) is connected to the same clone at a later time point (green). After some time clones grow to different extends and change shapes.

but not in the more general case of growing tissues.

Experimentally, there have been several studies probing noisy tissue growth. For example, cell density variations have been studied in culture (e.g. [55, 56]) and labeled clones of cell have been used in various experiments (e.g. [4]). Clones are labeled and genetically identical cells that share a common ancestry, enabling us to study the dynamics of a part of the tissue as the tissue grows. For example, looking at images of a a snapshot of mitotic cells and time evolution of clones in growing wing disc clearly shows some stochasticity (Fig. 1.2). We ought to be able to then say something about the statistics of mitotic cell density or, say, size distribution of clones.

As a first step towards understanding noisy tissue growth, we studied a simple model to attempt at answering these basic questions. For this purpose, we assumed that the tissue is a 2D elastic solid. A solid description is valid when there are no cell rearrangements in the tissue. This is definitely true for plants [57]. Even though many epithelial tissues show significant cell rearrangements, some like *Drosophila* wing disc have been shown to fit the solid description to a good approximation [58]. Therefore, for the rest of this section, we focus on growth of elastic tissues (we will discuss the validity of this assumption in more detail in Chapter 4).

Deterministic growth of elastic tissues has been studied in depth theoretically. One formalism that is often used to describe volumetric growth of elastic materials is called morphoelasticity, which is an extension of finite strain theory of elastic deformations [59] and formally similar to stress dependent plastic deformations [60]. It has been used to study buckling of morphoelastic filaments [61], instability of growing tissues [62], and growth and

remodeling of heart and bone tissues [63]. This formalism asserts that the deformation gradient tensor, the map from the initial state to the current state, can be decomposed into two components: a growth tensor G followed by elastic deformations. The principal components of G determine tissue's preferred dilation locally, i.e. they tell us by how much the tissue wants to grow in different directions locally to remain stress free. The tissue then has to elastically deform to be as close to the preferred grown state as possible. However, since G can end up being incompatible with the Euclidean space, tissue deformations may not be able to totally cancel out the local mass increase, leading to mechanical stresses to build up.

It is worth noting that another formalism that is sometimes used is called the target metric formalism, which has been shown to be equivalent to morphoelasticity. In this formalism, instead of the growth tensor G, the metric $\bar{g} = \mathrm{G}^{\mathrm{T}}\mathrm{G}$ is considered as the preferred metric after dilation [64]. This formalism has in particular been used to design and engineer elastic materials that would deform into a desired shape after dilation due to, say, temperature increase [65].

In Chapter 4, we start from the morphoelasticity formalism and consider a very simple model of nonequilibrium growth of elastic tissues to make predictions about experimentally accessible such as density-density correlation functions and the variance of clone size. We find that this simplistic model produces rich and surprising results. Even though the results do not in obvious ways help us understand how tissues buffer noise to stop growing at a specific size, this model can act as a first step towards more biologically accurate models, models that include effects of morphogens and anisotropic growth for example.

Our study of noisy tissue growth can be of value to the physics community as well. Growth has been studied extensively in physics. Particularly, nonequilibrium growth of interfaces, which often exhibits fractal patterns, have been of interest [66–68]. The most famous model of interface growth is arguably the KPZ equation [69]. KPZ equation is a great example of a generic model that was built purely by symmetry arguments, thus it should not come as a surprise that the KPZ equation has been used to successfully describe phenomena with completely different microscopic details such as combustion of paper [70], growing interface of bacterial colonies [71], turbulent liquid crystals [72], and the patterns of coffee rings [73]. Another notable example is diffusion-limited aggregation (DLA), which has been used to describe a variety of systems from particle aggregates [74] to urban structure [75]. Nonequilibrium growth of biological tissues can be seen as a new class of growth problems encompassing rich properties, waiting to be discovered.

1.3 Organization of the Thesis

This thesis is the collection of my PhD research under Prof. David Lubensky and involves a collaboration with the biology lab of Pierre Leopold in France, for which I have travelled to France on two occasions and taken part in experimental and imaging endeavors in addition to the main focus of my work, the theory of nonequilibrium growth and size regulation in biological tissues. Our goal in our modeling, in the same vein as the discussion at the beginning of this chapter, is to provide generic models of organ size coordination and growth regulation as a search for basic principles behind these mechanisms and to explore different consequences of our simple assumptions. The thesis has been divided into three semi-independent parts: (i) theoretical treatment of size coordination between organs, (ii) experimental and imaging aspects of size coordination in *Drosophila* wings, and (iii) growth regulation at the tissue level.

(i) In Chapter 2, as briefly discussed in Section 1.1, we look at the possibility of size coordination between organs by a single chemical signal. In particular, we will look at the most basic forms of feedback that can potentially exist in biology, namely proportional and integral feedback on growth rate and on absolute size, in each case examining the experimental signatures and potential issues. Moreover, we consider the most viable feedback mechanism in the case of *Drosophila*, which is proportional feedback on growth rate, and make predictions about different genetic manipulations. We will see that none of these feedback models are good candidates to correct errors in target size, suggesting that organ autonomous mechanisms also should be at play.

(ii) In Chapter 3, which focuses on our collaboration with the Leopold Lab, we look at the experimental and imaging side of organ coordination in the context of *Drosophila*. The chapter discusses the experimental procedure for mounting adult *Drosophila* wings on slides for imaging, and two MATLAB codes that we have used to quantify size FA and wing pattern FA of *Drosophila* wings in wild type flies and *dilp8*−/− mutants. Even though size FA can be easily measured by manual segmentation, it is a tedious and slow task, and prone to errors. This is particularly troublesome because we would ideally want to learn about the size FA distribution in different genotypes which means that we need many measurements of wing areas. To circumvent these issues, we automate this process using an image analysis algorithm. Moreover, to quantify shape FA, we look at the vein patterning and specifically the vein crossings on the veins. We present a code to identify vein crossings and used the Procrustes transformation to remove differences in size or rigid rotations and translations, and to isolate variations in vein patterns. This method allows us to quantify pattern FA.

(iii) In Chapter 4, we shift our focus towards growth and regulation at the tissue level as

a first step towards understanding autonomous size regulation in tissues such as *Drosophila* wing disc. As briefly discussed in Section 1.2, we look at the simplest case, where we will take the tissue to be an infinite 2D elastic solid with periodic boundary conditions. With this basic model, we study different measurable quantities like density-density correlation functions and the variance of clone size. What we discover is that surprisingly, density correlators show a power-law in space similar to inflationary models of cosmology where quantum fluctuations in the early universe lead to formation of large scale structures [76]. Because of this resemblance, we call our model *inflationary embryology*. We also find that our model exhibits two soft modes of growth. These are modes that do not generate any stress and are allowed to grow diffusively. We show that these modes have important consequences for dynamics of clones. Our model is the first step towards understanding noisy tissue growth and autonomous growth regulation in more specific biological contexts.

Finally, even though the contents of these chapters are related and tell a story on a whole, we have tried to give enough background information in the Introduction section and sufficient conclusions in the Discussion section of each chapter so that each of them can stand on its own merits independent of others. In some ways, each chapter in this thesis is like an organ of this body of work. Similar to how we think organs may function during development, each chapter is in a way autonomous, but there is still cross-talk between them.

CHAPTER 2

Organ Size Coordination by Chemical Signaling

Ojan Khatib Damavandi and David K. Lubensky
Department of Physics, University of Michigan, Ann Arbor, Michigan 48109-1040, USA
(Manuscript in preparation for Journal of the Royal Society Interface)

2.1 Introduction

One of the biggest open questions in biology is how animals set the sizes of their organs and how or whether organs coordinate their growth to lead to a a correctly proportioned animal at the end of development [77]. For instance, in the fruit fly *Drosophila melanogaster*, the left and right wings of the same fly rarely differ in surface area by more than 1% [1, 2, 29, 32] and the variability in wing shape is very low [30, 78]. Length measurements of left and right mouse forelimbs and hindlimbs show similar results [45].

In the recent years, there have been many new experimental discoveries regarding the underlying molecular components of organ size determination [21]. However, not much progress has been made into the mechanisms by which these components ensure proper organ sizes. In this chapter, we explore basic models of organ growth and coordination involving a single chemical signal and study the limitations of organ coordination and in particular, whether coordination can on its own ensure the exceptionally low asymmetry observed between left and right organs.

This small intra-individual asymmetry is due to intrinsic fluctuations present during growth and is often quantified by the so-called fluctuating asymmetry (FA) index [31, 32, 79–83]. FA refers to the difference in size or shapes due to intrinsic sources of noise of otherwise symmetrical organs [84–86] and can give us useful information about the amount of asymmetry in different genetic backgrounds or environments. The high precision in size control observed in animals and the low FA in their features is somewhat surprising given that often morphogenesis is a noisy process [87]. Could it be that each organ autonomously

regulates its growth precisely in such a way that all organs independently reach proper relative proportions? Or are there potential inter-organ coordination mechanisms to buffer errors in individual organ growth and ensure correct body proportions?

There is indeed evidence for autonomous organ growth, and existence of a 'target size' — an intrinsic size that an organ will reach independently of other organs — in animals ranging from fruit fly to salamander [40–42]. These classic transplantation experiments suggest that each organ has an idea of what size it wants to be. Furthermore, there has been evidence to suggest that organs have a control on their size and not necessarily their cell number. For instance, slowing cell division in a compartment of wing imaginal discs (precursor to adult wings in larval stage) in *Drosophila* leads to fewer cells in the compartment but the cells become larger and compartment size is unaffected [88]. This target size can in fact, and presumably does, depend on nutrition and environmental effects [21, 25]; organs read systemic signals related to these clues and determine their target size accordingly. We also note that even though organs in many organisms do stop growing, in some animals, such as lobsters and most fishes, growth never stops, rather it slow down as the animal ages but is never fully arrested [24, 43].

But is the existence of a target size enough to ensure correct final sizes to within a few percents as observed (e.g. 1% for adult fruit fly wings)? One could imagine that each organ may estimate its target size with some uncertainty, which can lead to high asymmetries if errors in relative target sizes are large. Even if each organ perfectly estimatees its target size, organs still may end up with large size differences if they are not allowed enough time to reach their respective target sizes. This could particularly be an issue for fruit flies which are known to have a very fast development, therefore potentially preventing organs from reaching their desired sizes before maturation, when growth stops.

Nonetheless, development is extremely robust against environmental variations, suggesting that some form of a feedback mechanism may be present during development to assist organs to coordinate their growth. A feedback mechanism can inform each organ of the developmental stage of others, thus helping organs modulate their growth rate accordingly. There is in fact evidence of coordination [26, 89–91]. Catch up growth has been observed in zebra fish inner ear development [92]. In *Drosophila* and mice, disrupting growth of an organ leads to a systemic growth rate reduction in other organs [44–46]. Coordination has even been observed between different compartments of *Drosophila* wings [46, 93].

The *Drosophila* example is particularly interesting as it was observed that knocking out the gene *dilp8* (responsible for the endocrine hormone Dilp8) in fly larvae results in an increased FA in adult fly wings [1, 2, 29]. Notably, even though it is not the first gene involved in buffering noise [28, 32], it is the first responsible for a secreted factor that has an

FA phenoype. Moreover, damaging or slowing down the growth of one imaginal disc in larva results in elevated levels of *dilp8* and increased secretion of Dilp8 hormone by the damaged disc, which in turn delays pupariation (the end of larval development and the onset of pupal stage) and slows down growth of uninterrupted discs so that the damaged disc can heal and catch up [1, 46–48, 94]. Thus, in *Drosophila*, Dilp8 is a natural candidate for a coordinating signal. What is less clear is whether Dilp8 is involved in coordinating organ sizes during normal physiological development when there is no significant stress on any of the discs.

Size coordination between organs has been studied before. One particular example is the notion of competition for limited resources observed in insects and bacteria [95–100]. However, at least in steady state, these limited resources mechanisms seem to only set a bound on the final size such that one organ could become large at the expanse of others [101]. This would lead to higher FA and thus makes these models less desirable for our study.

Here, inspired by Dilp8 in *Drosophila*, the question we tackle is whether organs can coordinate their growth by a single endocrine signal secreted by the organs themselves during *normal* development; in particular, we specifically exclude situations where one or more organs have been strongly perturbed so that they activate stress response pathways that are inactive in healthy, wildtype animals. Our primary focus is on coordination between left/right organs that show bilateral symmetry (e.g. fruit fly wings). Importantly, we build our models with the assumption that organs have an intrinsic target size, which suggests that organ growth slows down and stops eventually. This is in contrast with previous models that have assumed a growth rate that decays exponentially in time [5, 50, 102]. The issue with that assumption is that the steady state organ size will then depend on the initial conditions, which is incompatible with the idea of target size.

The organization of the chapter is as follows: first, we give an overview of the general scenarios of size coordination that we will consider for our study, pointing out their possible biological origins in Section 2.2. Then, in Section 2.3, we study these different cases individually in detail, discuss their major biological implications and explore their potential issues. Finally, in Section 2.4, we apply our models to the specific example of Dilp8 in *Drosophila*.

2.2 Scenarios of Growth and Coordination: Overview

In this section, we present an overview of the different scenarios of growth and size coordination in pairs of bilaterally symmetric growing tissues via a single endocrine signal (summarized in Table 2.1). In Section 2.3, we provide mathematical descriptions of these cases and discuss the main experimental consequences and of each model and their potential issues. Our main assumptions are:

(I) Organs have an idea of an asymptotic target size so that given enough time their growth will stop at this autonomously decided size at steady state.

(II) Organ growth completely stops at a specific developmental checkpoint, which we call the maturation point (e.g. pupariation time in *Drosophila*), before the asymptotic steady state is reached.

These assumptions are motivated by *Drosophila* development but have been observed in other organisms as well [43]. Throughout this section, we will frequently talk about the "coordination signal," by which we mean a hormonal signal that is secreted by both organs that helps in coordinating their sizes, and not, for example, a feed forward signal from the body. In order to understand the basic possibilities in the simplest context, we focus here and in the rest of this chapter on cases where one coordination scenario is predominant, but it is of course also conceivable that one animal might avail itself of multiple mechanisms (e.g., both controlling the timing of the maturation point and feeding back on organ size throughout growth).

2.2.1 No Coordination (NC)

The first possibility of coordination is of course that organs do not coordinate their growth at all, at least in normal physiological conditions. We call this scenario the 'NC model.' In this scenario, there may still be a hormone that only acts as a coordination signal in response to severe growth perturbations. But in normal conditions, the only signals each organ would receive are systemic ones such as nutritional and maturation signals, and the coordination signal is either not secreted or is only involved indirectly with processes such as homeostasis and housekeeping in each organ and not in any direct way involved with coordination between them. This implies that organs set their target size independently with high precision and, moreover, have enough time to reach that target size, or else FA would be high.

2.2.2 Timing-only (T)

Another possibility is that the coordination signal is only involved in delaying the timing of maturation long enough for the organs to come close to their target sizes. This scenario, similar to the NC model requires organs to have the same target size but relaxes the condition on timing. We call this hypothesis the 'T model.' Here, the hormone would need to down-regulate the secretion of some maturation signal (e.g., ecdysone in *Drosophila*), to delay the onset of maturation long enough for organs to grow to their proper sizes.

2.2.3 Continuous Feedback on Absolute Size (FS)

The coordination signal, secreted by the organs into the blood, may be involved in a continuous feedback loop instead of controlling only the timing of the maturation point. Even though the signal may simultaneously feed back on organs and delay timing of maturation, the simplest assumption is that in normal conditions signal only is involved in a feedback mechanism and only in response to severe growth disruption it may delay maturation.

First, let us assume that the coordination signal feeds back on errors in the absolute size of organs. Biologically, to have feedback on absolute size, we will show that organs need to secrete a hormone at a rate proportional to their size. Simultaneously, and more problematically, the cells in the organ need to 'know' the size of the organ, which could be achieved for instance by a constant amount of another chemical confined to the organ that is diluted as the organ grows, or perhaps by measuring the steepness of a morphogen gradient. As we show later, since the signals secreted by both organs are mixed up in the bloodstream, each organ can only gain knowledge about the average size by measuring the hormone concentration.

We consider two versions of this feedback, each with its own unique experimental signatures:

(A) Proportional feedback on absolute size, or 'FS-P model'

(B) Integral feedback on absolute size, or 'FS-I model'

2.2.4 Continuous Feedback on Growth Rate (FR)

Another possible case of continuous feedback is feedback on growth rate. This scenario implies that the coordination signal is secreted into the blood by organs in proportion to their growth rate. Again, hormone concentration in blood will carry information about the average growth rate of organs. Then each cell in each organ will have to compare its growth rate to this average growth rate to decide if it should slow down (to compensate for the other organ) or speed up (to catch up with the other organ). This case on the face of it seems more biologically probable as it is more natural for cells to know their growth rate than it is for them to know the absolute size of the entire organ and it does not require extra players such as a diluting chemical inside the organ. We also consider two versions of this scenario and will discuss their differences in the next section:

(A) Proportional feedback on growth rate, or 'FR-P model'

(B) Integral feedback on growth rate, or 'FR-I model'

2.2.5 Issues with Conversion of Hormone Concentrations

In both FS and FR models, organs need to convert the total concentration of hormone $[h]$ that they sense in the blood to a a meaningful average size (FS models) or growth rate (FR models) that they can then compare to their size or growth rate. This is not a trivial process and it is hard to imagine that organs are able to precisely interpret the correct blood volume accessible to them at all times, which is necessary to back out the information about average size or growth rate hidden in the hormone concentration. Thus, it is fair to assume that organs are likely to misinterpret the hormone concentration to some extend (but see [103] for a case where misinterpretation is not an issue). The question then is whether these feedback models are sensitive to signal misinterpretation and if so, how sensitive they are. We will see that only one mechanism (FR-P) is completely robust against errors in conversion, while others are sensitive to errors to varying degrees.

In Section 2.3, we work out the mathematical form of each model, which allows us to explore the biological implications of and issues with each scenario.

Scenario	Abrv.	Coefficient sign	Corrects δA_∞?	Sensitive to c_i?	Sensitive to $A_i(0)$?
No coordination	NC	N/A	No	N/A	No
Timing-only	T	N/A	No	N/A	No
Proportional feedback on absolute size	FS-P	Positive	Partially	Yes	No
Integral feedback on absolute size	FS-I	Positive	Yes	Yes	No
Proportional feedback on growth rate	FR-P	Negative	No	No	No
Integral feedback on growth rate	FR-I	Positive	Yes	Yes	Yes

Table 2.1: Overview of coordination scenarios. The following explain what each column mean. 2$^{\text{nd}}$ column: the abbreviation of each scenario that we will use throughout the chapter. 3$^{\text{rd}}$ column: what the effects of increasing the signal concentration are, e.g. a positive coefficient means increasing signal concentrations promotes growth. 4$^{\text{th}}$ column: whether the model is able to correct errors in target size, δA_∞. 5$^{\text{th}}$ column: whether the model is robust against misinterpretation of hormone concentration by organs ('Yes' means the model is not robust). 6$^{\text{th}}$ column: whether the model is robust against variabilities in initial sizes ('Yes' means the model is not robust).

2.3 Scenarios of Growth and Coordination: Models

Here, we go through the cases presented in the previous section one by one, first building the model mathematically based on our biological assumptions, then discussing experimental signatures and implications using fixed point analysis of the steady state organ sizes, and finally exploring the sensitivity of each model towards errors in parameters.

2.3.1 NC Model

This model assumes no coordination between organs in normal conditions. We model growth of two organs with sizes A_i $(i = 1, 2)$ assuming that each one knows its target size $A_\infty^{(i)}$ [assumption **(I)** in Section 2.2] and that there is no communication between them (the dynamics are decoupled). To do so, we assume that growth is exponential initially and slows down as the organ approaches its target size. Additionally, we assume that as the organ approaches its target size, the difference $A_\infty^{(i)} - A_i$ decays exponentially.

The simplest mathematical model with a built-in target size that captures these asymptotic behaviors is the logistic growth. In logistic growth the growth rate decreases linearly with size, making it a natural first choice for our model. The logistic differential equation is

$$\frac{\mathrm{d}A_i}{\mathrm{d}t} = \dot{A}_i = kA_i(A_\infty^{(i)} - A_i). \tag{2.1}$$

From Eq. 2.1 it is clear that if there is no coordination between organs, organs need to have the same target size A_∞ to high precision or each organ would approach a different final size leading to unwanted residual asymmetry (Fig. 2.1A). This is in fact a necessary but not sufficient condition because organs also need to have enough time before growth arrest to reach their asymptotic target size [based on assumption **(II)** in Section 2.2].

To understand why that is the case, we need to remember that growth is a noisy process. To discuss the consequences of noise, it is constructive to briefly look at noisy growth of organs (discussed in more details in Appendix A). Taking growth to be approximately a Poisson process and assuming that there is no cell death, noise can be shown to have a strength proportional to growth rate, and for each organ we will have:

$$\mathrm{d}A_i = kA_i(A_\infty - A_i)\ \mathrm{d}t + \epsilon\sqrt{kA_\infty\ A_i(A_\infty - A_i)}\ \mathrm{d}W_i, \tag{2.2}$$

where ϵ is a dimensionless noise strength parameter, $\mathrm{d}W_i$ is the Wiener process [104] and we have assumed that both organs have the same target size A_∞. We can see that noise goes down as A_i approaches A_∞. Importantly, this feature is due to the assumption that there is

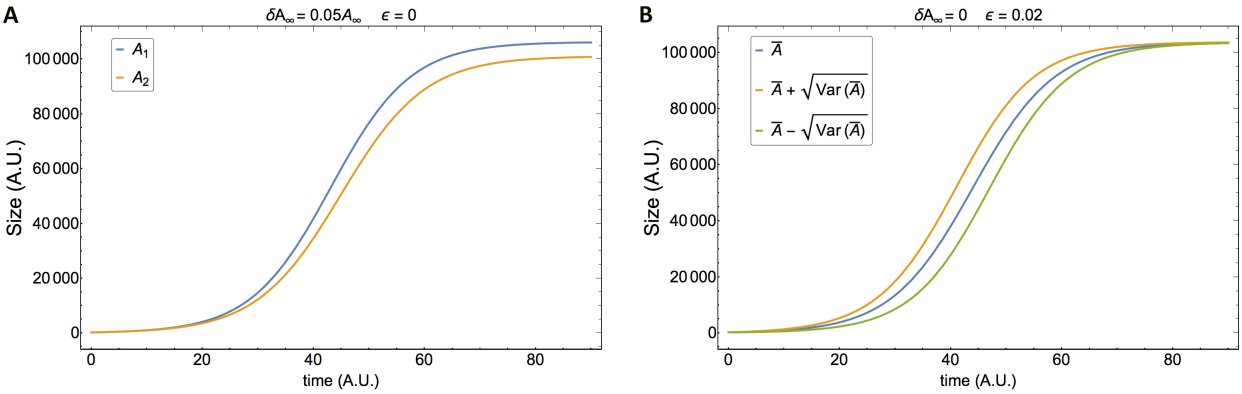

Figure 2.1: NC model requires the organs to have the same target size and are allowed enough time to grow. (A) Organs with different target sizes will have a high FA (5% in this case). Here it is assumed that there is no stochasticity due to growth fluctuations. (B) Even if organs have the same target sizes, noise can lead to variability. The average area $\langle \bar{A} \rangle \pm \sqrt{\mathrm{Var}(\bar{A})}$ is plotted against time. We can see that variance goes down as organs approach A_∞, so premature growth arrest will lead to high FA.

no cell death. If cell death is significant during growth, noise level never approaches zero.

According to 2.2, in order to reach the same size, organs need enough time to grow close enough to A_∞ so that the noise level is below a certain threshold. This threshold depends not only on ϵ, but also on the distance from A_∞. Therefore, even though on average organs may be following the same growth dynamics, the width of the size distribution will be nonzero unless organs are close enough to their target size (Appendix A) (Fig. 2.1B). In Fig. 2.1B, we plot $\langle \bar{A} \rangle \pm \sqrt{\mathrm{Var}(\bar{A})}$ with $\langle \bar{A} \rangle = (\langle A_1 \rangle + \langle A_2 \rangle)/2$, where $\langle \dots \rangle$ is the ensemble average over the noise and the overhead bar represent the mean.

Experimental Signatures

Assume that a hormone is identified or is suspected to be involved in organ coordination in response to large perturbation. Even though in normal physiological conditions the hormone does not play any role in coordination, if the hormone is involved in organ autonomous error corrections and ensuring homeostasis, knocking it out can still lead to higher FA by either increasing ϵ in Eq. 2.2 or leading to different targets sizes (Appendix A).

If the hormone is only permissive in normal conditions and has an indirect role in autonomous organ growth, its precise concentration may not matter, so for example, knocking it out and feeding the animal a downstream hormone required for proper tissue growth and homeostasis should rescue the wild type phenotype. Similarly, heterozygote mutants may not display an FA phenotype.

It is also possible that the mechanisms responsible for autonomous error corrections are

separate than the mechanism of coordination in response to severe perturbations. In that case, knocking down the coordination signal in normal conditions should not have any effect on final FA.

Error Sensitivity and Robustness

Perhaps not so much an issue, but a feature of the model is that it assumes that organs set their target sizes correctly with high precision. This implies organ autonomous error correction mechanisms.

2.3.2 T Model

This model assumes that in normal conditions, the coordination signal is necessary for achieving low FA by delaying maturation long enough so that the organs are close to their target sizes and noise level is low, but importantly, the signal is not involved in size coordination. So, while the model is mathematically represented by the same equation as NC model, (i.e. organs still follow Eq. 2.1 as they grow, and they still need to autonomously reach the same A_∞), T model differs from all other scenarios in that the maturation time, which we call t_f, is not assumed to be fixed in this model. In other words, the other models assume t_f is fixed and independent of growth history, whereas T model instead assumes that the signal affects t_f based on the growth history of organs such that they have enough time to grow.

Experimental Signatures

Where this model differs from NC model is in genotypes where the signal is knocked out. For these mutants, T model asserts that maturation will be accelerated since there is no signal to delay it and this acceleration causes organs to stop growing farther away from their target size, thus increasing final FA (Eq. 2.2), whereas NC model states that noise strength of individual organs may increase in mutants but developmental timing is untouched. This is an important distinguishing feature that can be tested in experiments.

Error Sensitivity and Robustness

The issue with this model is again the fact that the model necessitates having the same target size, so T model still requires autonomous error correction mechanisms.

2.3.3 FS-P model

As the first continuous feedback mechanism, let us assume that each cell in the organs secretes into the bloodstream an amount of a hormone proportional to its size. Then the total amount of hormone N_h in the bloodstream follows the rate:

$$\frac{\mathrm{d}N_h}{\mathrm{d}t} = r(A_1 + A_2) - \mu N_h, \tag{2.3}$$

where r is a proportionality constant and μ is the degradation rate. Assuming fast degradation so that the hormone is in a quasi steady state, $N_h = (2r/\mu)\bar{A}$, where $\bar{A} = (A_1 + A_2)/2$. Cells then can read off the total hormone concentration in the blood,

$$[h] = N_h/V \propto \bar{A}/V. \tag{2.4}$$

Here V is the volume of the blood available to the organs, which we take to be a constant. Even though as the animal grows, perhaps V also increases, because our interest is in the final size of the organs, taking V to be a constant does not affect the fixed point analysis and it is the most natural choice (assuming that V is not strongly correlated with organ sizes).

Eq. 2.4 shows that the coordination signal is proportional to the average size of the organs. In other words, an average size is all the information the coordination signal can carry. This is because the signal secreted by each organ gets mixed in the same pool and information about individual organ sizes is lost.

Each cell then reads out $[h]$ and constructs an error signal that will be fed back to its growth rate. As we discussed in Section 2.2, each cell in organ i has to know the absolute size A_i through some other mechanism. The FS-P model is

$$\frac{\dot{A}_i}{A_i} = k(A_\infty^{(i)} - A_i) + \eta(c_i\bar{A} - A_i), \tag{2.5}$$

where $\dot{A}_i/A_i$ is the cell growth rate, and η is the strength of feedback, followed by the error signal that is fed back to the growth rate proportionally. c_i is organ i's interpretation of the concentration $[h]$ (Section 2.2.5). In other words, c_i represents what organ i thinks the blood volume is. Ideally, we want $c_i = 1$ as it will mean that the error signal will try to get organs close to the average size. However, it is almost impossible for organs to be able to correctly interpret the signal concentration and exactly back out $\bar{A}$ at all times.

For simplicity, we assume that c_i are independent of time. We will study the consequences of errors in c_i for the final organ sizes in Section 2.3.3. To find the steady state behavior of

FS-P model, we find the fixed point of Eq. 2.5 ($\dot{A}_i = 0$ at $t \to \infty$):

$$\begin{aligned} \bar{A}(t \to \infty) &= \frac{k}{k + (1-\bar{c})\eta} \bar{A}_\infty \\ \delta A(t \to \infty) &= \frac{k}{k+\eta} \delta A_\infty + \frac{\eta\, k\, \delta c}{k + (1-\bar{c})\eta} \bar{A}_\infty, \end{aligned} \tag{2.6}$$

with $\delta A = A_1 - A_2$, and other quantities similarly defined.

Experimental Signatures

Here, we summarize the main implications of FS-P model.

Feedback coefficient η is positive: The feedback coefficient in FS-P model has to be positive ($\eta > 0$) in order for coordination to reduce errors. This can be seen from Eq. 2.5: Say initially $A_1(0) < A_2(0)$. Then in the ideal case $c_1 = c_2 = 1$ the error signal $\bar{A} - A_1 > 0$, therefore, $\eta > 0$ is required $\dot{A}_1$ to increase so A_1 can catch up to A_2. Experimentally, this means that if the concentration of signal is increased (via overexpression of hormone), the feedback is expected to increase the growth rate (Appendix A).

FS-P model partially corrects errors in target size if $\delta c = 0$: From Eq. 2.6, $\delta A(t \to \infty) = k\, \delta A_\infty / (k+\eta) < \delta A_\infty$ if $\delta c = 0$. Intuitively, stronger feedback (larger η) improves the error correction mechanism. However, FS-P model does not guarantee perfect error correction. Importantly, note that $\eta \to \infty$ is pathological because it will drive the organ sizes to zero, $\bar{A}(t \to \infty) \to 0$, unless $\bar{c} = 1$ (in this case, since we are additionally assuming $\delta c = 0$, this condition implies that organs need to interpret the signal perfectly). Regardless, as long as the error in target size δA_∞ is not too large, FS-P model can lower it below an acceptable value (Fig. 2.2A). The FA normalized by the average area at steady state is $\delta A(t \to \infty)/\bar{A}(t \to \infty) = [(k + (1-\bar{c})\eta)/(k+\eta)]\delta A_\infty / \bar{A}_\infty$, which linearly depends on $1 - \bar{c}$. Interestingly, this means that if organs overestimate the signal concentration $\bar{c} > 1$, the steady state FA will be lower.

Notably, it is reasonable to believe that in most cases, the condition $\delta c = 0$ can be met as it simply means that both organs have the same interpretation of the signal concentration, which can be expected to be true when both are subject to the same environment. If however, the ability of one of the organs to interpret the signal is disturbed, we expect FA to increase even if the organs accurately estimate their target sizes (Eq. 2.6).

Mutants will have smaller organs and higher FA: knocking out the gene responsible for the coordination signal or knocking down the signal effectively amounts to setting $c_1 = c_2 = 0$ because this means that organs will not receive any hormone concentration. From Eq. 2.5 we find $A_i(t \to \infty) = k\, A_\infty^{(i)}/(k+\eta)$, which is smaller than final wild type organ sizes. Assuming

$c_1 = c_2$ for wild type, it can be easily seen from Eq. 2.6, $\bar{A}(t \to \infty)$ in wild type is larger than in mutant. Moreover, even though $\delta A(t \to \infty)$ is the same in both wild type and mutant ($c_1 = c_2$ in wild type), error relative to $\bar{A}(t \to \infty)$ is larger in mutant. Thus, mutants have a higher FA than wild type (Fig. 2.2B).

Organs in heterozygous mutants are expected to secrete about half the hormone as the the wild type animals ($c_i \sim 1/2$). Hence, final average organ size is expected to be smaller than wild type but larger than knockout mutants, and FA to be higher than wild type but lower than knockout.

Feedback reduces noise during growth: Here, we assume both organs have the same target size and $c_1 = c_2 = 1$ in wild type, and focus on noisy dynamics of the FS-P model to see if the noise during the growth is lowered by feedback. $c_i \neq 1$ qualitatively behaves the same. We add noise with strength proportional to the square root of growth rate and use small noise approximation outlined in Appendix A to find $\mathrm{Var}(A_1 - A_2)$ for three cases: $\eta = 0$ (NC model), $\{\eta \neq 0, c_1 = 1\}$ (FS-P model, wild type), and $\{\eta \neq 0, c_1 = 0\}$ (FS-P model, knockout). We find that $\mathrm{Var}(A_1 - A_2)$ is smaller for FS-P model throughout the growth. Interestingly, the knockout shows lower variability compared to wild type initially due to smaller organ sizes, but later it becomes noisier than wild type (Fig. 2.2C). To find FA, we normalize $\sqrt{\mathrm{Var}(A_1 - A_2)}$ by the average area $\langle \bar{A} \rangle = (\langle A_1 \rangle + \langle A_2 \rangle)/2$, which reveals that knockout mutants have a higher FA throughout growth (Fig. 2.2D).

Error Sensitivity and Robustness

The main issue with FS-P model stems from the dependence of the steady state on how signal is interpreted by the organs. In particular, if $\delta c \neq 0$, from Eq. 2.6 we can see that even if organs have determined their target sizes correctly ($\delta A_\infty = 0$), the final sizes will be different and the steady state FA depends linearly on δc. However, we note that it is not very likely for organs to misinterpret the signal in different ways as long as no significant perturbation is applied to one organ and not the other.

2.3.4 FS-I Model

We saw that even though FS-P model improves errors in target size, it still is not able to fully correct them. It is well known in control theory that in order to ensure that a system reaches a specific final state, integral feedback needs to be employed [105]. Therefore, here, we assume that the error signal is integrated before being fed back to organ growth rates.

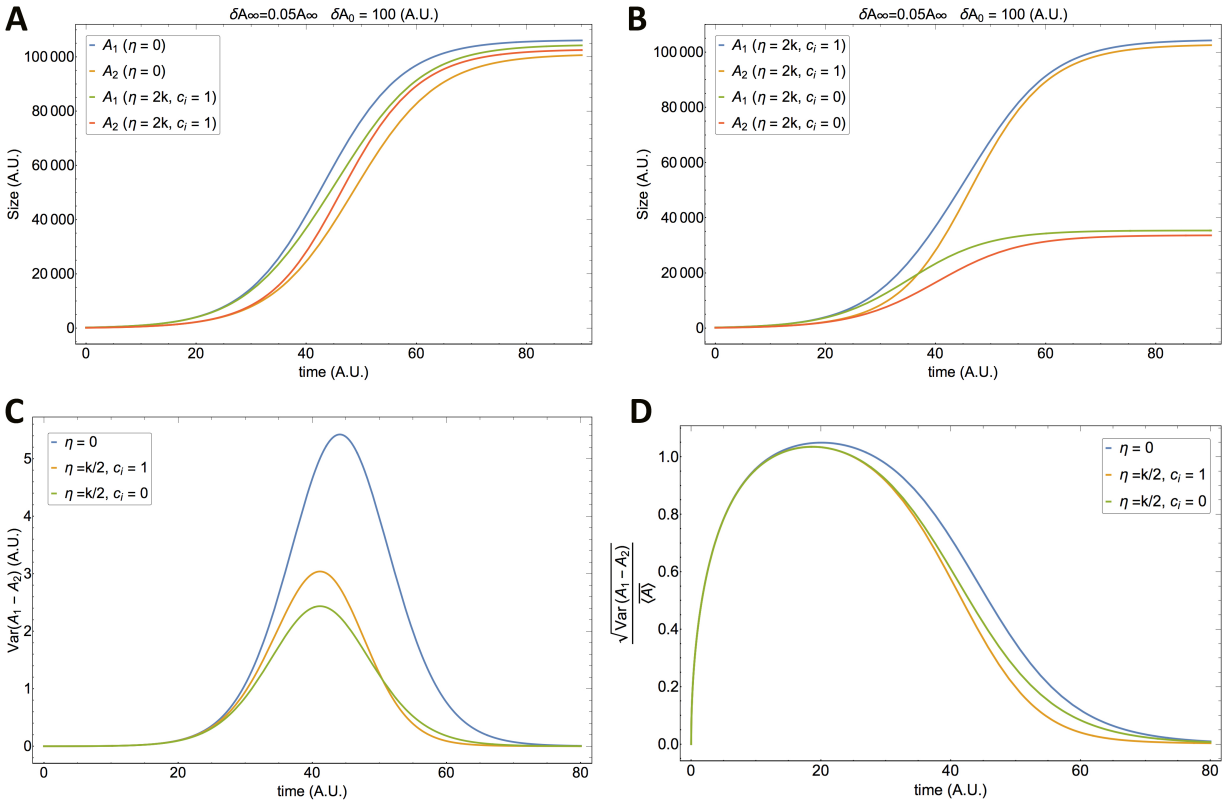

Figure 2.2: FS-P model. (A-B) Some asymmetry in initial sizes was introduced to better distinguish organs during growth. $(A_1(0) = 264, A_2(0) = 164)$. (A) Left and right organs growing without feedback (NC model) and with feedback (FS-P model). Feedback can partially correct errors in target size. (B) Knocking out the signal $c_i = 0$ leads to increased FA and significant size reduction. Even though $\delta A(t \to \infty)$ is not changed in mutants, the lower average size leads to higher FA. (C-D) Noisy dynamics shows that $\mathrm{Var}(A_1 - A_2)$ is lowered in FS-P model compared to NC model $\eta = 0$. In knockout mutants, $\mathrm{Var}(A_1 - A_2)$ is initially lower due to smaller organ sizes. $\mathrm{Var}(A_1 - A_2)$ normalized by the average size $\langle \bar{A} \rangle$ shows that FA is higher in mutants throughout the growth, but interestingly, still lower than NC model.

The differential equations are thus

$$\begin{aligned} \frac{\dot{A}_i}{A_i} &= k(A_\infty^{(i)} - A_i) + \eta\, g_i(t) \\ \dot{g}_i(t) &= c_i \bar{A} - A_i, \end{aligned} \tag{2.7}$$

where g_i is the integral of error signal and other parameters defined similarly to FS-P model.

It is instructive to also look at the dynamics of $\bar{g}$ from Eq. 2.7:

$$\dot{\bar{g}}(t) = (\bar{c} - 1)\bar{A}. \tag{2.8}$$

Eq. 2.8 shows that the dynamics only results in finite steady state sizes if $\bar{c} = 1$, in which case, taking $g_i(0) = 0$, $\bar{g}(t) = 0$. This implies $A_i(t \to \infty) = c_i \bar{A}_\infty$. If additionally, $c_i = 1$ for each i, organs are guaranteed to be the same size as the average size at fixed point, $A_1(t \to \infty) = A_2(t \to \infty)$, as expected from integral feedback.

However, if $\bar{c} \neq 1$, the error signal keeps feeding back on organs until their sizes shrink to zero or gets pathologically large. For instance, if $c_1 = c_2 = 1/2$, initially, sizes will grow because the dynamics is dominated by the logistic growth, however, since A_1 or A_2 can never simultaneously be half the average size $\bar{A}$ (unless they are both identically zero), the magnitude of the integrated error signal gets large enough and will drive the dynamics to the zero steady state (Fig. 2.3C).

Experimental Signatures

It is already clear that this model is not robust against errors in c_i, but before discussing it in the next subsection, we provide some experimental signatures assuming $\bar{c} = 1$ in wild type so that the dynamics is well-behaved.

η is positive: Similar to FS-P model, this model requires $\eta > 0$. Notably, for $\eta < 0$ the fixed point becomes unstable as can be seen from stability analysis below.

Feedback can correct errors in target size if $c_i = 1$: as we showed above, the integral feedback guarantees that the organs will reach the same size at steady state if organs perfectly interpret the signal concentration.

FS-I model is oscillatory: It is common for integral feedback to show oscillations. In particular, in integral control, the output may be allowed to overshoot until it settles to the steady state as a damped oscillator. Accordingly, FS-I model also shows oscillations with a period that depends on the strength of feedback: The larger η is, the faster oscillations will be (Fig. 2.3A-B). A simple stability analysis around the fixed point shows a damped oscillation, as outlined below.

For simplicity, we assume organs have the same target size. Expanding $A_i = A_\infty + x_i$, where $x_i \ll A_\infty$, we can expand Eq. 2.7 to lowest order in x_i. After taking a second derivative, the dynamics of x_i is given by

$$\ddot{x}_i = -[kA_\infty - \eta g(t \to \infty)]\dot{x}_i + \eta A_\infty(\bar{x} - x_i). \tag{2.9}$$

From Eq. 2.7 with $A_\infty^{(i)} = A_\infty$, we can find $g(t \to \infty) = 0$. This is the equation for a coupled damped oscillator. The dynamics of $\delta x = x_1 - x_2$ makes this very clear:

$$\delta\ddot{x} + kA_\infty\delta\dot{x} + \eta A_\infty\delta x = 0. \tag{2.10}$$

The frequency of undamped oscillations is $\omega_0 = \sqrt{\eta A_\infty}$ and the damping ratio is $\zeta = k\sqrt{A_\infty}/2\sqrt{\eta}$. This oscillation can be observed experimentally if *in vivo* images of organs during growth is obtained. We expect organ sizes to oscillate if FS-I model is at play. Finally, this analysis also shows that $\eta > 0$ is required for stability of fixed point.

Mutants lose their organs: Any mutation that causes $c_i < 1$ will drive $A_i \to 0$ at steady state. If however, maturation happens before the organs reach zero size, mutants will not lose their organs, albeit the organs will be significantly smaller than wild type. If somehow maturation is delayed (for instance by inhibiting the maturation signals), it is expected that organs would eventually destroy themselves by cell death. Note that even though in FS-P model, mutants has smaller organs, the dynamics reaches a nonzero steady state, whereas in FS-I model, the steady state is identically zero.

Error Sensitivity and Robustness

FS-I model has a serious problem, which is its sensitivity to c_i. There are two issues that arise from this sensitivity:

1) As we showed, unless $\bar{c} = 1$, the dynamics does not have a finite-sized fixed point. However, this condition is difficult to achieve and maintain throughout the growth because as the animal grows, organs need to always know precisely what the blood volume available to them is, which is unrealistic given the noisy nature of biology.

2) If the condition $\bar{c} = 1$ is met but $\delta c \neq 0$, organs will not reach the same size: $A_i(t \to \infty) = c_i\bar{A}_\infty$, thus the FA normalized by the average size will be δc at fixed point regardless of errors in target size. In other words, the model corrects errors in target size but introduces errors of its own (Fig. 2.3D).

Therefore, unless $c_1 = c_2 = 1$, either the dynamics will be pathological or errors in integration will carry over and perfect size coordination cannot be achieved, which is what

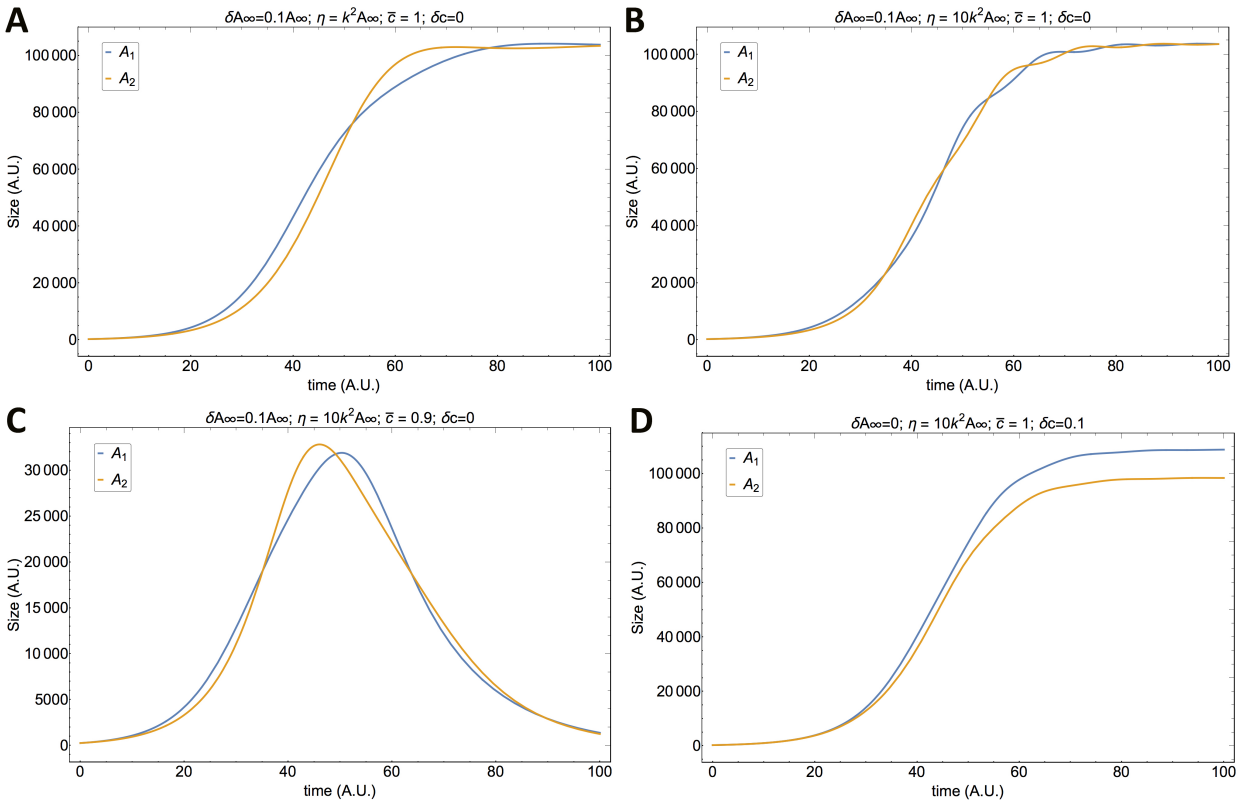

Figure 2.3: FS-I model. (A-B) FS-I model can correct errors in target size, however, it is oscillatory. Increasing η increases the frequency of oscillations. (C) FS-I model is sensitive to $\bar{c}$. If $\bar{c} \neq 1$, the dynamics is pathological. For example, underestimating the signal concentration will cause organs to shrink to zero. Similarly, in mutants, same behavior is observed. (D) FS-I model is sensitive to δc. A small change in δc will lead to different final sizes even if $\delta A_\infty = 0$.

an integral feedback model is intended to do. Therefore, it seems inevitable to conclude that FS-I is not a robust mechanism of size coordination due to its sensitivity to misinterpretation of signal.

2.3.5 FR-P Model

Along the same line as Section 2.3.3, we will build another continuous model, this time with a coordination signal that is a readout of growth rate instead of absolute size. Assume that each cell secretes an amount of hormone proportional to its growth rate. On average, growth rate of a cell belonging to organ i is $\dot{A}_i/A_i$, therefore, hormone production rate over the entire area of organ i is proportional to $A_i(\dot{A}_i/A_i) = \dot{A}_i$. The hormone is released into the circulatory system, hence hormone produced by each organ is mixed with that produced by the other organ. We again assume that the hormone is degraded with constant μ and

produced with rate r, and that the hormone degrades fast and is in quasi steady state. Then for the total number of hormone molecules produced we have $N_h = (2r/\mu)\dot{\bar{A}}$ and the hormone concentration $[h] = N_h/V \propto \dot{\bar{A}}/V$ where V is again the volume of the blood available to the organs. We can take V to be a constant like in Section 2.3.3, but perhaps a more accurate guess would be $V \propto (A_1 + A_2)$ leading to

$$[h] \propto \frac{\dot{\bar{A}}}{\bar{A}}. \tag{2.11}$$

Note that in Section 2.3.3, we could not use the same approximation for V as N_h was also proportional to the average size, which would have led to a constant hormone concentration defeating the purpose of coordination. In Appendix A we show that for FR-P model, a constant V qualitatively does not differ from our choice.

Eq. 2.11 shows that the concentration of hormone is a readout of the average growth rate per average area, or roughly, the average "distance" from the target size ($\dot{A}/A \propto A_\infty - A$). In fact, another way that we can get a hormone concentration that effectively looks like Eq. 2.11 is if the organ produces a fixed amount of the hormone, part of which will be used in the organ and the rest leaks out. Then as the organ grows, less of the hormone can leak out, until the organ reaches its target size at which point all of the hormone is used up in the organ. Thus the total amount of hormone will be proportional to the target size, and at each instant, an amount proportional to $A_\infty - A$ leaks out.

Unlike FS models, we do not require extra chemicals for the model to work. Cells can simply compare their own growth rate $\dot{A}_i/A_i$ to $[h]$ and autonomously regulate their growth rate so that both organs sync up their growth. Thus, we formulate a feedback mechanism by considering the error signal $\dot{\bar{A}}/\bar{A} - \dot{A}_i/A_i$, which is fed back to the growth rate of each cell:

$$\frac{\dot{A}_i}{A_i} = k(A_\infty^{(i)} - A_i) + \lambda\left(c_i\frac{\dot{\bar{A}}}{\bar{A}} - \frac{\dot{A}_i}{A_i}\right). \tag{2.12}$$

Here λ represents the strength of the feedback signal that the organs feel, and c_i is defined similarly as before. Notably, if $c_i = 1$, $\bar{A}$ does not see any feedback (i.e. it is independent of λ). This means that feedback is symmetric with respect to the average size.

We can rewrite this equation to get another useful form of this model:

$$\frac{\dot{A}_i}{A_i} = \frac{k}{1+\lambda}(A_\infty^{(i)} - A_i) + c_i\,\frac{\lambda}{1+\lambda}\frac{\dot{\bar{A}}}{\bar{A}}. \tag{2.13}$$

This alternative form will be useful later when we discuss Experimental signatures of this model.

Fixed point analysis of Eq. 2.12 reveals that at steady state

$$A_i(t \to \infty) = A_\infty^{(i)}, \tag{2.14}$$

which immediately appears to disqualify FR-P model as it is not capable of correcting errors in target size (Fig. 2.4B). However, this model has benefits that actually make this the most plausible scenario of coordination that we will discuss. In FR-I model section we explore whether integral feedback on growth rate does better in terms of correcting errors in target size.

Experimental Signatures

Even though FR-P model fails at correcting possible errors in target size, it still has benefits for development that are worth discussing; therefore, in this section we assume that by some other (perhaps organ autonomous) mechanism, target sizes are correctly set by the organs, $A_\infty^{(i)} = A_\infty$, and study FR-P model's experimental signatures.

Feedback coefficient λ is negative: Unlike FS models, this model require feedback coefficient to be negative ($\lambda < 0$). To understand the sign of λ assume that $A_1 > A_2$ just before the feedback is turned on. If organs are past the initial exponential phase of growth, because $A_1 > A_2$, A_1 is closer to the target size and therefore has a smaller growth rate. If we turn on feedback, we expect it to slow down A_1 even more while accelerating A_2 growth so it can catch up sooner (Fig. 2.4A). In other words, the error signal $\dot{\bar{A}}/\bar{A} - \dot{A}_i/A_i$ is negative for the smaller organ and we need a negative λ to accelerate $\dot{A}_2$. As a matter of fact, $-1 < \lambda < 0$ because $\lambda = -1$ is a singular point, which could be seen from Eq. 2.13.

Experimentally, $\lambda < 0$ suggests that if the hormone concentration is elevated, growth rate of the organ would decrease (Appendix A).

Model is robust against misinterpretation of signal by organs: FR-P model is more well-behaved and robust against noise than FS models since the steady state is independent of c_i, or how accurately the organs interpret the signal (Eq. 2.14). Because of this robustness, for the rest of this section, we assume $c_i = 1$ for wild type as it makes our calculations more straightforward.

Feedback reduces noise during growth: Since we have assumed that the organs have the same target size, we need some other source of variation to study how FR-P model does. Firstly, if the organs have different initial sizes right before the feedback kicks in, we can see in (Fig. 2.4A) that feedback reduces the size difference faster than having no feedback (NC model). More concretely, we study the stochastic version Eq. 2.12 to explore the effects of feedback on noise and in particular, $\mathrm{Var}(A_1 - A_2)$. We find that similar to FS-P model,

feedback on growth rate reduces noise throughout growth, which also means that the animal can reach maturation sooner than NC model while having the same FA (Fig. 2.4C).

Mutants have a higher FA than wild type: Similar to before, a knockout mutant corresponds to $c_i = 0$ in our model. From Eq. 2.13 we can see that organs in knockouts show logistic growth with a modified growth rate $k' = k/(1 + \lambda) > k$. In (Fig. 2.4D) we can see growth can accelerate significantly in mutants according to FR-P model and according to Eq. 2.2, since organs will reach their target size much faster, noise in mutants will be lower. However, we believe that this significant increase in growth rate is implausible biologically as there are fundamental limits to how fast cell cycles can become, and thus a more likely scenario is that organs in the absence of the coordination signal get desensitized against higher levels of growth promoting factors. This means that in mutants $k' \to k$, which means that effectively, mutants in this model are equivalent to setting $\lambda = 0$, or in other words NC model. Looking at (Fig. 2.4C) again shows that mutants have a higher FA than wild types in FR-P model.

Equivalently, we can think of this rescaling of k as asking organs to stop growing at the same average size as wild type (since as we mentioned, the average size is independent of λ at least when $c_i = 1$). This allows us to explore other mutations such as heterozygous mutations where we expect organs to produce half of the signal $c_i \sim 1/2$. In this case, asking for maturation at the same average size as wild type results in a higher FA than wild type but lower FA than knockout mutation similar to FS-P. The difference between FS-P and FR-P here is that in FS-P a significant decrease in organ size is expected for mutants where as in FR-P model that is not the case.

Error Sensitivity and Robustness

The main issue with this model is that it cannot correct errors in target size. Biologically, this is because when each organ reaches its target size, it will stop secreting the coordination signal. Moreover, FR-P model ensures that the growth rates are synced throughout the growth, therefore both organs will reach their respective target sizes at roughly the same time, meaning that at that point there will be no signal to correct any error in target size.

2.3.6 FR-I Model

As we saw, even though FR-P model is promising in terms of syncing up the organ growth rates thus reducing noise, and also being robust against errors in c_i, it fails at fixing errors in target size. Here, we study the integral feedback on growth rate in hopes to fix that issue.

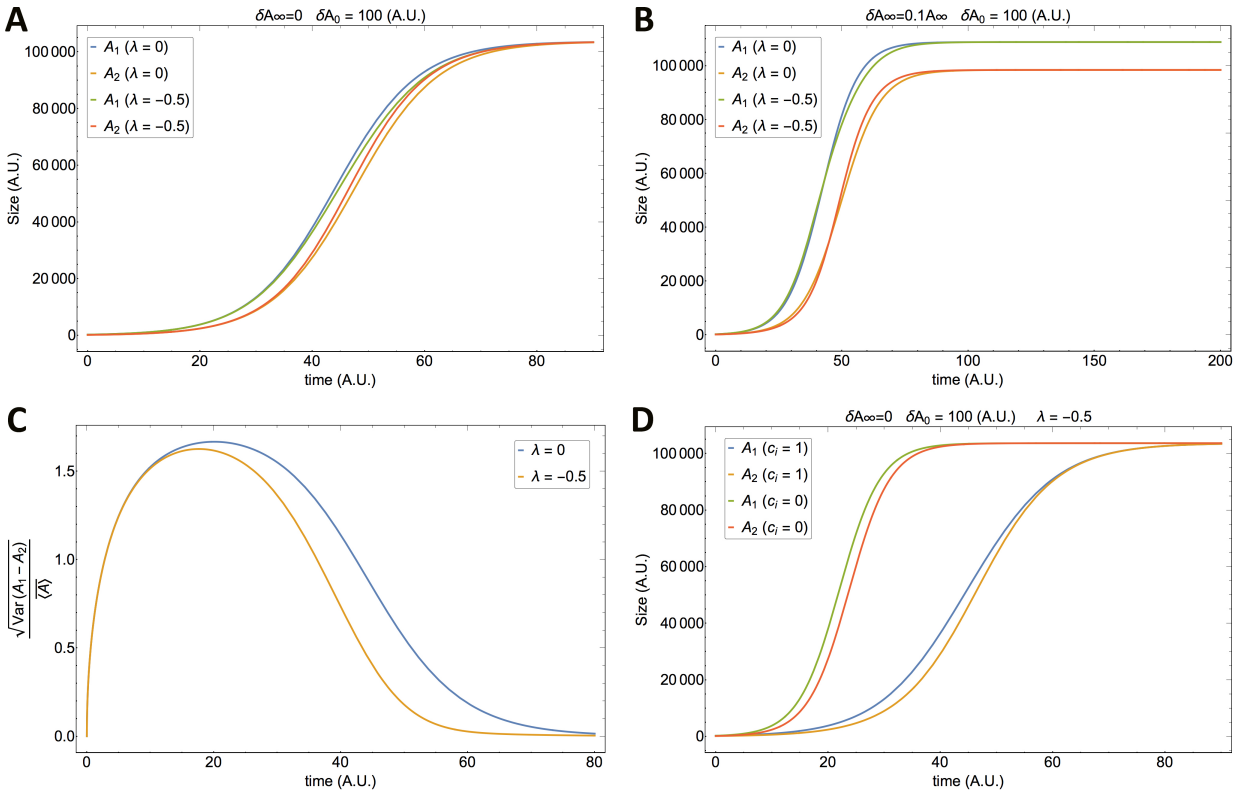

Figure 2.4: FR-P model. (A-B) In the absence of error in target size, FR-P model can sync up the growth rate during the growth. Different initial conditions were chosen to demonstrate the error correction mechanism; however, FR-P model cannot correct errors in target size ($A_1(0) = 264, A_2(0) = 164$). (C) Noisy dynamics shows that FR-P model can lower noise during growth compared to the NC model $\lambda = 0$. We also believe that knockout mutants also correspond to $\lambda = 0$ due to desensitization of organs to higher growth promoting factors in the absence of the coordination signal. Here we assume $\delta A_\infty = 0$. (D) If organs do not desensitize against higher levels of growth promoting factors in knockout mutants, growth rate will increase significantly, thus organs would reach their target size much faster and noise in mutants would be significantly lower because noise goes to zero as organs reach their target size (Eq. 2.2)

The differential equations of FR-I model are

$$\begin{aligned} \frac{\dot{A}_i}{A_i} &= k(A_\infty^{(i)} - A_i) + \lambda\, f_i(t) \\ \dot{f}_i(t) &= c_i \frac{\dot{\bar{A}}}{\bar{A}} - \frac{\dot{A}_i}{A_i}. \end{aligned} \tag{2.15}$$

The steady state of this model strongly depends on initial conditions, therefore, we will discuss the behavior of Eq. 2.15 in appropriate places in the following subsection.

Experimental Signatures

Here, we summarize different implications of FR-I model.

λ is positive: Unlike FR-P model, this model is only well-behaved when $\lambda > 0$. The reason for this difference lies in the fact that the sign of $f_i(t)$, the integral of error signal, will depend on only the initial sign of $\dot{\bar{A}}/\bar{A} - \dot{A}_i/A_i$ in most cases and thus will not change sign. For example, it can be seen that when $A_\infty^{(1)} \neq A_\infty^{(2)}$, $\dot{\bar{A}}/\bar{A} - \dot{A}_i/A_i$ will change sign somewhere mid-growth, however its integral, f_i will not. So, if initially $\dot{A}_1 > \dot{A}_2$, f_1 will always be negative, and we need $\lambda > 0$ for FR-I model to properly reduce the size difference between the organs whereas in the FR-P model that depends on the instantaneous error signal and not its integral, only $\lambda < 0$ works for proper late time behavior of the model (see Appendix A for more information).

Feedback can correct errors in target size if $\delta c = 0$ and $A_1(0) = A_2(0)$: This model turns out to be sensitive to initial conditions. First, let us assume that $c_i = 1$. In Appendix A, we show that if we want the same final sizes, f_1 and f_2 must exactly have the following relationship

$$f_2(0) - f_1(0) = \log \frac{A_1(0)}{A_2(0)} + \frac{k\,\delta A_\infty}{\lambda}. \tag{2.16}$$

The most reasonable initial conditions are $f_1(0) = f_2(0)$ or each cell's integrator has to know δA_∞ and the initial sizes. This implies that for the model to correct errors in target size with the initial condition $f_1(0) = f_2(0) = 0$, we additionally need a strong feedback $\lambda \gg 0$ and $A_1(0) = A_2(0)$. Intuitively it makes sense that a strong feedback would work because integral feedback on growth rate will ensure that the growth rates are the same asymptotically, so a strong integral feedback will sync up the growth rates from the beginning and if $A_1(0) = A_2(0)$, the organs will have the same sizes throughout growth (Fig. 2.5A).

For $c_i \neq 1$ but $\delta c = 0$, it can also be seen (Fig. 2.5A) that feedback corrects errors in target size if the same conditions hold. However, the final size and growth rate will be affected. For $\bar{c} > 1$, growth rate will be larger and organs will reach a larger size, whereas

for $\bar{c} < 1$, the opposite is true, and the stronger the feedback is, the more pronounced these effects are.

Mutants have much smaller organs: In mutants, $\bar{c} < 1$, so as we mentioned above, final size of the organs will be much smaller. For example, for knockout mutants where $c_i = 0$, organs will be orders of magnitude smaller in size compared to wild type (Fig. 2.5C). This is because $\dot{f}_i < 0$ and growth rates of both organs will consistently be negatively affected. Thus, even though unlike FS-I model that loses organs in mutants, FR-I model does not, it still will lead to pathologically small organs in mutants.

Error Sensitivity and Robustness

The biggest issue with FR-I model is the strong dependence of the final sizes on initial conditions. This is problematic because it having the exact same initial sizes seems to be improbable biologically. A small difference in initial conditions will indeed leads to large final FA even if target sizes are the same (Fig. 2.5D). Moreover, this means that this model shifts the requirement of having the same target sizes (FR-P model) to a requirement of having the same initial sizes.

Additionally, we are not gaining much by this model since it is also sensitive to errors in c_i. This is especially an issue since feedback needs to be strong to correct errors in target size, which will make the effects of signal misinterpretation more pronounced and can lead to pathologically large or small organs. Also, if $\delta c \neq 0$ (which admittedly is a less likely scenario), final FA will again be large (Fig. 2.5B). For these reason, we believe this model is not a robust mechanism of size coordination.

In this section, we discussed the main biological implications of each model and their shortcomings and issues summarized in Table 2.1. Overall, integral feedback models are not robust mechanisms of error correction in organ growth. FS-P and FR-P models seem to be the most reliable coordination mechanisms, but each had its own shortcomings as we saw. Overall, it seems unlikely that organs could coordinate final sizes with a single endocrine signal. In the next section, we discuss the example of Dilp8 in *Drosophila* and study experimental implications of the models relevant in that case. In particular, based on experimental observations, Dilp8 matches the descriptions of FR-P model the most.

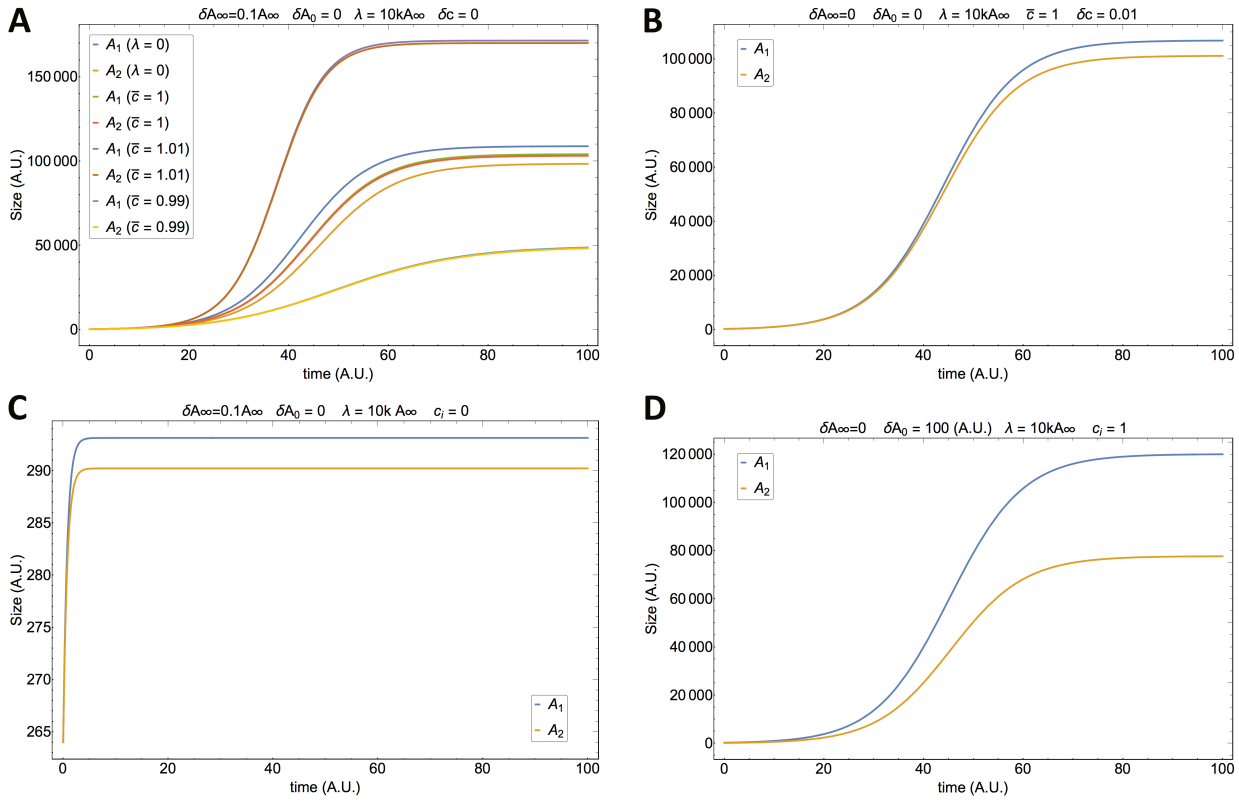

Figure 2.5: FR-I model. (A) FR-I can correct errors in target size if $A_1(0) = A_2(0)$ and $\delta c = 0$. A 1% change in $\bar{c}$ from 1 will additionally lead to a significant increase of reduction of final sizes. Note: The bright yellow curve that reaches the smallest steady state size is actually two curves almost on top of each other. (B) FR-I model is sensitive to changes in δc. Even if target sizes are the same, a 1% variation in δc leads to different final sizes. (c) Organ sizes knockout mutants reach steady state very quickly and are pathologically smaller (in this example $A_i(t \to \infty) \approx A_i(0) \approx 0.003\bar{A}_\infty$ and $A_i(0) = 264$). The reason for this pathological behavior is that in mutants, the dynamics is mainly driven by f_i due to feedback being strong which quickly reaches its steady state value. (D) FR-I model is not robust against changes in initial condition. Here $A_1(0) = 264$ and $A_2(0) = 164$.

2.4 Experimental Implications Dilp8 as a Coordination Signal in *Drosophila*

Major implications of coordination models were discussed in the previous section. Here, we focus on *Drosophila* and explore the possibility of coordination in this organism. Particularly, Dilp8 hormone is a strong candidate for a coordination signal. We know that at least in strong perturbations, Dilp8 is involved in organ coordination. The question we try to answer in this section is what the experimental implications are if Dilp8 is also involved in coordination in normal physiological conditions. We will show that based on current experimental observations of Dilp8, the most likely possibility (other than no coordination in normal growth) is FR-P model. We will then make predictions about different genetic manipulations based on this model.

Our current knowledge is that in response to growth perturbations to imaginal discs, Dilp8 is secreted by the organs and delays pupariation, which is normally initiated by a large spike in ecdysone (the molting hormone). Dilp8 is able to delay pupariation by down-regulating biosynthesis of ecdysone. Moreover, this inhibition also results in a reduction of disc growth rates since ecdysone additionally promotes disc growth [49, 106]. Furthermore, knocking out Dilp8 leads to a two- to three-fold increase in FA but not much acceleration in pupariation.

dilp8 is a target of several pathways. In response to stresses, it is known that JNK pathway activates *dilp8*. However, in normal conditions, it seems to be a target of Yorkie (Yki), a growth promoting transcription co-activator. This suggests that during normal growth, Dilp8 is a readout of growth rate. Thus, with its inhibitory effect on ecdysone, Dilp8 may be involved in a feedback loop on disc growth (Fig. 2.6A) such that overexpression of Dilp8 would lead to a decrease in disc growth rates. This suggests that if Dilp8 is involved in organ coordination in physiological conditions, the FR-P model is the best candidate for describing this mechanism. However, we also cannot fully rule out the T model, since some experiments have shown a slightly earlier pupariation in *dilp8* −/−, which is what we would expect from T model. In other words, it is possible that Dilp8 does not affect the basal level of ecdysone required for proper disc growth and only delays the large ecdysone spike to delay pupariation. We do not study the FR-I model here because of the issues we discussed about its sensitivity to initial conditions and the sign of λ being the opposite of what experiments suggest for Dilp8.

We will thus begin by testing T model based on available growth *Drosophila* data, and then move on to exploring different experimental implications of FR-P model. Since both

these models require discs to have the same target size, we assume that by some organ autonomous way, discs set their target sizes correctly. Hence, an immediate conclusion is that Dilp8 alone cannot be regulating wing final size precision as a coordination signal.

Finally, we mainly use the noisy version of the models (Appendix A) and define an FA index (FAi(t)) to study the time evolution of FA as

$$\text{FAi} = \frac{\sigma\{A_1 - A_2\}}{\langle \bar{A} \rangle} \tag{2.17}$$

where $\sigma\{\cdots\}$ denotes the standard deviation and $\langle \bar{A} \rangle = (\langle A_1 \rangle + \langle A_2 \rangle)/2$ is the average organ size. Since our models are nonlinear, we apply the small noise approximation (Appendix A) to approximate FAi. Eq.2.17 is in fact the square root of FAi6 measure defined in [107]. The reason we use the square root is that it would be easier to interpret this FAi as a relative error.

2.4.1 Application of T Model to *Drosophila* Example

Here, we assume that in the absence of large growth perturbations or damage to one of the discs, Dilp8 is only affects the timing of pupartion by delaying the large spike in ecdysone and thus follows teh T model. Before discussing the model's predictions for the role of Dilp8 in *Drosophila*, we briefly review the small noise approximation on Eq. 2.2 that we need for our analysis.

Small Noise Approximation on Logistic Growth

Because in the T model, there is no direct feedback on disc growth rates, dynamics of the discs are decoupled and each disc follows Eq. 2.2. Using the small noise approximation (Appendix A), we expand the area A_i as $A_i(t) = a_i(t) + \epsilon\ X_i(t) + \mathcal{O}(\epsilon^2)$, where $a_i(t)$ is the solution to the deterministic equation given by Eq. 2.1 (with $A_\infty^{(i)} = A_\infty$). By equating terms of the same order in ϵ, we find the following equations up to first order in ϵ

$$\begin{aligned} \frac{\mathrm{d}a_i}{\mathrm{d}t} &= k a_i (A_\infty - a_i) \\ \mathrm{d}X_i &= k X_i (A_\infty - 2a_i)\mathrm{d}t + \sqrt{k A_\infty\ a_i (A_\infty - a_i)}\ \mathrm{d}W_i. \end{aligned} \tag{2.18}$$

The time evolution of noise is captured in $\sigma\{A_i\}$, which is found to increase in value in the initial stage of the growth when growth is approximately exponential, and decrease as the organ approaches its target size and the average growth rate decreases. The initial increase in variance is expected because as the area increases exponentially any noise in divisions will

intensify over time, but as the growth rate slows down as the organ approaches its target size, strength of the noise also decays with the growth rate. The growth dynamics of a wing disc evolving according to Eq. 2.2 and with the approximation given in Eq. 2.18 is shown in (Fig. 2.6C).

Because $\sigma\{X_i\}$ is a function of $a_i(t)$, it follows from Eq. 2.17 that FAi is a function of only ϵ and $a_i(t)$. $\text{FAi}(t) = f\left[\epsilon, a_i(t)\right]$. In fact, FAi is linear in ϵ:

$$\text{FAi}(t) = \epsilon f\left[a_i(t)\right]. \tag{2.19}$$

Therefore, we can use ϵ as a control parameter to tune FAi: smaller ϵ means smaller FA. This of course makes intuitive sense, because ϵ is a measure of noise strength. The linear dependence of FAi on ϵ also means that by knowing the ratio of knockout FAi to wild type FAi, we can uniquely find the amount by which growth arrest is accelerated in mutants as we discuss next.

Acceleration of Pupariation in *dilp8* −/− Mutants

Here we provide an experimental implication of Dilp8 if it follows T model. As a demonstration, we use the data for *Drosophila* ([5] and Leopold Lab).

Based on this model, each wing grows independently according to Eq. 2.2 until growth stops at pupariation time t_f in wild type flies. If on the other hand, the discs lack the ability to secrete Dilp8 (knockout mutants), the growth stops prematurely at $t_f^* < t_f$, thus based on Eq. 2.2, since the organs are farther away from the target size, final noise and subsequently FAi (Eq. 2.17) will be higher. From the experiments, we can see how much FAi is increased and how much the timing of maturation is accelerated if any. The model gives a unique t_f^* based on the FAi increase, which we can compare to experimental results. The procedure is as follows:

1) In principle we should be able to get an average estimate for growth parameters k and A_∞ by measuring disc sizes at different times and fitting a logistic curve to the data. For instance, in (Fig. 2.6B) these parameters for *Drosophila* published in Bittig et al. are $A_\infty = 103,667\ \mu\text{m}^2$ and $kA_\infty = 0.13566\ \text{hrs}^{-1}$. This allows us to find $a_i(t)$ (Eq. 2.18). Note that growth stops before discs actually reach A_∞ as it is merely the asymptotic size. If we also obtain the average pupariation time t_f (we took it to be 72 hrs after the end of first larval instar, L1) and measure the final FAi from experiments, we can get an estimate the noise strength ϵ by solving Eq. 2.19 for ϵ at time $t = t_f$. We can then use this ϵ to get the entire width of the growth and FAi at all times. (Fig. 2.6C) shows the width for two different values of ϵ. As can be seen, a larger ϵ leads to larger width and larger asymmetry

on average throughout the growth.

2) Now, assume that we knock out *dilp8*. If T model is true, pupariation time t_f would go down and the increased FA caused by the knockout has to be due to the change in t_f only. From experiments, we can get the average mutant pupariation time t_f^* and the mutant FAi. Obtaining ϵ from wild type data has uniquely identified FAi as a function of time. Therefore, if only the pupariation time is different in mutants, we can read off the FAi at t_f^*. Fig. 2.6D shows FAi vs. maturation time for $\epsilon = 0.01$. This provides a simple test for this model. If the assumption that the signal only coordinates the timing is true, the FAi obtained from Eq. 2.19 for the experimental t_f^* should match the experimental mutant FAi, or equivalently, t_f^* obtained from Eq. 2.19 for the experimental mutant FAi should match the experimental t_f^*.

In *Drosophila*, it has been reported by some studies that pupariation is accelerated by only 4 hours or less while in other studies, no significant acceleration has been seen [1, 47]. Using the published data from [5] for average growth parameters and FAi measured for wild type and *dilp8* –/– flies from the Leopold Lab we found that an accelerated maturation time of 8 hours is needed if the hypothesis is true (p-value of 0.03). Even though not very conclusive, it seems that the model requires flies to pupariate more prematurely than what has been observed experimentally, and therefore, Dilp8 does appears to be more likely involved in a feedback mechanism in normal conditions if it plays any coordinating role at all.

2.4.2 Application of FR-P Model to *Drosophila* Example

Since knocking out *dilp8* does not cause significant acceleration in the timing of pupariation, it is reasonable to believe that at least in normal conditions, Dilp8 does not delay pupariation and thus may only be involved in a feedback mechanism. Furthermore, based on biological data, it seems that if Dilp8 is indeed feeding back on organ growth, it must be a negative feedback on growth rate, meaning that FR-P model is the most likely candidate for describing the coordination between left and right wings. Here, we discuss the experimental implications of this model for specific *Drosophila* experiments. We assume that feedback starts from the beginning of the larval growth, however, our results can be modified if feedback starts later. We do not expect significant dependence on when feedback starts during development as long as it does not start too close to pupariation. This can be verified later in Fig. 2.7D where we start the feedback at a time after the beginning of growth.

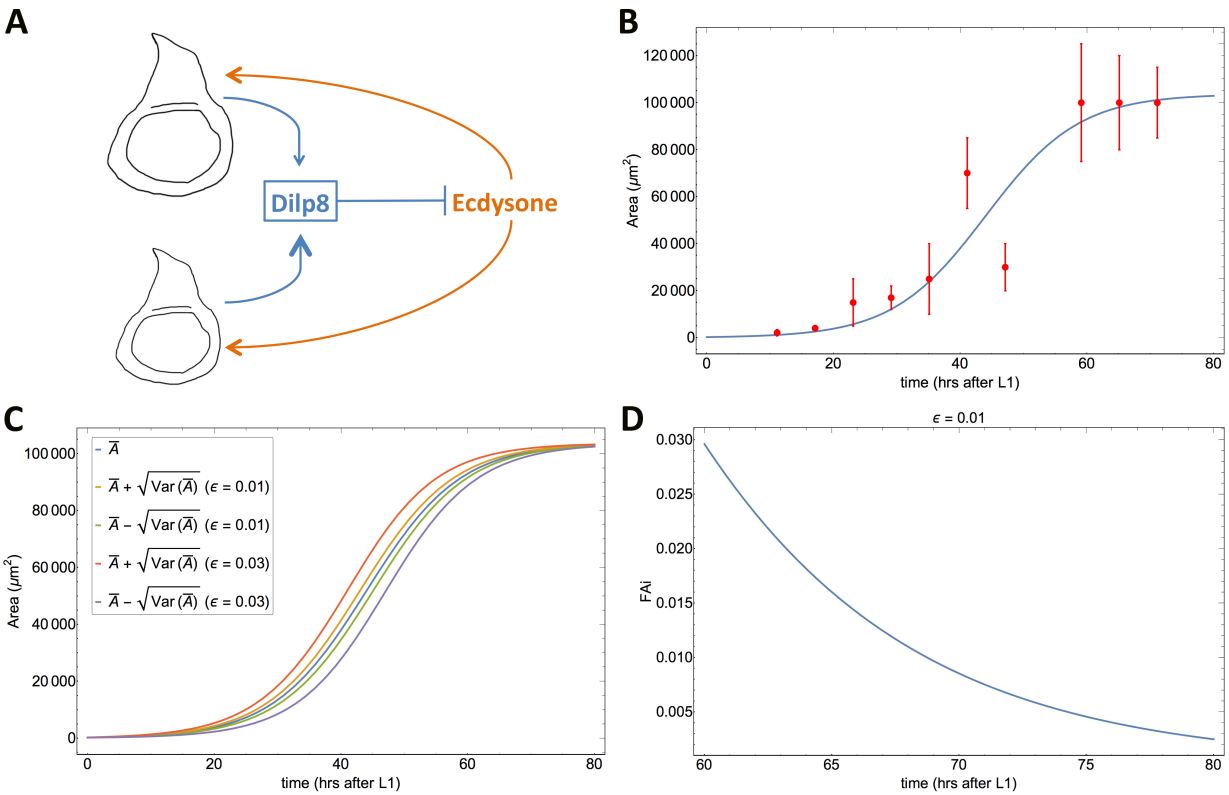

Figure 2.6: Applications to *Drosophila* experiments. (A) Possible negative feedback loop involving Dilp8 and ecdysone based on experimental observations. Larger wing disc (top) is closer to the target size, thus grows more slowly and secretes less amount of Dilp8. Dilp8 secreted by both discs gets mixed up in the hemolymph, the larval equivalent of blood, and inhibits ecdysone, which promotes disc growth. (B) Fitting Bittig et al. data [5] to a logistic curve using Mathematica's nonlinear model fitting function. Error bars represent the experimental errors in their paper. (C) Adding noise to the NC model (Eq. 2.2) and applying small noise approximation allows us to analytically find the variance of the size distribution as a function of time. $\sqrt{\text{Var}(\bar{A})}$ depends linearly on *epsilon*, so higher epsilon will lead to a higher width in the size distribution. (D) For a fixed ϵ FAi monotonically goes down with time near the target size. Thus, in the T model, having the pupariation time or the final FAi uniquely determines the other. L1 refers to the first larval instar. The measurements in Bittig et al. started from the end of L1, and we take that as our initial state.

Predictions for *dilp8* −/− and *dilp8* +/−

By following the same procedure as in the previous section, we can write down Langevin equations for the discs with noises proportional to the square root of growth rates. One subtlety is that feedback correlates the discs, so A_1 and A_2 are not statistically independent anymore Appendix A. FAi now depends on ϵ, the strength of noise, and λ, the feedback strength.

If we have the wild type disc growth data, we can get the feedback strength as a function of the noise strength, $\lambda(\epsilon)$, that produces the correct wild type FA. We can see in Fig. 2.7A that as the noise strength increases, feedback also becomes stronger (more negative) to compensate for the noise and result in the wild type FA. By comparing $\mathrm{Var}(A_1 - A_2)$ normalized by ϵ it is clear that noisy feedback does better compared to having no feedback in terms of noise suppression and lower FA (Fig. 2.4C). Noise suppression also can potentially ensure that both organs are at the same developmental stage at all times, which is crucial in development.

Following the same steps as in the previous section, we can find the pupariation time for *dilp8* −/− mutants by using $\lambda(\epsilon)$ from the wild type data. According to the model, organs in knockout animals follow Eq. 2.2 with $k \to k' = k/(1+\lambda)$. The problem as we discussed is that $k' > k$ and the resulting increase in growth rate leads to less asymmetry late in development because the organs will approach the target size much more quickly and the noise decays faster. Therefore, to get higher FA than wild type, the organs need to stop growing much sooner. In fact, it is easy to see that for any $-1 < \lambda < 0$ growth arrest in knockouts is accelerated more in this model compared to T model, or $\lambda = 0$ (Fig. 2.7B). This is an issue since as in *Drosophila* the pupariation time is not accelerated significantly, and this model then would do worse than T model.

One possible remedy as we explained the is desensitization of organs to the higher growth promoting factors in the absence of the coordination signal. In the case of *Drosophila*, Dilp8 is assumed to control the growth rate by regulating the basal levels of ecdysone in this model. While inhibiting ecdysone production has negative effect on disc growth, feeding ecdysone to wild type flies does not seem to further promote the growth of imaginal discs than normal conditions [49]. This, together with the evidence on the lack of sensitivity of growth rate to the elevated levels of ecdysone in *dilp8* −/− flies lead us to believe that if Dilp8 is a feedback agent, knocking it out should desensitize imaginal discs to the excess amount of ecdysone produced, which in mathematical terms means rescaling k' back to k (or effectively setting $\lambda \to 0$ in FR-P model).

It has also been shown experimentally [2] that at pupariation, average wing disc size in *dilp8* −/− does not have a significant difference compared to wild type flies and the mutant

pupariation time is not significantly shorter than the wild type, which means that in our model, mutant maturation time, t_f^* should be the same as wild type t_f at least in the *Drosophila* example. Alternatively, instead of scaling $k' \to k$, we could find the FAi at the time when mutant average size is the same as wild type average size. For knockouts this is equivalent to the rescaling, but in other mutants like heterozygous, the scaling would be different because heterozygotes still see some feedback and are not fully decoupled, and thus numerically, it is easier to use this condition instead of scaling k'.

With the $k' \to k$ rescaling, we can easily see that the mutant FA at t_f increases monotonically with $|\lambda|$ (Fig. 2.7C). By knowing the FAi of both WT and mutants, we can find the noise strength along with the feedback strength that buffers the noise in the WT.

Using the ϵ and $\lambda(\epsilon)$ found by fitting our model to the wild type and mutant data, we can look at other genetic manipulations and test the model predictions against experimental results. As an example, we now discuss our model's prediction for *dilp8* heterozygous flies. Because heterozygotes produce half the amount of wild type Dilp8, we need to set $c_i = 1/2$ in Eq. 2.12.

We use the ϵ and λ obtained from the *dilp8* –/– FA analysis and find the FA for *dilp8* +/– flies. We also assume that heterozygotes pupariate at the same size as the wild type, which is in agreement with experiments. Our model predicts that heterozygotes have an increased FA compared to wild type, but that this FA is smaller than *dilp8* –/–. *dilp8* –/– has a 2.75-fold increase in FA compared to WT, but *dilp8* +/– show a 1.6-fold increase. The recent experiments also show an increased FA in *dilp8* +/– but the results are currently statistically insignificant.

Temporal Control on *dilp8*

Another possible experiment is time dependent expression of *dilp8* using the temperature sensitive GAL80^{ts} driver to observe for example how late *dilp8* expression could be delayed while still rescuing the wild type FA. In our feedback model, we can look at the final FA starting the FAi some time T^* in the middle of growth. For λ and ϵ, we pick values that would give the wild type FAi if $T^* = 0$ and the knockout mutant if $T^* = t_f$. As we can see in Fig. 2.7D, where the final FAi (normalized by the wild type FAi) is plotted against the time at which *dilp8* expression is turned on (T^*). What we observe is that the final FAi at pupariation stays relatively similar to the wild type FAi up until two thirds through the growth, and only starts to increase for T^* close to t_f.

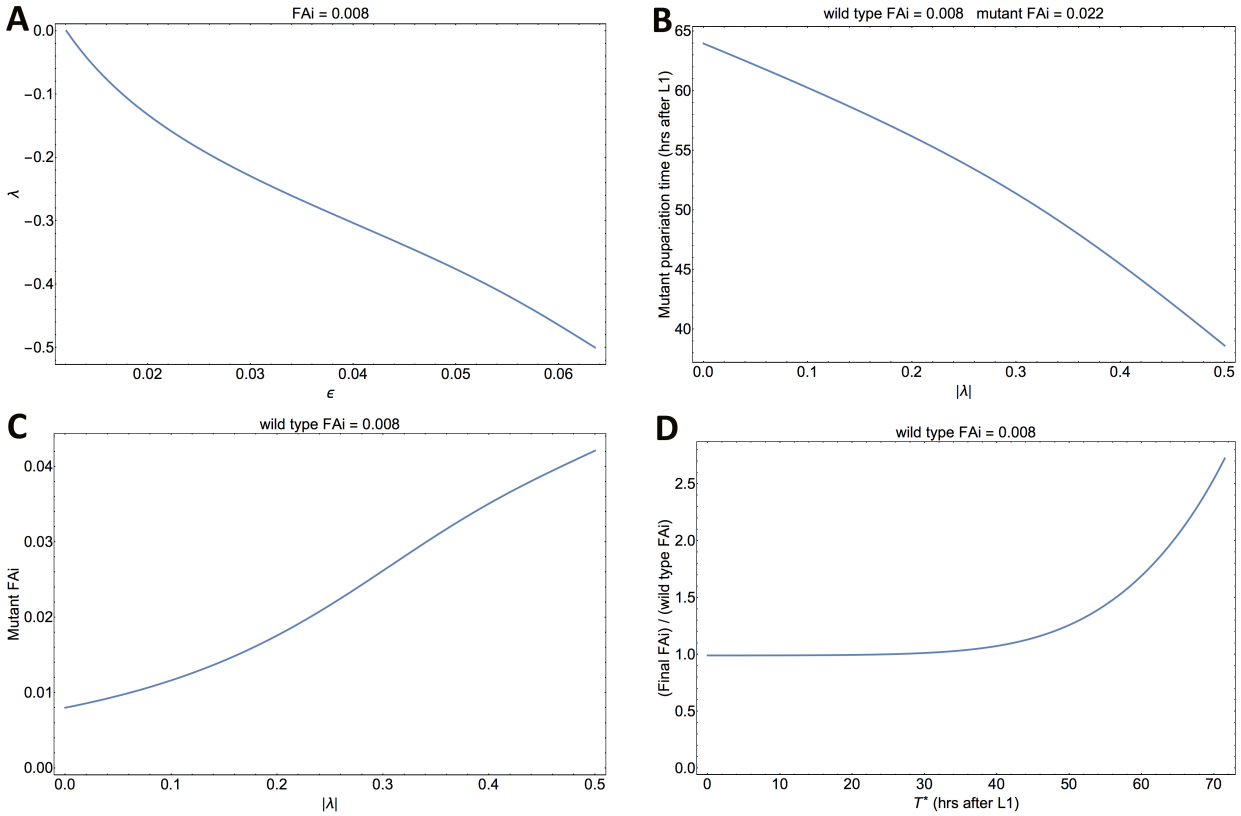

Figure 2.7: Implications of FR-P model for fruit fly experiments. (A) λ vs. ϵ that would give an FAi of 0.8% (wild type FA) at pupariation. As the noise in increased, $|\lambda|$ needs to increase accordingly to lead to the same final FAi. (B) If wings do not desensitize against higher levels of basal ecdysone in *dilp8* –/– background, to get the observed mutant FAi of 2.2%, pupariation needs to be accelerated in FR-P model, with the lowest acceleration belonging to $\lambda = 0$ or T model. (C) With the desensitization to ecdysone in knockouts, mutant FAi will increase monotonically with $|\lambda|$ as expected: higher $|\lambda|$ means that noise is stronger so in the absence of feedback, FAi will be higher. (D) Activation of *dilp8* using the GAL80^{ts} driver at time T^*. The feedback can buffer noise relatively well if it is activated later than usual, and only fails if it is activated close to puparation. This suggests that *dilp8* does not necessarily need to be expressed from the beginning of development and temporal variations in *dilp8* expression do not significantly affect the final FA.

2.5 Discussion

In this chapter, we explored all obvious coordination mechanisms between bilaterally symmetric organs that have an autonomous idea of a target size via a single endocrine signal. Our generic approach to the complicated question of organ coordination enabled us to make predictions about the limitations of chemical signaling in organ development based on simple assumptions on how possible models of coordination look like based on biological constraints.

Specifically, we studied how the notion of target size affects coordination, concluding that it is unlikely to robustly coordinate final sizes with endocrine signaling. This suggests that organs most probably have robust intrinsic mechanisms of error correction that will ensure that each organ can independently reach the correct final size in proportion to the body (see for example [108] for a review of biology and [51, 54, 109] for models describing possible mechanisms). During development, however, feedback can help coordinate organs in response to different fluctuations facilitating maturation in a timely manner. We found that among all the cases considered (Table 2.1), the FR-P model was the most biologically plausible scenario, the most robust against perturbations and can help organs coordinate their sizes during growth. Interestingly, this mechanism is also the most likely candidate for describing the role of Dilp8 in coordinating left and right wings in *Drosophila*.

Particularly, we saw that while FR-P model is unable to correct any possible errors in target sizes, it is not sensitive to how accurately organs interpret the concentration of the signal (represented by c_i parameters). In contrast, all other mechanisms are sensitive to varying degrees to errors in c_i. Notably, both integral feedback mechanisms (FS-I and FR-I) failed to robustly improve errors in final sizes. More specifically, FS-I completely breaks if organs do not perfectly interpret the signal concentration at all times and FR-I model showed a high sensitivity to c_i and initial conditions. This is perhaps somewhat surprising given that integral control is often employed to guarantee a desired steady state [12, 13, 105]. The reason is that normally the error is calculated based on a parameter independent of the input, which determines the steady state value, whereas here the error is calculated with respect to the average size or growth rate.

Even though the fixed point of FS-P model depends on c_i, we note that it is still a well-behaved mechanism and like FR-P model it can lower noise during growth and help organs sync up (Fig. 2.2D). This is indeed a major implication of coordination. Experimentally, the noise levels during growth can be measured by dissecting organs at different instances or using *in vivo* imaging when appropriate to measure sizes and calculate the variance in the difference between the left and right organs of the same animal. It is also worth noting the experimental differences between FS-P and FR-P models. One of the main differences

between these two models is that the coefficient of the feedback signal in FS-P model is positive whereas the coefficient for FR-P model is negative. This can be a distinguishing feature for example if the signal is overexpressed (Appendix A). Specifically, FS-P model is expected to lead to larger final sizes and a lower FA if signal is overexpressed, whereas FR-P model is expected to behave oppositely. Moreover, an organism that follows FS-P model for organ coordination is expected to have significantly smaller organ sizes in mutants (Fig. 2.2B) while in FR-P model no significant reduction in final size is expected.

We also applied our models to the example of *Drosophila*. In *Drosophila*, Dilp8 is the clearest candidate for wing size coordination during larval stage, although Dpp has also been suggested as a signal that leaks out of discs as they growth (thus it also can carry information about growth rate) [110]. From experimental signatures of Dilp8, it is most likely that in normal conditions it follows the FR-P model of coordination (Fig. 2.6A). However, we also explored the possibility that Dilp8 only delays pupariation in physiological conditions and does not affect wing disc growth directly (T model). We saw that it is in fact an unlikely that T model is correct given that the amount by which pupariation is accelerated in mutants is not significant. Regardless, the procedure we outlined can be used in other organisms where T model is suspected to test this hypothesis.

Finally, we used FR-P model to make predictions about different genetic manipulations on *dilp8* in *Drosophila*. We saw that this model predicts desensitization to higher levels of ecdysone in the absence of Dilp8 hormone, which has been observed in before [49]. We also found that in *dilp8* +/– mutants, lower FA than *dilp8* –/– is expected but that FA is still higher than in wild type. This is expected from the model since heterozygotes will produce half the amount of wild type hormone. It has been shown than the FA increase in *dilp8* +/– is not signficant compared to wild type [2]. Whether this means that *dilp8* +/– do not show FA or that more experiments would make the increase more significant remains to be seen. Lastly, we looked at temporal control on *dilp8* expression using the temperature sensitive GAL80^{ts} driver. We saw that there is some tolerence regarding the timing of *dilp8* activation (Fig. 2.7D); expressing *dilp8* as late as mid-third instar seems to still lead to a final FA close to wild type at pupariation.

Size coordination is useful as it helps organs 1) stay coordinated during growth and in response to different environmental fluctuations, and 2) stop growing sooner and keep their symmetry since it helps organs lower their developmental noise sooner. The latter is particularly useful for *Drosophila* as it is known to have a fast developmental timing. However, this does not exclude the possibility that organ coordination is not needed during normal growth and is only activated in response to significant growth perturbations (NC model).

This indeed seems to be the case in mice [45]. Then, in normal conditions, the coordination signal may be involved in organ autonomous error correction mechanisms by regulating, say, cell apoptosis. If this is the case, knocking out the signal would still lead to in increased FA, but it is possible that heterozygotes still have enough amount of the hormone and do not show significant FA compared to wild type. In terms of our models, these mechanisms can amount to a control on noise in target size or the strength of the noise, ϵ in Eq. 2.2. In Appendix A we briefly explore these cases in more detail.

Another possibility is the idea of "catch up" growth, which suggests that if an organ's growth is interrupted, that organ intrinsically modulates its growth rate to catch up to the unperturbed organ. If in an organism there is no feedback and instead the catch up growth is involved, organs need to individually respond to stresses and damages. Previously, models of size correction have been studied for individual organs [111]. The catch up growth hypothesis was recently observed in the development of fish ear [92].

One of the main limitations of our models is that they only consider two organs yet it is definitely possible that several organs participate in the same feedback mechanism. For example, in *Drosophila* coordination has been observed between wing and eye discs [44, 46]. If all organs have the same target size, our model can be extended to include N coupled organs. If however organs have different target sizes because they are different organs, the same model can still be applied and each organ just needs to individually interpret the signal properly based on internal mechanisms. Overall, no qualitative changes to our main results are expected. Furthermore, the coordination signal could be involved in multiple mechanisms at once, but even if that is the case, the major signatures of these models will still be relevant.

Finally, our model does not say anything about shape asymmetry. However, organ shapes also show low FA [30]. Recently a mechanism for shape control in *Drosophila* independent has been proposed [112] that is independent of what individual cells do, thus it would be interesting to build generic mathematical models to investigate the possibility of shape control through global or local mechanisms and whether a secreted hormone can have a role in correcting errors in organ shapes as well as organ sizes.

CHAPTER 3
Size and Shape Asymmetry in *Drosophila* Wings

In the previous chapter, we discussed the concept of fluctuating asymmetry (FA) in developing left/right organs drawing inspiration from *Drosophila* wing development and the role of the hormone Dilp8 in regulating the final FA in wing surface area. The observed wing area FA in wild type flies is less than about 1% and *dilp8* –/– mutants show a small but significant increase in FA [1, 2, 29]. However, more information about the FA distribution is lacking. For example, one important question that needs to be answered is what the distribution of FA looks like in different genotypes. Does FA in both wild type and *dilp8* –/– have a distribution of the same shape but differet mean, or does the FA distribution in *dilp8* –/– have a longer tail for instance? Quantifying the FA distribution can help us better understand the mechanistic role of Dilp8 in regulating FA and can inform us in developing more biologically relevant models. Another question one could ask is whether Dilp8 also affects shape asymmetry. For example, it would be interesting to see if the pattern of veins in *dilp8* –/– flies is more varied between left and right wings. In fact, it has been reported, though without citation of any published data, that vein patterns are more varied among *dilp8* –/– flies [113]. Thus, quantification of such a variability would be crucial. Answering these questions inspired us to work on image segmentation algorithms to automate area FA measurements and to quantify shape asymmetry in adult *Drosophila* wings.

In this chapter, dedicated to a collaboration with the biology lab of Pierre Leopold in France, we will discuss the procedures involving mounting, imaging fly wings, using image analysis techniques to measure size and shape FA in different genetic backgrounds, and error analysis. The organization of this chapter is as follows: First we give a brief outline of the mounting and imaging procedure. Then we discuss the shortcomings of the manual segmentation method currently employed by most biologists and motivate automating the process. Next, we will explain the wing segmentation algorithm. And finally we will discuss the quantification of shape asymmetry using the Procrustes method adopted from [30].

Unfortunately, we will not present any final results for wing area and pattern FA. The

reason is that the fly samples that we collected for our analyses did not match the previously reported area FA, which we believe may be due to mislabeling of our samples. Therefore, we have postponed final measurements and detailed error analysis of our codes until we receive new images from our collaborators. In what follows, we will only discuss our methods.

3.1 Image Analysis of Adult Wings

Imaging adult *Drosophila* wings is a relatively straightforward task as far as biological experiments are concerned, and it turned out to be more or less theorist-friendly. To mount adult wings, we followed the protocol used in [2] as follows: First, wings of dead flies (courtesy of Leopold Lab) are clipped in ethanol using forceps under a microscope one by one. Care must be taken not to damage the wing in the process as wings are very delicate. Each wing is then dried and submerged in a Euparal solution, a mounting medium, on a glass slide making sure that left and right wings are placed with the right orientation relative to each other so that later on we can tell them apart. After mounting wings on the slide, a cover slip is placed on top of the wings to spread out the mounting medium and keep the wings flat. Then, slides are incubated at 60°C overnight for bubbles to dissipate while the medium slowly polymerizes. A small weight is also placed on top of the cover slip during this process to ensure that the wings stay flat and are not wrinkled. After the incubation process, wings are permanently fixed on the slide and can be imaged. An example image of a right wing is shown in Fig. 3.1. Images were taken using a Leica M205 FA florescence stereo microscope with a Leica MC190 HD digital camera at 40× magnification. We note that in another common method, instead of using Euparal, wings are mounted in lactic acid, which does not require incubation allowing for faster mounting [114] and is now being employed by the Leopold lab; however, in this method wings are not mounted permanently.

3.1.1 Manual Segmentation and its Issues

Traditionally, wing area measurements have been done by manual segmentation of wing images. However, there are obvious problems with manual segmentation that make it less than ideal. Firstly, manual segmentation is prone to errors as a human needs to draw a contour around the wing by eye. From Fig. 3.1 we can see that the periphery of the wing is surrounded by a thick vein that slowly becomes thinner as it wraps around the wing in clockwise fashion, which is itself covered in bristles. This causes ambiguities in where to draw the contour line. This is particularly problematic since *Drosophila* wings show very small FA values even in knockout mutants, so small measurement errors can lead to significant

Figure 3.1: A bright field image of the right wing of a wild type fly.

uncertainties. Secondly, manual segmentation is an extremely tedious task that needs to be repeated for tens of pairs of wings for each genotype to be able to say anything statistically meaningful about the fold change in FA between different genetic backgrounds. What's more, finding the FA distribution requires many more measurements than biologists typically do to find the FA, which would be very time consuming and impractical to do manually.

These issues with manual segmentation motivated us to look for a way to automate the process. For this purpose, we wrote a short code in MATLAB to automatically segment the wings and find the area FA. Our goal was to have a simple code with few free parameters (so that people unfamiliar with coding can also benefit from it) that is fast and reliable, and performs at least as well as manual segmentation. The wing segmentation algorithm is outlined in the following section. We used the Imgae Processing Toolbox in MATLAB edition R2018a for the analyses in this chapter.

3.2 Adult Wing Segmentation Algorithm

In this section we outline the wing area segmentation algorithm that can be used to find wing area FA in a short amount of time, hence making it attractive for analysis of large sample populations. Manually, the most reasonable way to segment is to crop through the

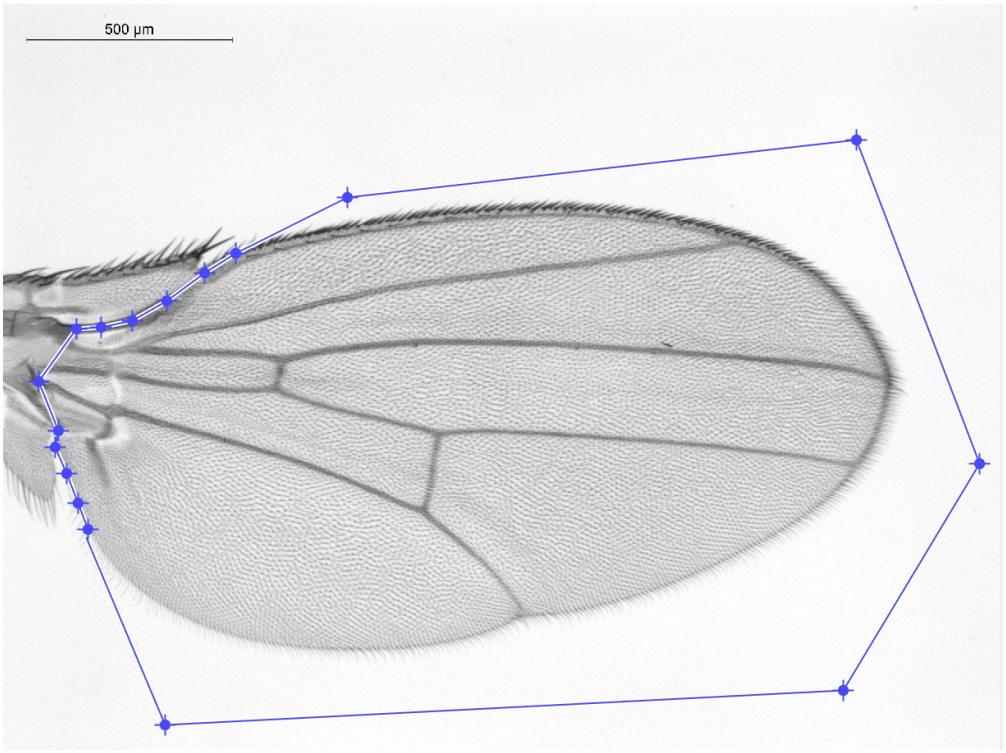

Figure 3.2: The ROI specified by the user. The user only needs to accurately specify the where on the hinge the wing is to be segmented; the rest of the wing blade will automatically be identified by the program. The circles show the locations of mouse clicks specifying the vertices of the ROI polygon.

middle of the thick vein at the edge of the wing blade, thus excluding the bristles. The main challenge in automating the process is that those bristles make a simple thresholding method futile. Our method gets around this issue by effectively "cutting" the bristles out. The way we get around this issue is by using a skeleton of the outer vein to effectively make a cut through the edge of the wing blade and remove the bristles from the segmented wing. The code outlined below is in the Live Script (MATLAB notebook) for user accessibility.

First, the user needs to specify where along the hinge they want the wing to be cut using a polygon selection tool `roipoly(Image)`. This is the only part of the program that is not currently automated, the reason being that there is not an obvious pattern or structure on the hinge to use for segmentation. Therefore, this part of the wing needs to be segmented manually but because it is a small region, the manual ROI selection is quite fast. In Fig. 3.2 we show an example of a reasonable ROI selection.

After this, two separate thresholds are applied to the input image. One is a simple global thresholding with a cut off set automatically by MATLAB based on the global histogram and using Otsu's method, an optimal thresholding method [115]. This global threshold segments the whole wing including the bristles. After morphological operations, we get an image like

the one in Fig. 3.3, which we call initial segmentation. These operations are shown in the Listing 3.1. We first fill the holes after the global threshold, then apply morphological closing and opening to smooth out the bristles and close any openings inside the wing, then fill any remaining holes. Finally, we erode the image as a control mainly on the bottom edge of the wing. Depending on the resolution of the image, the size of erosion needs to be set manually once to get the desired output. The larger the size of erosion is, the more the bottom half of the edge will shrink in the final segmentation. Erosion is necessary to exclude the short hairs at the bottom half of the wing periphery.

Listing 3.1: Initial segmentation

```
BWs = 1-imbinarize(Image); %global threshold

%%morphological operations on the global threshold
BWdfill = imfill(BWs, 'holes'); %fill the holes

seD = strel('diamond',10); %size of erosion. recommended: 10
seC = strel('disk',3); %radius of closing. recommended: 3
seO = strel('disk',5); %radius of opening. recommended: 5
BWfinal = imclose(BWdfill,seC);
BWfinal = imopen(BWfinal,seO);
BWfinal = imfill(BWfinal, 'holes'); %fill any remaining holes
%erodes the image
BWfinal = imerode(BWfinal,seD);
```

Before applying the other threshold, a Gaussian filter is applied to the input image to blur out some of the fine details such as trichomes on the surface of the wing. The standard deviation of the filter is set by the user, which specifies the amount of blurring. Later we explain how to pick a reasonable value for this parameter. The second threshold is an adaptive one which is chosen using local first-order image statistics around each pixel. The result is a binary image that only identifies the veins, which locally have different intensity than their surroundings — we call this image the 'skeleton' of the wing (Listing 3.2). This threshold has a sensitivity parameter that needs to be set by the user. Together with the standard deviation of the Gaussian blur, these two parameters control the resulting skeleton. The user needs to tune these two parameters such that the skeleton shows the the top half of the wing periphery up until the point where the third inner vein touches the periphery, but not much beyond that (Fig. 3.4).

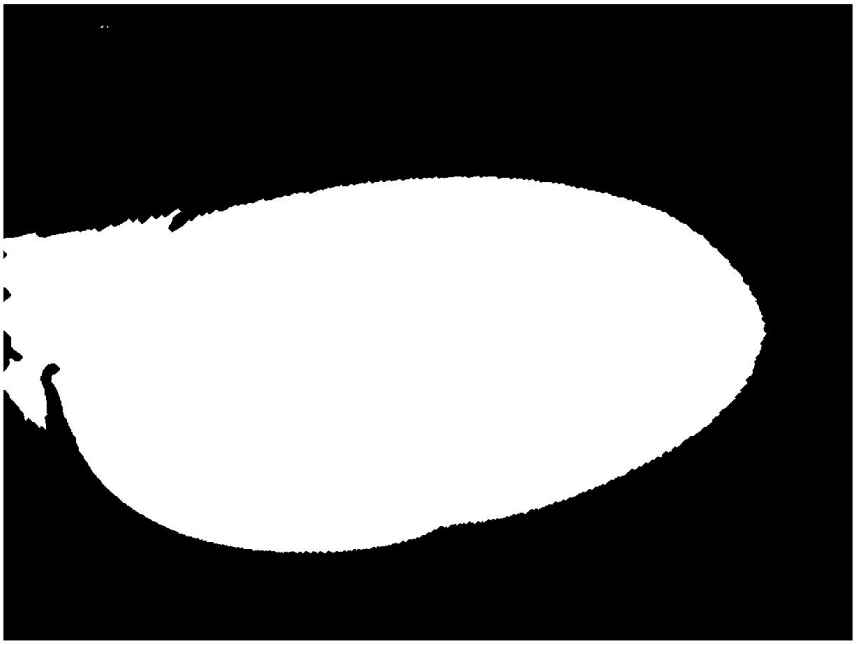

Figure 3.3: The global threshold segments the whole wing, including the unwanted edge bristles.

Listing 3.2: Second segmentation

```
1 Iblur = imgaussfilt(Image, 10); %blurring the image with standard ...
      deviation 10
2 %adaptive threshold with sensitivity = 0.78
3 BWs2 = 1-imbinarize(Iblur,'adaptive','Sensitivity',0.78);
```

The proper values for these parameters depend mainly on the imaging variables such as resolution, exposure, etc. As long as these variables are consistent among all acquired images, standard deviation and sensitivity parameters will not need to be tweaked a lot once tuned for one image. Higher standard deviation leads to a smoother image with less defined structure, and thus a smoother skeleton (see Fig. 3.4B with Fig. 3.5 for a comparison between standard deviation of 10 and 4). Generally, a smoother skeleton will give us a cleaner final segmentation. Higher sensitivity leads to a skeleton with less of the wing structure visible (Fig. 3.4).

After the skeleton is produced, we further thin the skeleton using MATLAB's `bwmorph` function. The thinning process reduces the skeleton to lines of a single pixel width. We then multiply the initial segmentation shown in Fig. 3.3 by the inverse of the thinned skeleton to effectively make a cut through the bristles. This cut essentially separates the bristles around the periphery of the wing from the rest of the wing blade (Fig. 3.6A) allowing them to be

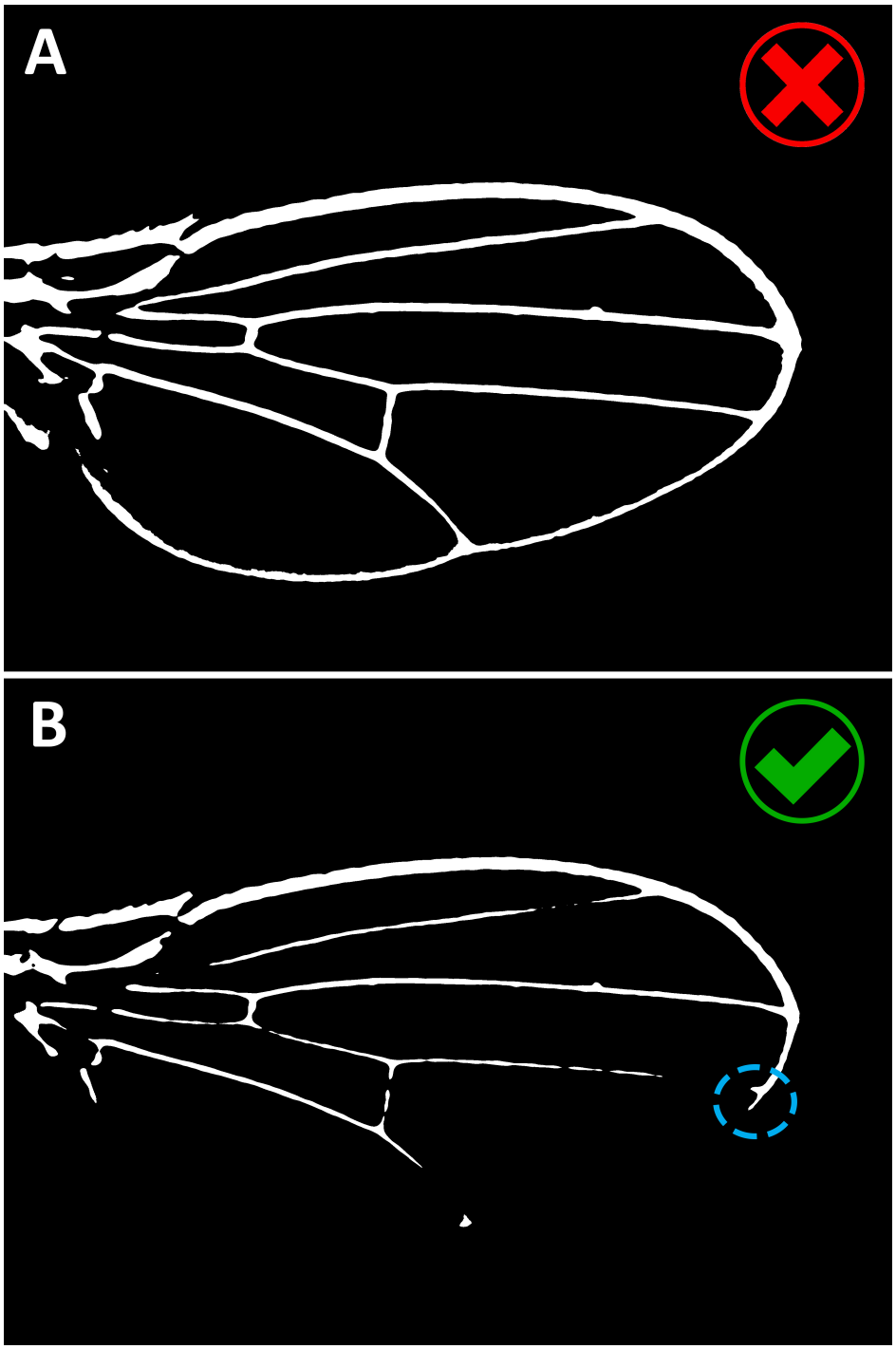

Figure 3.4: Two adaptive thresholds with standard deviation of 10 pixels and different sensitivities. (A) An example of a improper adaptive threshold (sensitivity of 0.69). This threshold is not useful as the bottom half of the periphery in the resulting skeleton will remove parts of the actual wing blade from the segmented image. (B) An example of a proper adaptive threshold (for this test wing, sensitivity was 0.78). The periphery is visible up until the third horizontal vein crossing but does not extend to the fourth vein crossing near the bottom of the wing. The blue dashed circle indicates where the periphery should extend based on our experience: a little after the third vein crossing but not much further.

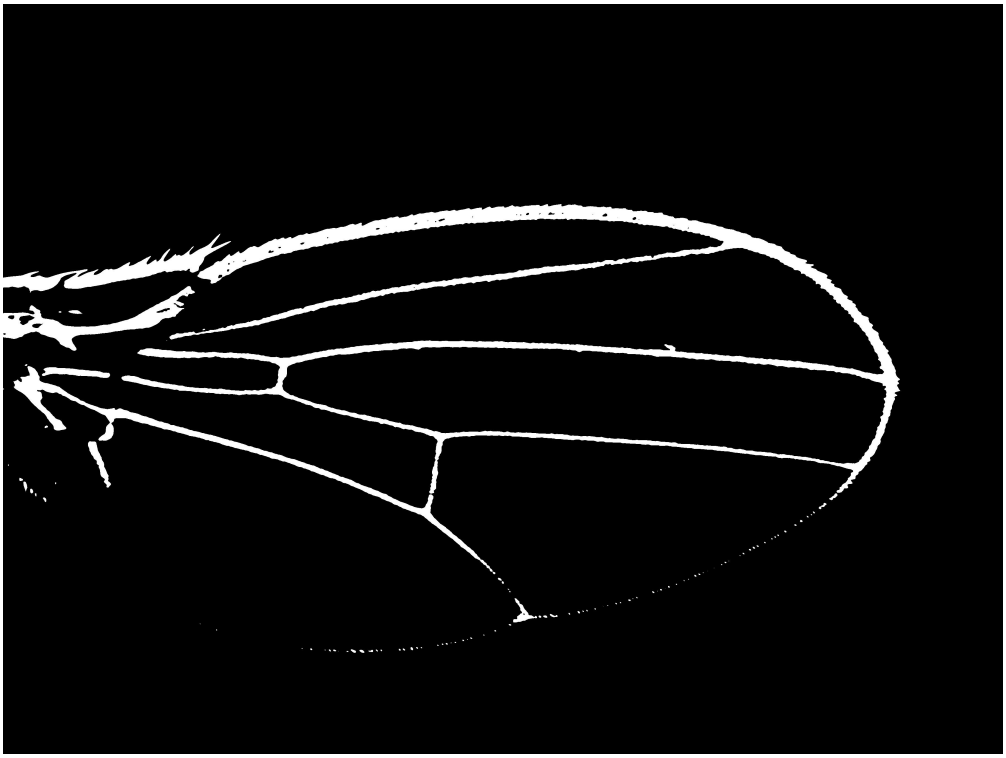

Figure 3.5: An adaptive threshold with sensitivity 0.78 and standard deviation of 4 pixels. The detailed structure of the wing and particularly the bristles make this skeleton undesirable.

removed using morphological opening. The radius of this morphological operation is set by the user such that the result no longer has the bristles but other parts of the wing are mostly intact. The result is shown in Fig. 3.6B. We can see in Fig. 3.6 that the multiplication has also cut through the inner veins. This can easily be filled using morphological closing after we have removed the bristles. Listing 3.3 shows the procedure.

Listing 3.3: Cutting through the initial segmentation

```
skeleton = bwmorph(BWs2,'thin',inf); %thinning the skeleton
%make a cut through the initial segmentation
BWfinal2 = (1-skeleton).*BWfinal;

%remove the cut out bristles with morphological opening
BWfinal2 = imopen(BWfinal2,strel('disk',20));
%pick the largest connected component. Useful when there are leftover ...
    pieces that we don't want
BWfinal2 = bwareafilt(logical(BWfinal2),1,4);

%morphologically close to fill out the interior cuts
BWfinal2 = imclose(BWfinal2,strel('disk',30));
BWfinal2 = imfill(BWfinal2, 'holes'); %fill any remaining holes
```

Finally, we do one more round of smoothing by first, blurring the image in Fig. 3.6B using a Gaussian filter, and then re-thresholding the blurred image to get the smoothed image (Listing 3.4).

Listing 3.4: Final smoothing

```
BWfinal3 = BWfinal2;
blurryImage = imgaussfilt(double(BWfinal3), 50);
BWfinal3 = blurryImage > 0.5;
BWfinal3 = J.*BWfinal3;
```

After applying the ROI mask to this smoothed binary, we get the final segmented wing. This is shown as a red shading of the original image in Fig. 3.7. The code outputs the area of this segmented image, which can be used for area FA measurements. We have used our code on several sets of images which had been already segmented manually, and in all cases the FA values we found using the code has agreed with the manual method.

Possible sources of error are the standard deviation of the Gaussian filters (both for the blurring in Listing 3.2 and smoothing in Listing 3.4), the sensitivity of the adaptive

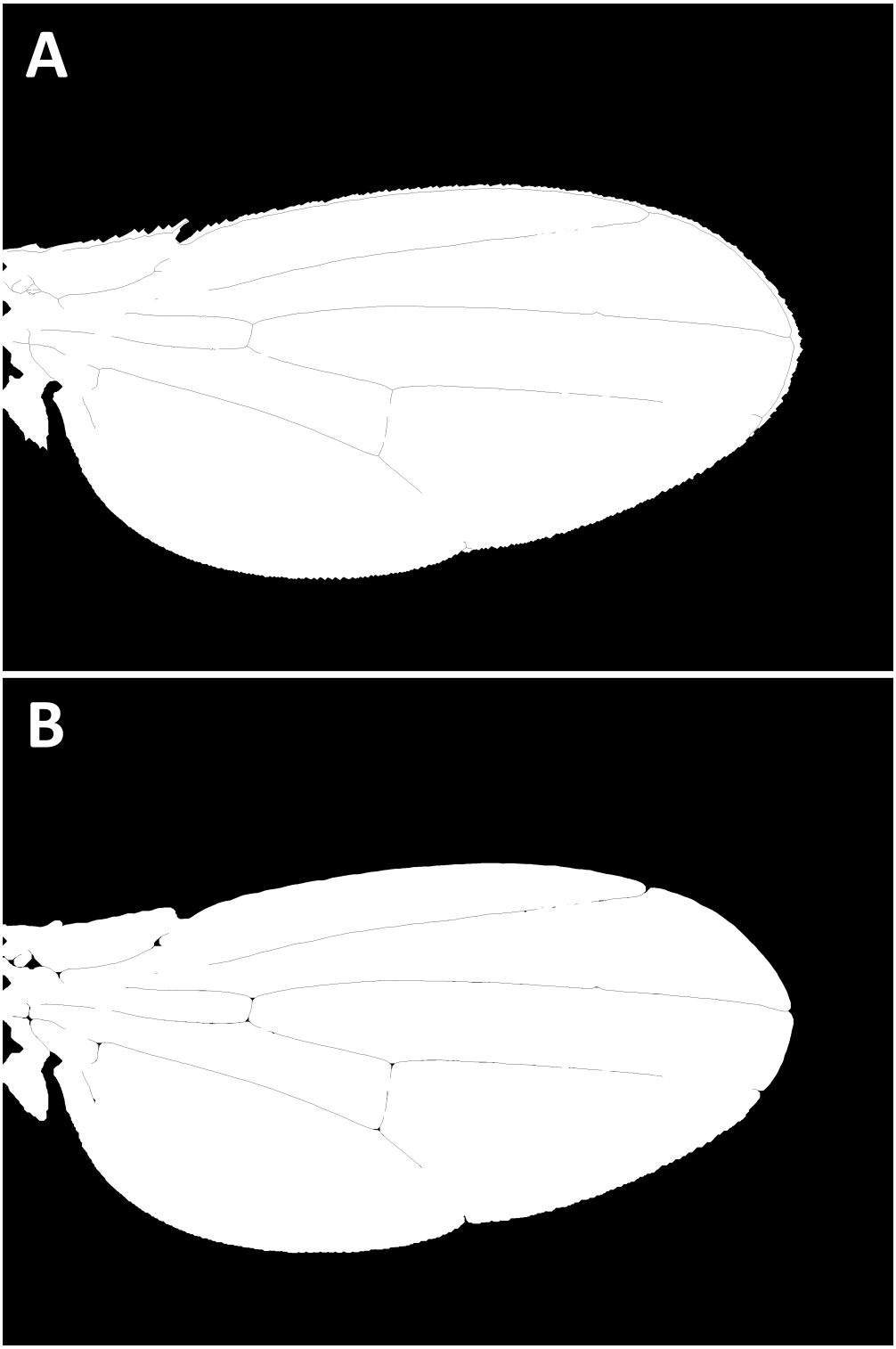

Figure 3.6: (A) Multiplying the initial segmentation by the inverted thinned skeleton results in an effective cut through the segmented wing. (B) Applying morphological opening to the image removes the bristles from the edge of the wing.

threshold (Listing 3.2), and morphological operations. Since the standard deviations of Gaussian filters and the threshold sensitivity parameter are the main parameters that need to be set by the user, we varied them to see how sensitive the outcomes are to these parameter choices, finding that the final result is not sensitive to small changes in these parameters. In particular, we first picked a pair of wild type wings. For this pair, the FA, defined as $2(A_{left}-A_{right})/(A_{left}+A_{right})$, was found to be -0.017 (which notably is high for wild type). We then varied the adaptive threshold from 0.75 - 0.77, the standard deviation of the first Gaussian filter from 7 - 10 pixels, and the standard deviation of the second Gaussian filter from 30 - 50 pixels, and ran the segmentation code seven times for the pair, each time with different parameter values. The ranges of parameters were decided such that skeleton of the image followed the condition in Fig. 3.4 and the final segmented image looked reasonable to the eye. The standard deviation of the resulting area measurements were 0.05% and 0.04% of the left and right wing areas respectively suggesting that the algorithm is not sensitive to these parameters.

We further tested how the pairwise measurements were affected by calculating the FA of each outcome, which was consistently about -0.017. Pairing up outcomes with the same parameter values, the standard deviation of these FA values was 2×10^{-4} while for randomly paired outcomes, the standard deviation in the FA values was 6×10^{-4}. Notably, standard deviation of $2(A_{left} - A_{right})/(A_{left} + A_{right})$ is the FAi (defined in Chapter 2, Eq. 2.17) if it is calculated across the population (but with A_{left} and A_{right} of the same fly). For wild type, FAi is about 1%, so variations due to parameter choices are more than an order of magnitude smaller than the observed FA, again suggesting that the algorithm is not sensitive to choices of parameters.

3.3 Wing Shape Asymmetry

In this section, we outline a code for measuring the wing shape asymmetry. As a measure of wing shape, we focus on vein patterns and in particular, the location of vein crossings. This method is adopted from a study by Abouchar et al. [30]. In their paper, Abouchar et al. found the location of seven vein crossings called landmarks on each wing, and used the so-called Procrustes transformation to analyze the difference between the location of these seven landmarks across different wings finding that the variability in vein crossing patterning is less than or equal to a single cell size in wild type. The idea of Procrustes method is to scale all wings to the same size (thus removing size asymmetries) and rotate them in such a way to get rid of rigid rotations. This method guarantees that the resulting variance in the location of the landmarks is purely due to pattern asymmetries. Following their analysis, we

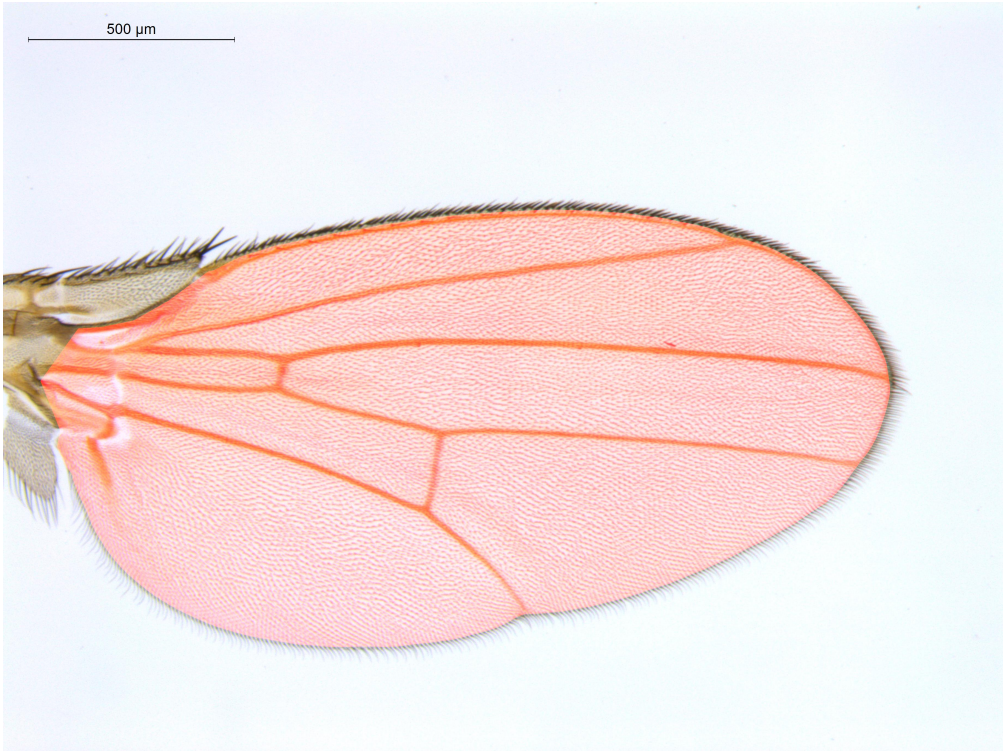

Figure 3.7: The final result of the wing segmentation algorithm. The red shade shows the final segmented image, imposed on the original image.

find the location of these seven landmarks (shown in Fig. 3.8) on each of our wings using a simple MATLAB code, then use the Procrustes method to find the pattern FA between left and right wings. The procedure is outlined below.

3.3.1 Finding Vein Crossing Landmarks

Firstly, we mirror the left wing images to have the same orientation as right wings. The input image[1] first needs to be blurred using a Gaussian filter and thresholded by the same adaptive threshold introduced in Section 3.2 (Listing 3.2) to visualize only the veins. The Gaussian blur standard deviation and threshold sensitivity need to be chosen such that all seven vein crossings of interest are visible. Speaking out of experience, it is mostly sufficient to set these parameters based on one image and not change them for the rest of the images in the set, and the same parameter values as in Listing 3.2 work in this analysis as well.

Next, the skeleton will be thinned down to lines. At this stage, the user specifies the seven landmarks one by one by drawing a small polygon encompassing each landmark. After each polygon is drawn, the algorithm finds the vein crossing by finding the intersection of

[1]Note that wings need to have the same orientation for our analysis. We decided to mirror images of left wings.

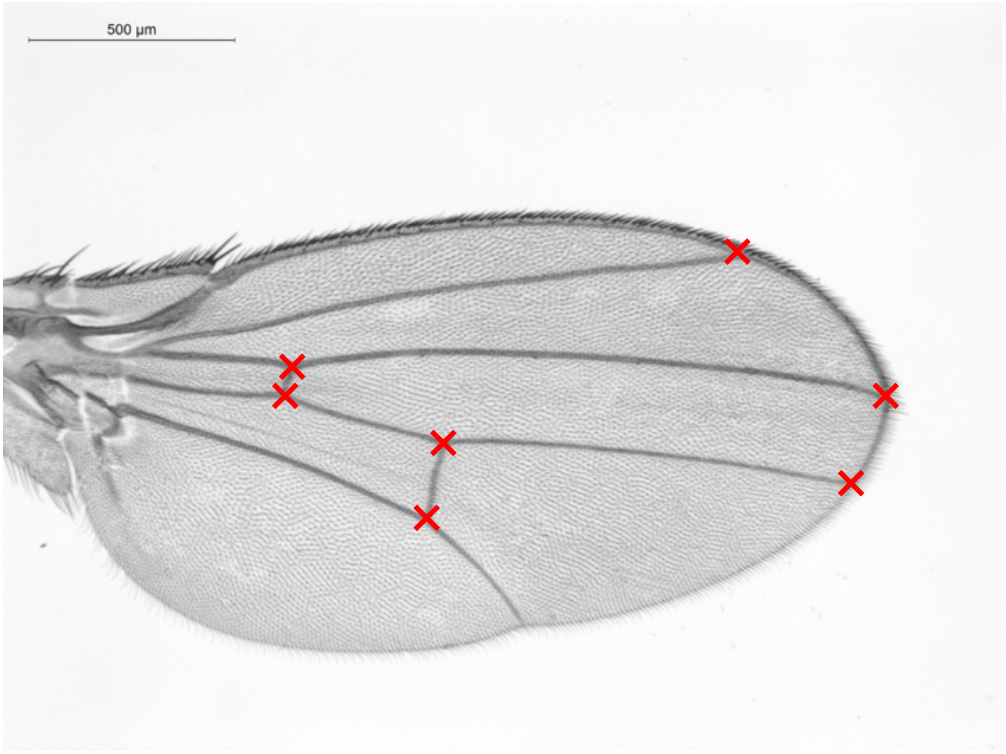

Figure 3.8: Seven landmarks used for pattern FA analysis marked on the wing.

the lines inside the polygon (Listing 3.5).

Listing 3.5: Finding the landmarks

```
x = zeros(1,7);
y = zeros (1,7);
for i =1:7
    roi = roipoly(skeleton);
    crossing = bwmorph(roi .* skeleton,'branchpoints');
    [y(1,i),x(1,i)] = find(crossing);
end
```

After all seven polygons are drawn by the user, the program saves the list of the seven landmark coordinates in a file. The user repeats the same procedure for each wing making sure to specify landmarks in the same order for all images. We note that Abouchar et al. used a different method in finding the vein crossings by finding the center of each vein close to the crossings from the intensity profile across the vein and then estimating the crossing as the centroid of extrapolated lines that denote the center of each vein [30]. Even though their method is more concrete, our final results agree with theirs fairly well (see the next Section), so we decided to continue with our method based on skeletonization.

After all wings are processed, the coordinate files are read by a separate code that performs the Procrustes transformation and asymmetry measurements.

3.3.2 Procrustes Transformation and vein Pattern FA

The Procrustes transformation first translates each configuration of landmark coordinates $(X_{0,i}, Y_{0,i})$ ($i = 1, \ldots, 7$ denotes each of the landmarks on a given wing) to a common origin by subtracting the average position of the seven landmarks from each landmark in each set. The algorithm then scales each set of now translated coordinates (X_i, Y_i) by the centroid size $S = \sqrt{\sum_{i=1}^{7}[X_i^2 + Y_i^2]}$:

$$(x_i, y_i) = \frac{1}{S}(X_i, Y_i). \tag{3.1}$$

S is a linear measure of the size of the wing, therefore scaling the coordinates by it effectively removes variability in sizes across different wings. Finally, the set of normalized coordinates (x_i, y_i) of each configuration is rotated to be as close as possible to other configurations, thus subtracting the variability due to rigid rotations. To do this, the average of all configurations was chosen as the reference coordinate (x_i^{ref}, y_i^{ref}) and all configurations were rotated according to:

$$(x_i^r, y_i^r) = (x_i \cos\theta - y_i \sin\theta, y_i \cos\theta + x_i \sin\theta) \tag{3.2}$$

with

$$\theta = \tan^{-1}\left(\frac{\sum_{i=1}^{7}\left(x_i y_i^{ref} - y_i x_i^{ref}\right)}{\sum_{i=1}^{7}\left(x_i y_i^{ref} + y_i x_i^{ref}\right)}\right), \tag{3.3}$$

where (x_i^r, y_i^r) denotes the coordinates of landmark i after rotation. θ is chosen this way to minimize the sum of the squared distances between (x_i, y_i) and (x_i^{ref}, y_i^{ref}).

To get a single value for variability between the sets, we construct the 14×14 covariance matrix C of the coordinates (7 landmarks with 2 coordinates each) and define the variability as the square root of the unbiased variance across the configurations, i.e.

$$\Sigma = \langle S \rangle \sqrt{\frac{1}{10}\mathrm{Tr(C)}} = \langle S \rangle \sqrt{\frac{1}{10}\left[\sum_{i=1}^{7}\mathrm{Var}(x_i) + \sum_{i=1}^{7}\mathrm{Var}(y_i)\right]}, \tag{3.4}$$

where $\langle S \rangle$ is the average centroid size in the set of wing images being analyzed. $\mathrm{Var}(x_i)$ means the variance in the x-coordinate of the i'th landmark across all configurations. The unbiased variance is obtained by considering the number of degrees of freedom for the Procrustes transformation, i.e. we need to subtract 4 (2 degrees for translation, 1 for scaling and 1 for rotation) from 14, the total number of coordinates.

Σ gives the pattern variability for all wings. More specifically, to find the pattern FA, we define

$$\Sigma_{L-R} = \langle S \rangle \sqrt{\frac{1}{10}\left[\sum_{i=1}^{7} \mathrm{Var}(x_i^L - x_i^R) + \sum_{i=1}^{7} \mathrm{Var}(y_i^L - y_i^R)\right]}, \tag{3.5}$$

where the superscript L refers to the coordinates of the left wing and R refer to the right wing. In Fig. 3.9 we show the transformation results for a set of 38 pairs of supposedly wild type wings. For this set, we found $\Sigma = 7.3\mu$m and $\Sigma_{L-R} = 6.9\mu$m consistent with the values reported by Abouchar et al [30]. The area FAi for this set was found to be 0.016 (confirmed with both manual and our automated segmentation), which is too high for wild type, leading us to believe that some of the flies in the set may have been mislabeled.

We have also looked at the error of the algorithm in finding vein crossings by running the algorithm several times on a single image while changing the threshold sensitivity or the Gaussian blur standard deviation. Σ was then calculated for the outcomes (but with 14 degrees of freedom instead of 10 since the Procrustes transformation was not applied here) finding that Σ was consistently well below the reported size of a single cell ($13.0\pm0.7\mu$m [30]). For instance, for an image we varied the Gaussian blur standard deviation from 6 - 15 pixels while fixing the threshold sensitivity at 0.73, finding $\Sigma = 1.46\mu$m, while fixing Gaussian blur standard deviation at 10 pixels and varying the threshold sensitivity from 0.68 - 0.78 lead to $\Sigma = 1.81\mu$m. This suggests that the algorithm is not very sensitive to changes in the sharpness of the image or the sensitivity of the adaptive threshold. For reference, all three images shown in Figs. 3.4 and 3.5 would be reasonably acceptable for the algorithm.

3.4 Discussion

In this chapter, we examined image analysis of adult *Drosophila* wings from two angles:

1) We presented an automated, more efficient alternative to manual wing segmentation for calculation of wing area FA. This alternative method eliminates the strenuous and error-prone segmentation by hand. As we discussed, the user still needs to manually specify where the wing needs to be segmented along the hinge, which has the potential for errors, but we argue that the algorithm minimizes errors by limiting the variability introduced by human errors and being more consistent across the set of images. As we showed in Section 3.2, the error introduced by the choice of parameters was insignificant. Furthermore, we tested for the magnitude of the error introduced by the manual ROI selection by segmenting the same wing five times using the same parameters and each time re-selecting the ROI. We found that the standard deviation of the resulting areas was three orders of magnitude smaller

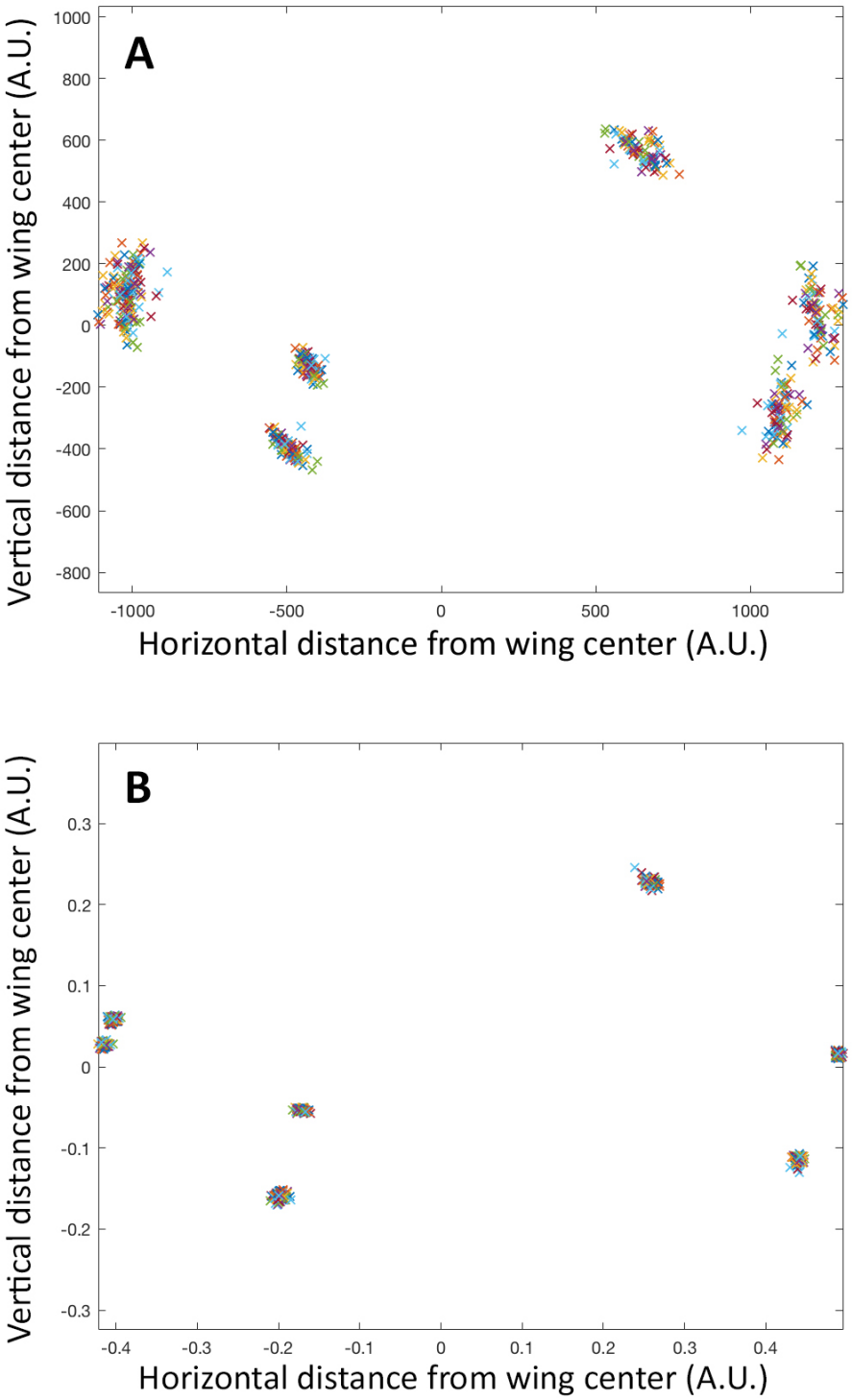

Figure 3.9: An example of the Procrustes transformation for a set of 38 pairs of wings. (A) Vein crossing landmarks after translating each configuration to the common origin. (B) Landmarks after scaling and rotating the configurations. Each cluster shows the variability among 76 wings for each landmark. For this set, $\Sigma = 7.3\mu$m.

than the average area of those five measurements. The most important advantage of this code, however, is its relative speed compared to manual segmentation. Whereas manual segmentation, if done carefully, can take about 2 minutes for each wing, the code, once the parameters are properly set, takes less than 30 seconds to run, making it more than 4 times faster than manual segmentation.

2) We also discussed wing shape FA in the context of vein patterning variability between different wings, and in particular the relative location of seven vein crossings shown in Fig. 3.8. Studying the variability in these seven landmarks is perhaps the most obvious and simplest first choice in quantifying the shape FA. We tested the algorithm for a set of wild type wing images acquired in France and found a shape FA comparable with the results reported in [30], however, because the area FA's of the wild type and *dilp8* –/– flies did not agree with reported values, we think the flies might have been mislabeled at collection, so we have not been able to conclude this analysis.

One extension of this analysis would be to include the eighth vein crossing at the bottom of the wing. The reason that we did not include it in the first place was that in [30] the authors show that including it does not affect their final results about variability in vein patterning in the genetic backgrounds that they studied. However, in our case, *dilp8* –/– mutants could potentially show significant patterning variability at that crossing, so it would be interesting to include that in our analysis as well. Of course, this only amounts to minor modifications in our code, and additionally, to obtain the unbiased variance, Tr(C) needs to be divided by 12 and not 10 to account for two extra degrees of freedom for the extra landmark.

Other sources of errors other than the ones we mentioned (i.e. parameters of the algorithms) are imaging errors. When taking an image, there are several parameters that need to be set such as the light intensity, focus, magnification, as well as the orientation of the sample. All of these parameters can introduce errors of their own, however, these errors do not appear to be significant [30].

Finally, once we have access to new sets of images with enough number of wings, we would be able to measure area and pattern asymmetries and hopefully, we can extract useful information about the FA distribution in different genotypes.

CHAPTER 4

Statistics of Noisy Growth with Mechanical Feedback in Elastic Tissues

Ojan Khatib Damavandi and David K. Lubensky
Department of Physics, University of Michigan, Ann Arbor, Michigan 48109-1040, USA
(Published in PNAS Mar 2019 [116])

4.1 Abstract

Tissue growth is a fundamental aspect of development and is intrinsically noisy. Stochasticity has important implications for morphogenesis, precise control of organ size, and regulation of tissue composition and heterogeneity. Yet, the basic statistical properties of growing tissues, particularly when growth induces mechanical stresses that can in turn affect growth rates, have received little attention. Here, we study the noisy growth of elastic sheets subject to mechanical feedback. Considering both isotropic and anisotropic growth, we find that the density-density correlation function shows power law scaling. We also consider the dynamics of marked, neutral clones of cells. We find that the areas (but not the shapes) of two clones are always statistically independent, even when they are adjacent. For anisotropic growth, we show that clone size variance scales like the average area squared and that the mode amplitudes characterizing clone shape show a slow $1/n$ decay, where n is the mode index. This is in stark contrast to the isotropic case, where relative variations in clone size and shape vanish at long times. The high variability in clone statistics observed in anisotropic growth is due to the presence of two soft modes—growth modes that generate no stress. Our results lay the groundwork for more in-depth explorations of the properties of noisy tissue growth in specific biological contexts.

4.2 Introduction

Growth is central to biology and usually involves a level of stochasticity [39, 117, 118]. The presence of such noise can have significant consequences for developmental processes like morphogenesis and the regulation of organ size. Yet, relatively little is known about quantitative aspects of stochastic growth. Our goal here is to understand the interplay between noise and mechanical feedback in growing elastic tissues. To that end, we present a generic, continuum model of such tissues and use it to study measurable features of tissue architecture like density fluctuations and statistics of marked, neutral clones. Our model makes a number of unexpected predictions, including the presence of power law correlations in space and the existence of soft modes that allow clone sizes to grow diffusively, evading the effects of mechanical feedbacks that might otherwise be expected to limit clone size variability.

In experiments, noise in growth has most often been probed through the size and spatial distribution of clones of cells [4, 119–124], especially of neutral clones that are genetically identical to surrounding tissue except for a clone marker. Cell density variation has also been observed directly in culture [55, 56, 125–127] and in fixed tissues [128], as have correlations in positions of mitotic cells [117], and size asymmetry between contralateral organs can be used as an indirect readout of noise levels [86].

Theoretically, the most thoroughly explored area is the noisy dynamics of stem cell populations [119, 120, 123], where zero-dimensional descriptions are often appropriate and spatial crowding effects, when important, have been included at the level of simple lattice models. Similar models apply to fluid tissues where clone fragmentation and aggregation is the dominant process at long times [121]. Here, in contrast, our goal is to explicitly include the effects of mechanical stresses on growth of elastic tissues. An elastic description is typically valid for plants [57, 129] and can be applied to animal tissues like the *Drosophila* wing imaginal disc to the extent that cell rearrangements are rare [3, 58, 130–132]; moreover, the formalism we adopt can be extended to encompass simple models of plastic flow that allow for more frequent rearrangements [59]. We expect that noise will lead to growth nonuniformities and thus to the uneven accumulation of cell mass; this, in turn, will generate stresses that can feed back on local growth rates. Ranft *et al.* [6] have shown that such mechanical feedbacks cause the stress tensor to relax as if the tissue were a viscoelastic fluid; their treatment of noise, however, is limited to fluctuations about zero average growth, where most of the phenomena of interest here are absent.

On a very basic level, the idea of mechanical feedback on growth is uncontroversial—cells obviously cannot grow indefinitely into space occupied by other cells, so some sort of contact inhibition or crowding effects must be present. Whether cells more generally adjust

their growth rates to their mechanical environment is, however, less obvious. The idea that negative feedback from mechanical stresses could damp out cell density fluctuations was proposed in [51] and has since been incorporated into a number of models [53, 57, 109, 122, 129, 133–140]. Clear experimental examples of mechanical feedback have been more difficult to obtain [141, 142]. Nonetheless, several studies have argued that tissues both in culture [126, 143–145] and *in vivo* [52, 146–149] respond to mechanical stress by modulating the rate and orientation of cell division or by inducing cell death [145, 150–152]. Clones of fast-growing cells in *Drosophila* wing discs reduce their growth rate through mechanical feedback [122], and similar behavior has been observed in plant systems [129, 153] including the *Arabidopsis* sepal [124]. In confluent monolayers, contact inhibition slows mitosis [125, 127]. Cell aggregates [154–157] and bacterial populations [158] also appear to respond to mechanical cues. Thus, it seems likely that some mechanical feedback on growth is present in many tissues.

In what follows, we first introduce our basic framework, which assumes linear elastic deformations about a uniformly growing reference state and linear feedback of the stress tensor on the local growth rate. We then consider the special case of strictly isotropic growth, where we show that density-density correlations generically decay with distance as a power law and that mechanical feedback drives clone size variability to zero on large scales. (Closely related results are obtained independently in [159].) We also find that the areas of neighboring clones are statistically uncorrelated. We then turn to the more general case of locally anisotropic growth. Here, we observe the appearance of soft modes, where faster growth of one tissue region is exactly compensated by slower growth in surrounding regions and elastic deformations so as to leave the tissue completely stress-free; these modes can thus grow without bound even in the presence of feedback. As a consequence, clone sizes display a standard deviation of order their mean, in strong contrast to the isotropic case.

4.3 Basic Model

We consider a flat epithelium undergoing isotropic, exponential growth on average, with small, random deviations from this average. Though many of our results can be generalized, we limit ourselves here to two-dimensional tissues. At the macroscopic scale, we view the epithelium as an elastic continuum. Growth then looks like local creation of mass, and non-uniform growth can induce tissue deformations. We treat the simplest case of an infinite tissue and ignore boundary effects.

With these assumptions, we define reference (Lagrangian) coordinates $\{\mathbf{R}\}$ and material (Eulerian) coordinates $\{\mathbf{r}\}$. Each point on the tissue at time t is related to a point in the

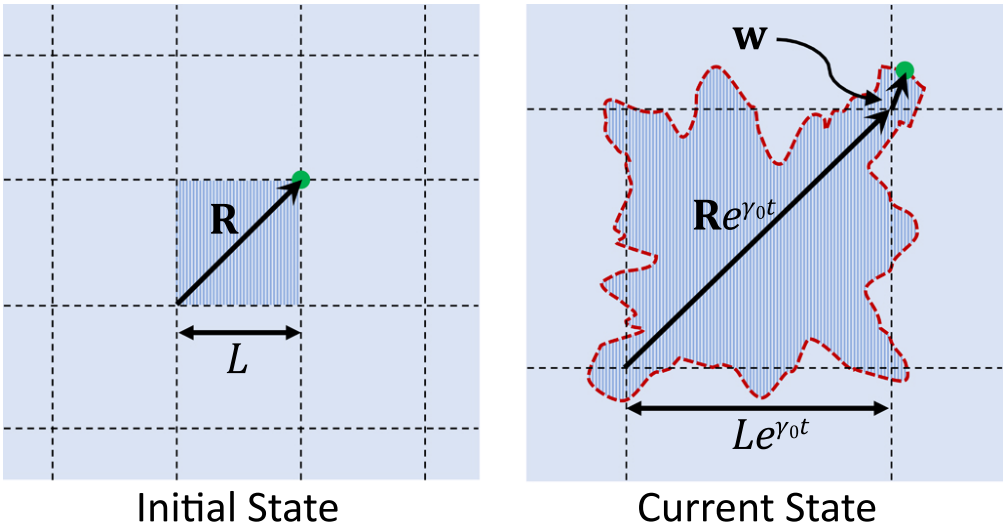

Figure 4.1: Noisy growth leads to tissue deformation. A shaded square of side L in the initial state has grown at time t into a larger region with deformed boundaries (red); dashed grid lines indicate the average, uniform tissue dilation. A material point (green dot) initially at $\mathbf{R}$ is displaced to $\mathbf{R}e^{\gamma_0 t} + \mathbf{w}$.

reference coordinates by $\mathbf{r} = \mathrm{e}^{\gamma_0 t}\mathbf{R} + \mathbf{w}$, where γ_0 is the average growth rate and $\mathbf{w}$ the local deformation due to growth fluctuations (Fig. 4.1). We focus primarily on $\gamma_0 > 0$ but show in the Supporting Information (Appendix B) that we recover known results [6] when $\gamma_0 = 0$.

Growth is represented by the symmetric second rank tensor $\mathrm{G}(\mathbf{R})$ (see, e.g., [59]). Its principal components give the tissue's preferred dilation—that is, the factor by which the tissue particle at $\mathbf{R}$ must expand to remain stress free—along the two principal axes. It can be decomposed as $\mathrm{G}(\mathbf{R}) = \bar{G}\mathbb{1} + \widetilde{\mathrm{G}}(\mathbf{R})$, where the scalar $\bar{G} = \mathrm{e}^{\gamma_0 t}$ describes the spatially uniform, average tissue expansion, and the tensor $\widetilde{\mathrm{G}}(\mathbf{R})$ represents fluctuations about the average.

We assume that growth is slow enough that the tissue is always at mechanical equilibrium; absent any external forces or confinement, spatially uniform growth then should not generate any mechanical stress, which will instead be caused entirely by the spatially-varying component $\widetilde{\mathrm{G}}$ of the growth tensor. In the limit of weak fluctuations in growth rate, $\widetilde{\mathrm{G}}$ and $\mathbf{w}$ will both be small, and we can linearize at each instant about the uniformly dilated state. The resulting theory has a form familiar from thermoelasticity [160,161]. We define a strain-like tensor $w_{ij} = (\partial_i w_j + \partial_j w_i)/2$, where ∂_i denotes the partial derivative with respect to R_i. (Throughout this paper, spatial derivatives are taken with respect to Lagrangian coordinates unless otherwise specified.) The Cauchy stress tensor is then:

$$\sigma_{ij} = \frac{1}{\bar{G}}[\lambda(w_{ll} - \widetilde{G}_{ll})\delta_{ij} + 2\mu(w_{ij} - \widetilde{G}_{ij})], \tag{4.1}$$

where λ and μ are the Lamé coefficients and summation on repeated indices is implied. Intuitively, Eq. 4.1 says that the stress vanishes when the actual strain w_{ij} matches the preferred local deformation due to growth $\widetilde{G}_{ij}$ and otherwise grows linearly with the difference between these two quantities. It differs from textbook thermoelastic results only in the factor of $1/\bar{G}$, which arises from the conversion of derivatives with respect to $\mathbf{R}$ to derivatives with respect to the uniformly dilated reference coordinates $\bar{G}\mathbf{R}$. Eq. 4.1 can also be obtained by linearizing a fully nonlinear theory of morphoelasticity [59] (see Appendix B).

Given Eq. 4.1, force balance $\partial_i \sigma_{ij} = 0$ implies

$$(\lambda + 2\mu)\nabla(\nabla.\mathbf{w}) - \mu(\nabla \times \nabla \times \mathbf{w}) = \lambda \nabla \widetilde{G}_{ll} + 2\mu \nabla.\widetilde{\mathrm{G}}. \tag{4.2}$$

This equation may be solved to obtain $\mathbf{w}$, and thus w_{ij} and σ_{ij}, at each instant as a function of $\widetilde{\mathrm{G}}$.

To complete our description, we must specify the dynamics of G, whose most general possible form is

$$\partial_t \mathrm{G} = \Gamma \mathrm{G}, \tag{4.3}$$

where Γ is a rank four tensor that incorporates mechanical feedback and noise (see Appendix B). We define ∂_t to be a time derivative taken at fixed Lagrangian coordinates $\mathbf{R}$. (The Appendix B discusses how $\partial_t \mathrm{G}$ with this convention is related to proposed expressions for the time derivative at fixed Eulerian coordinates.)

Assuming that deviations from uniform growth are small, we can expand Eq. 4.3 to linear order in stress feedbacks and noise. The most general form allowed by symmetry is

$$\partial_t \left[\frac{\widetilde{G}_{ij}}{\bar{G}} \right] = c\ \sigma_{ll}\ \frac{\delta_{ij}}{2} + c^{(d)} \left(\sigma_{ij} - \sigma_{ll}\ \frac{\delta_{ij}}{2} \right) + \xi_{ij}(\mathbf{R}, t), \tag{4.4}$$

where we have also dropped higher order gradient terms (whose effects are addressed in the SI). The constants c and $c^{(d)}$ give the strengths of the stress feedbacks (the superscript (d) stands for deviatoric), and ξ_{ij} is a noise term.

4.3.1 Density

Within continuum elasticity, it is natural to define a density $\rho(\mathbf{R}, t)$ of the deformed material. For a complex biological tissue, ρ of course does not represent the total mass density but instead can be thought of as roughly the density of materials (like cytoskeletal proteins) that give the tissue an elastic rigidity or, equivalently, as a measure of elastic tissue compression or expansion relative to an ideal, unstressed state. If we call the (uniform) density in the

stress-free configuration ρ_0 and deviations $\delta\rho(\mathbf{R},t) = \rho(\mathbf{R},t) - \rho_0$, then to linear order in growth fluctuations,

$$\delta\rho = \frac{\rho_0}{\bar{G}}(\widetilde{G}_{ll} - w_{ll}). \tag{4.5}$$

If all cells in the tissue have the same preferred apical area, then ρ is proportional to the cell density. Even if that is not the case, as long as cells' relaxed areas are uncorrelated, the difference between the cell density and the average of ρ over a region of area A will decrease as $1/\sqrt{A}$, allowing the cell density to be used to estimate ρ on long enough scales.

4.4 Isotropic Growth

In order to build intuition, we first consider the simplest case of isotropic growth. We thus set $\widetilde{G}_{ij} = \widetilde{G}\,\delta_{ij}$ and keep only the isotropic part of Eq. 4.4 by taking $c^{(d)} = 0$ and $\xi_{ij} = \xi\delta_{ij}/2$.

As outlined above, we can use force balance (Eq. 4.2) to find w_{ij} in terms of $\widetilde{G}$. After Fourier transforming, we have $(\lambda+2\mu)(\mathbf{Q}.\mathbf{w})\mathbf{Q} - \mu(\mathbf{Q}\times\mathbf{Q}\times\mathbf{w}) = -2i(\lambda+\mu)\widetilde{G}\,\mathbf{Q}$. Solving for $\mathbf{w}$ and using Eq. 4.5 to relate $\delta\rho$ and $\widetilde{G}$, we find

$$\mathbf{w} = -2i\frac{(\lambda+\mu)\ \mathbf{Q}}{(\lambda+2\mu)Q^2}\widetilde{G} \quad \text{and} \quad \delta\rho = \rho_0\frac{2\mu}{\lambda+2\mu}\ \frac{\widetilde{G}}{\bar{G}}.$$

Then Eq. 4.4 can be rewritten as

$$\partial_t\,\delta\rho(\mathbf{R},t) = -k\,\delta\rho + \rho_0\ \frac{\mu}{\lambda+2\mu}\xi(\mathbf{R},t). \tag{4.6}$$

Here, $k = 2\mu(\lambda+\mu)c/(\lambda+2\mu)$, and the (scalar) noise $\xi(\mathbf{R},t)$ is delta correlated in time and spatially correlated on a length scale a of order a cell radius; this small but non-zero correlation length is needed to prevent pathological behavior and reflects the fact that cell growth and division are correlated on the scale of a single cell. Because typical cell sizes remain constant as the tissue grows, the correlation length should be viewed as fixed in Eulerian coordinates, so that $\langle\xi(\mathbf{r},t)\xi(\mathbf{r}',t')\rangle = De^{-\frac{(\mathbf{r}-\mathbf{r}')^2}{a^2}}\delta(t-t')/\pi a^2$, where D is the noise strength. In Lagrangian coordinates, the noise then satisfies $\langle\xi(\mathbf{R},t)\xi(\mathbf{R}',t')\rangle = De^{-\frac{\bar{G}(t)^2(\mathbf{R}-\mathbf{R}')^2}{a^2}}\delta(t-t')/\pi a^2$, where we used, to leading order, $\mathbf{r}\approx\bar{G}\mathbf{R}$.

4.4.1 Density-density Correlations

From Eq. 4.6 we can calculate the density-density correlation function, which we find in steady state drops off like a power law in r for large separations $r \gg a$:

$$\frac{1}{\rho_0^2} \langle \delta\rho(\mathbf{r}, t)\delta\rho(\mathbf{0}, t)\rangle_{t\to\infty} \sim \left(\frac{r}{a}\right)^{\frac{-2k}{\gamma_0}}, \tag{4.7}$$

where the pre-factor is $\mathcal{O}(k/\gamma_0)$ (see Appendix B). Fig. S1 plots the full correlation function versus r/a.

To understand this behavior, suppose that noise generates a density fluctuation initially correlated on a length scale a. Over time, growth will advect this fluctuation outwards while mechanical feedback will cause its amplitude to decay. After time t, the initial, small-scale fluctuation will induce correlations up to a scale $r \sim a\ e^{\gamma_0 t}$, but $\delta\rho$ will have decayed like e^{-kt} (so that the correlation function is smaller by a factor e^{-2kt}). For a given r, fluctuations that happened around $t^*(r) = \log(r/a)^{1/\gamma_0}$ ago are dominant; earlier fluctuations have died out while later ones have not yet reached the distance r. Thus, we expect $\langle\delta\rho(\mathbf{r})\delta\rho(\mathbf{0})\rangle \sim \exp[-2kt^*(r)] \sim (r/a)^{-2k/\gamma_0}$. A similar mechanism produces power law correlations in inflationary models of the early universe [76]. This result requires a small but finite initial correlation length for fluctuations. In the SI, we extend our results to the case where this lengthscale is set by gradient terms in the growth dynamics as well as to unequal time correlations in arbitrary dimension.

Qualitatively, our finding of power law correlations says that cells in growing epithelia are more clumped together on large scales than for a totally random spatial distribution, with the effect becoming more pronounced for smaller k/γ_0. Correlations in cell density are experimentally accessible [55, 56, 127, 128], and we expect that similar clumping should be observed in spatial distributions of mitotic cells (which, intriguingly, are known cluster in some tissues [3, 117]). Estimates of the exponent $2k/\gamma_0$ could be used to determine the strength c of mechanical feedback, which has not previously been measured.

4.4.2 Clone Statistics

Following marked, neutral clones has proven to be a useful tool to track growth and development [4, 119–124]. Here, we examine the size and shape statistics of clones in a growing tissue. Starting from a circular clone, we derive expressions for the variance of the clone area and of mode amplitudes characterizing the clone shape.

The area of a clone with initial radius R_c is $A(t) = \int_{R\le R_c} |\partial\mathbf{r}/\partial\mathbf{R}|\, \mathrm{d}\mathbf{R} \approx \pi(\bar{G}R_c)^2 +$

$\bar{G}\ \int_{R\leq R_c} \nabla.\mathbf{w}\ \mathrm{d}\mathbf{R}$, to leading order in small w. The variance of clone size is then

$$\mathrm{Var}(A) = \bar{G}^2 \int_{R,R'\leq R_c} \langle \nabla.\mathbf{w}\ \nabla'.\mathbf{w}' \rangle\ \mathrm{d}\mathbf{R}\mathrm{d}\mathbf{R}', \tag{4.8}$$

where $\nabla' = \nabla_{\mathbf{R}'}$ is the gradient operator taken with respect to $\mathbf{R}'$. To study clone shape, we describe the instantaneous clone boundary as a curve $r_c(\theta)$ in Eulerian coordinates, where θ is the polar angle, which we can then express as a Fourier series $r_c(\theta) = \sum B_n e^{in\theta}$. To linear order in $\mathbf{w}$, we may neglect differences between the Lagrangian and Eulerian polar angles Θ and θ, and $r_c = \bar{G}R_c + \hat{\mathbf{R}}.\mathbf{w}$, where $\hat{\mathbf{R}}$ is a unit vector in the direction of $\mathbf{R}$. Continuing to work to the same order, and defining $w_j' = w_j(R_c, \Theta')$, it is easy to see that

$$\left\langle |B_n|^2 \right\rangle = \int_0^{2\pi} \frac{\mathrm{d}\Theta \mathrm{d}\Theta'}{(2\pi)^2} \hat{R}_k(\Theta)\hat{R}_j(\Theta')\langle w_k w_j' \rangle e^{-in(\Theta-\Theta')}. \tag{4.9}$$

For isotropic growth, both $\mathbf{w}$ and $\nabla.\mathbf{w}$ can be written in terms of $\delta\rho$, so Eq. 4.6 is all we need to evaluate Eqs. 4.8 and 4.9. We find that the variances in clone size and shape become small compared to the mean at long times: $\lim_{t\to\infty} \mathrm{Var}(A)/\left\langle A \right\rangle^2 \to 0$ and $\lim_{t\to\infty} \left\langle |B_n|^2 \right\rangle / B_0^2 \to 0$. Thus, for isotropic growth, all sufficiently old clones are statistically similar. This is a direct consequence of the mechanical feedback that causes $\delta\rho$ to relax exponentially to zero; we will see in the next section that once growth is allowed to be locally anisotropic, soft modes lead to dramatically different behavior.

Before introducing anisotropy, we note that our model also predicts that the areas of two nearby clones are uncorrelated: If the deviations from the mean clone areas are ΔA_1 and ΔA_2, then $\langle \Delta A_1 \Delta A_2 \rangle = 0$. This follows immediately from the elastic response of an infinite tissue to localized growth [122]: With $\widetilde{G} \sim \delta(\mathbf{R})$, $\mathbf{w} \sim \hat{\mathbf{R}}/R$, and $\nabla.\mathbf{w} = 0$ except at the origin. Thus, while the shapes of clones near the origin are distorted, only clones that actually contain the origin change their area (Fig. 4.2A). More generally, for both isotropic and anisotropic growth, the size of each clone depends only on $\widetilde{G}$ within its own boundaries, and $\widetilde{G}$ is spatially uncorrelated (see Appendix B).

4.5 Anisotropic Growth

Cells in both animal [52, 144, 146] and plant [153] tissues have been shown to orient their divisions relative to the principal axis of an applied stress. Thus, in general, we should consider stress-dependent, local growth anisotropies. If we continue to assume that growth is isotropic on average so that $G_{ij} = e^{\gamma_0 t}\delta_{ij} + \widetilde{G}_{ij}$, then we can specify the symmetric tensor

$\widetilde{\mathrm{G}}$ by three scalars: its trace and two components for the traceless part. We follow the same steps as in the isotropic case to solve Eq. 4.4 and find expressions for density-density correlations and clone statistics. We will see that density-density correlations follow the same power law behavior as in Eq. 4.7, but that new soft modes appear which cause clone size and shape variability to remain large even at long times.

To solve Eq. 4.2 for $\mathbf{w}$ in terms of $\widetilde{\mathrm{G}}$, we work in Fourier space and write the traceless part of $\widetilde{\mathrm{G}}$ in terms of the Q-dependent scalars $\widetilde{G}_{\parallel}$ and $\widetilde{G}_{\perp}$ (see also the SI):

$$\widetilde{G}_{ij} = \widetilde{G}_{ll}\frac{\delta_{ij}}{2} + (\widetilde{G}_{\parallel}\delta_{ik} - \widetilde{G}_{\perp}\epsilon_{ik})\left[\frac{2Q_kQ_j}{Q^2} - \delta_{kj}\right], \tag{4.10}$$

where ϵ_{ij} is the Levi-Civita tensor. Eq. 4.2 then gives the components of $\mathbf{w}$ longitudinal and transverse to $\mathbf{Q}$:

$$\begin{aligned} w_k^{\parallel} &= \frac{-i}{\lambda+2\mu}\left[(\lambda+\mu)\widetilde{G}_{ll} + 2\mu\ \widetilde{G}_{\parallel}\right]\frac{Q_k}{Q^2} \\ w_k^{\perp} &= 2i\ \widetilde{G}_{\perp}\ \epsilon_{kl}\frac{Q_l}{Q^2}. \end{aligned} \tag{4.11}$$

Finally, we have the stress tensor:

$$\sigma_{ij} = 2(\lambda+\mu)\frac{\delta\rho}{\rho_0}\left[\frac{Q_iQ_j}{Q^2} - \delta_{ij}\right]. \tag{4.12}$$

Strikingly, growth in an infinite system can thus only induce a nonzero stress when there is a non-vanishing density fluctuation $\delta\rho$ related to $\widetilde{G}_{ij}$ by

$$\delta\rho = \rho_0\frac{\mu}{\lambda+2\mu}\left(\frac{\widetilde{G}_{ll} - 2\widetilde{G}_{\parallel}}{\bar{G}}\right). \tag{4.13}$$

Having found the stress, we next turn to the time evolution of G. The noise ξ_{ij} in Eq. 4.4 now has three independent components. We define ξ_{ll}, $\xi_{\parallel}$, and $\xi_{\perp}$ in analogy to the corresponding quantities in Eq. 4.10 and take them to be independent, Gaussian random variables; rotational invariance requires that $\xi_{\parallel}$ and $\xi_{\perp}$ have the same strength which can, however, differ from that of ξ_{ll}. As in the isotropic case, we choose these random variables to be delta correlated in time but colored in space to avoid pathological behavior (see Appendix B).

Substituting Eq. 4.12 for the stress into the growth dynamics Eq. 4.4, we find that the

dynamics can be decomposed into three independent modes as (see also SI)

$$\partial_t \delta\rho = -(k + k^{(d)})\delta\rho + \rho_0 \frac{\mu}{\lambda + 2\mu} \left(\xi_{ll} - 2\xi_{\parallel}\right) \tag{4.14}$$

$$\partial_t Z_T = \xi_{\perp} \tag{4.15}$$

$$\partial_t Z_L = \xi_{ll} + 2\frac{k}{k^{(d)}}\xi_{\parallel}, \tag{4.16}$$

where $k^{(d)}$ is defined similarly to k, and $Z_T = \widetilde{G}_{\perp}/\bar{G}$ and $Z_L = [\widetilde{G}_{ll} + 2(k/k^{(d)})\ \widetilde{G}_{\parallel}]/\bar{G}$ are the amplitudes respectively of transverse and longitudinal soft modes, which do not produce any stress and thus grow diffusively. Before studying the density and clone statistics, we next consider these soft modes more carefully.

4.5.1 Soft Modes

As just shown, in two dimensions growth has two soft modes. They have the same physical origin: A nonuniform growth field $\widetilde{\mathrm{G}}$ induces a displacement $\mathbf{w}$ that exactly cancels the growth, so that no mechanical stress or density change results. Fig. 4.2B illustrates this for the longitudinal mode. In essence, excess mass created by faster growth in one part of the tissue is transported to slower-growing parts so as to equalize the tissue density. What is remarkable is that, for certain patterns of growth, this redistribution can be accomplished in an elastic tissue—thus without viscous flow or cell neighbor exchanges—without causing shear stresses or mechanical feedback. Specifically, Eq. 4.13 implies that only growth perpendicular to $\mathbf{Q}$—i.e., only the $\widetilde{G}_{22}$ component of $\widetilde{\mathrm{G}}$, if $\mathbf{Q}$ points in the 1 direction—induces density changes that can then generate stresses (Eq. 4.12). In contrast, growth parallel to $\mathbf{Q}$ (Z_L) or at a 45° angle (Z_T) is exactly compensated by elastic deformations.

From Eqs. 4.15–4.16, one might imagine that the soft modes grow without bound. This, however, turns out not to be the case: The modes are defined at fixed Lagrangian wavevector $\mathbf{Q}$, but $\xi_{\perp}$ and $\xi_{\parallel}$ have constant correlations in Eulerian space. As growth progresses, a given $\mathbf{Q}$ corresponds to longer and longer Eulerian lengthscales, leading to a decrease in the noise amplitude with time. As a result (see Appendix B), the mean squared values of Z_L and Z_T remain bounded for all times.

4.5.2 Density-density Correlations

As in the isotropic case, we can calculate density-density correlation functions for anisotropic growth. From Eq. 4.14, it is evident that the only differences between the two cases are the feedback strength and the presence of a second noise term $\xi_{\parallel}$. The latter will only affect the

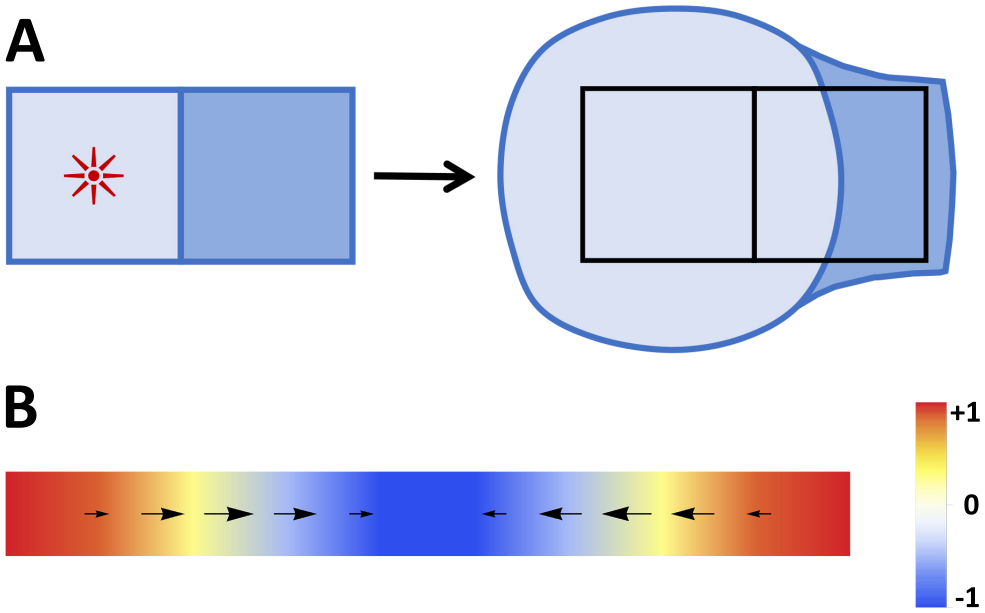

Figure 4.2: (A) Independence of nearby clone areas. A localized region of growth (marked by the red star) at the center of the left clone (light blue) leads to an increase in the area of that clone, but it leaves the area of the adjacent clone (dark blue) unchanged even while distorting its shape. (B) Longitudinal soft mode. Sinusoidal growth (color scale gives $\widetilde{G}$) leads to a deformation field $\mathbf{w}$ (arrows) that exactly compensates for the growth, leaving the density unchanged.

pre-factors. We thus find that

$$\frac{1}{\rho_0^2}\left\langle \delta\rho(\mathbf{r},t)\delta\rho(\mathbf{0},t)\right\rangle_{t\to\infty} \sim \left(\frac{r}{a}\right)^{\frac{-2(k+k^{(d)})}{\gamma_0}}, \tag{4.17}$$

just as for isotropic growth, with prefactors of the same order.

4.5.3 Clone Statistics

In the isotropic case, where $\delta\rho$ was the only dynamical variable, mechanical feedback caused clone size and shape variations to decay in time relative to the average dilation. However, if we allow growth anisotropies, $\nabla.\mathbf{w}$ and $\mathbf{w}$, which are the relevant variables for clone properties (Eqs. 4.8 and 4.9), depend on the soft modes as well as on the density.

As mentioned above, the correlation functions for soft modes reach constant values at long times, whereas correlators that involve $\delta\rho$ decay exponentially in time. Thus $\langle\nabla.\mathbf{w}\ \nabla'.\mathbf{w}'\rangle$ and $\langle w_k w_j'\rangle$ will be dominated by soft modes at long times. We find that as $t\to\infty$ the clone area obeys

$$\frac{\mathrm{Var}(A)}{\langle A\rangle^2} \sim \frac{1}{R_c^2}, \tag{4.18}$$

while for $n \geq 2$ the mode amplitudes show a slow $1/n$ decay:

$$\frac{\langle |B_n|^2\rangle}{B_0^2} \sim \frac{1}{R_c^2}\frac{n}{n^2-1}. \tag{4.19}$$

The pre-factors are $\mathcal{O}(1)$ if $R_c \sim a$, i.e. the clone is initially the size of a single cell. Adjacent clones' areas are uncorrelated, just as in the isotropic case (Fig. 4.2A).

Eq. 4.18 says that the areas of large clones are just as variable as those of small clones. Such behavior would be normal for an exponentially growing population with no constraints on its size [162], but it is quite unexpected for a clone embedded in an elastic tissue and subject to mechanical feedback. In effect, soft modes allow the growth to be as noisy as if feedback were absent. Together with our finding that the areas of different clones are uncorrelated, this result means that even elastically coupled clones behave in many ways as if they were growing independently and without feedback.

4.6 Discussion

We presented a simple model of noisy growth of elastic tissues with mechanical feedback. This model predicts nontrivial behavior for experimentally accessible quantities including

density-density correlation functions and clone size statistics.

We first showed that density correlations decay in space as a power law whose exponent depends on the average growth rate and feedback coefficient. Using our result, it should be possible to estimate the strength $c + c^{(d)}$ of the mechanical feedback, a quantity that has not so far been measured in growing tissues. Somewhat counterintuitively, the sign of $c^{(d)}$ seems to be negative in some plant systems [153]. We find that this does not destabilize growth as long as $c + c^{(d)} > 0$.

We then studied marked, neutral clones, whose statistics depend strongly on whether local growth anisotropies are allowed. In their absence, mechanical feedback tends to prevent fluctuations on large scales, and size variation becomes much smaller than the mean for large clones. This behavior changes dramatically for anisotropic growth, where soft modes allow certain deformations to escape any negative feedback. As a consequence, the standard deviation in clone area grows like the mean, exactly as if the clone were an exponentially growing aggregate of independently dividing cells completely indifferent to the presence of surrounding tissue [162]. Similarly, fluctuations in clone shape remain large when growth is anisotropic and soft modes dominate. Strikingly, we also find that the areas of different clones are always uncorrelated. These conclusions together imply that (at least to within the weak noise approximation inherent in our calculations) neutral clone areas have the same statistical properties in elastic tissues as in systems where mechanical feedback and crowding effects are completely absent.

Our calculations also show more generally that overgrowth of one clone (whether or not neutral) cannot induce undergrowth in nearby tissue solely through mechanical feedback in a linear, elastic continuum (Appendix B and [122]); this is consistent with the fact that known examples of such behavior, like cell competition [163], appear to depend on the activation of specific signaling pathways rather than on generic mechanical effects.

One limitation of our results is that they ignore clone disappearance and fragmentation. Such events should be vanishingly unlikely for fast enough growth or large enough initial clone area, but can skew size distributions in the opposite limits [119]. Thus, our findings are most directly applicable to tissues where the rate of cell division is much higher than of cell death or to situations where clones can be imaged over time [4], so that it is possible to quantify a clone's incremental growth after it has reached some threshold size.

We emphasize that the soft modes in our model are distinct from stress relaxation due to tissue fluidization [6]. Whereas in the latter case, stress decays exponentially in time, for soft modes it is identically zero. Our soft modes are related to harmonic growth [53, 164, 165], which likewise does not generate any stress. This phenomenon, however, occurs in finite tissues with isotropic growth and appropriate boundary conditions. Here, anisotropic soft

modes are integral to the structure of the growth problem even in the absence of boundary effects.

Our model is the simplest that incorporates noise in the growth control problem. It ignores the influences both of boundaries and of frictional forces. Friction always dominates for large enough growing tissues [166], but its effects can be small when growth is slow or sources of drag are weak (as, e.g., for plant tissues growing in air). By assuming a solid tissue, we also neglect the possibility of cell rearrangements (T1 transitions) and flow. This assumption usually holds for plant cells [57, 129]. In animal epithelia, flows and T1's are sometimes significant [121], but there are also cases that exhibit more solid-like behavior. The *Drosophila* wing disc, for example, clearly supports circumferential stresses without yielding [52,146], and cell shapes and packing are consistent with a solid rather than a fluid-like phase [167]. Despite some differences in measured rates of T1's in *ex vivo* discs [3, 58] and of clone dispersal [130–132], these are consistent with predominantly solid behavior with possibly some plastic slippage. Thus, it is reasonable to treat the disc as an elastic solid in a first approximation. Moreover, plastic deformations can be described with the same multiplicative decomposition of the deformation gradient used in morphoelasticity (Appendix B), so that incorporating a simple version of plasticity into our model requires nothing more than renormalizing the coefficients in the time evolution of G (Eq. 4.4) [59].

Our calculations also assume weak noise and hence small deformations. Importantly, this approximation is valid and self-consistent even with soft modes, because the soft mode amplitude is proportional to the noise strength and remains bounded at long times. Nonetheless, it would be of interest to explore what happens for stronger noise and larger deformations. Indeed, the physics of nonequilibrium growth has a long and rich history (e.g. [69]), and from this perspective volumetric tissue growth represents an entirely new class of problems. Notably, we expect that the basic physics of soft modes survives the transition to the nonlinear regime. In the nonlinear case, it is convenient to characterize growth by a "target metric" (equal to $\mathrm{G}^T\mathrm{G}$); if this metric lacks intrinsic curvature, it can always be compensated by a displacement field $\mathbf{w}$ and so will not generate any stresses [54, 59].

The formalism presented here can also be extended to include less generic effects, like inhomogeneous growth driven by morphogen gradients and chemical signaling, that are nonetheless crucial to many examples of morphogenesis and organ size control [109,133,134]. Our work is thus a first step towards more comprehensive models of specific biological systems.

CHAPTER 5
Conclusions

In this thesis, we tackled profound questions in growth and size coordination in developmental biology with simple and generic models, combining methods from a variety of subjects such as nonequilibrium statistical physics, theory of elasticity and control theory. Our approach enabled us to make nontrivial predictions about the underlying biological processes that are at play in a growing living being. Importantly, these predictions were made without relying too heavily on the microscopic details of such systems. This is indeed a feature of phenomenology that makes these models powerful tools in studying complex biological systems. Our models not only shed light on the biology involved in the process of growth, but also informed us of exciting new physics waiting to be explored. Here, we give a brief summary of this work and discuss some possible future steps in studying nonequilibrium tissue growth.

We started with a fundamental question in biology: How do growing animals ensure that their organs have the proper sizes in relation to one another and to the body? What makes this question a problem well-suited for physicists is that there is no information in the DNA that directly specifies organ shape and size. Thus, morphogenesis is a self-organization problem likely influenced by many different physical and chemical interactions, which calls for the type of coarse-grained modeling for which physicists were trained.

Chapter 2 entailed our attempts at answering the aforementioned question. More specifically, inspired by the biological observation that Dilp8, an endocrine signal secreted by the organs during *Drosophila* larval stage, is involved in coordination of organ sizes, we asked the question, can we get organ size coordination via a single chemical signal? To answer this question, we studied several biologically plausible models based on feedback mechanisms regulating either absolute size or growth rate of organs. By building biologically relevant feedback models we were able to study the implications of each feedback mechanism if a system were to employ said mechanism for organ size coordination. In particular, by fixed point analysis of different models and studying noisy organ growth, we were able to discriminate between different coordination mechanisms and explore experimental implications of

each feedback model. Crucially, these generic models equipped us with the predictive power to set limits on the ability of chemical signaling in coordination of final organ sizes.

Notably, we made an important assumption that organs have an idea of what size they want to be, which we called the target size. This assumption, again based on biological data, had important consequences for the feedback models. For example, if organs did not have a target size, proportional feedback on growth rate (Section 2.12) would have the opposite sign than what we found in our study, implying very different experimental signatures. Moreover, having a target size introduces a source of error that needs to be corrected for proper organ proportions to be achieved (because it is possible for organs to estimate their target sizes inaccurately on their own). Notably, we found that no form of feedback can reliably correct errors in target size. This is an important conclusion as it implies that organs must have an intrinsic size correction mechanism to buffer noise in their target size. In other words, organs autonomously set the correct target size and feedback can then help coordinate sizes during growth, perhaps in response to environmental fluctuations and to help speed up development.

Perhaps the most obvious signature of feedback is coordination during growth. Then, it would be interesting to look at *in vivo* imaging of wing discs in wild type and *dilp8* –/– flies and measure the wing sizes as the larva grows. The expectation would be that if Dilp8 acts as a feedback agent during normal growth, we expect to see less variability in wing pairs in wild type flies during growth. Ideally, we would be able to extract FA curves and even extract the strength of feedback λ. Of course, there are challenges associated with live imaging as we need to minimize stresses to larvae or stress dependent pathways involving Dilp8 may be activated [21, 47, 48]. The Leopold Lab is pursuing this and hopefully in the near future, size variability during growth can be measured.

The conclusion that we reached in Chapter 2, namely that organs perhaps autonomously correct errors in target size, raises another important question: How exactly? We explored this question in Chapter 4, but before that, we discussed a collaboration with the Leopold Lab in Chapter 3. In addition to their instrumental contributions to our research by providing experimental data to use for testing our models, our collaborators provided us with the opportunity to take part in imaging and image analysis of adult wings. We used this opportunity to think about some open questions regarding FA in fruit fly wings in different genotypes. For example, what does the wing size FA distribution look like in wild type and *dilp8* –/– flies, or whether Dilp8 also affects shape asymmetry in wings? We outlined two algorithms, one for automating wing image segmentation that would help facilitate area measurements and thus size FA measurements, and another algorithm for quantifying the shape asymmetry based on the pattern of vein crossings in wings.

Regarding shape FA, there are indeed other ways of quantifying shape. For instance, one

could think about FA in the length to width ratio of the wing. One could also study the curvature of wing periphery and perhaps compare not only the shapes of left and right wings of the same fly, but how different wing shape is on average between different genotypes. It would be interesting to use different methods of shape FA measurements and see whether there is a particular measure that shows a significantly higher FA and what that would tell us about the process of wing growth.

In Chapter 4, we tackled the question of autonomous error regulation in growing tissues. It has been known that morphogen gradients can stop tissue growth without outside help [109]. Moreover, recently the form of mechanical response to morphogens that would lead to a unique target size has been studied [54]. However, it is not yet clear what the consequences of noise are in setting the precision of this final size. In fact, as we have discussed, there have not been many studies on noisy tissue growth in general. What we set out to understand, then, was the basic consequences of noise in quantities that could be observed experimentally. Our study not only was an important step towards understanding how organs may be able to accurately set their target size, but also provided us with striking results like the power law behavior of density density correlations, which could be used as an indirect way to measure the strength of mechanical feedbacks, a quantity that has not been measured before. Another somewhat unexpected observation was the appearance of two soft modes of growth, with important consequences for clone dynamics.

Remarkably, our simple framework, stripped of many biologically relevant details such as the existence of morphogen gradients, tissue boundaries and anisotropic growth, led to nontrivial and surprising results. Importantly, because of the generic nature of our model, our findings are expected to hold in more complex situations. For instance, to observe remnants of a power law, all that is needed is the existence of fluctuations correlated on a small length scale in a growing tissue, which would be present in most situations involving stochastic cell divisions. Of course, biological experiments are often not clean and it is not guaranteed that these power law behaviors can ever be observed experimentally, but our hope is that on large enough distances where short scale fluctuations average out, we might be able see the clumpiness of tissue due to the power law correlations.

In the mean time, vertex model simulations of growing tissues could provide an alternative avenue for observing the power law correlations and soft modes. It would be interesting to confirm these results starting from discrete cells. Simulations would also allow us to study cell rearrangements that currently are not included in our continuum framework and see how plasticity affects the results. Another open question is how valid our approximation to take the tissue as a continuum sheet is. For example, how large should the tissue be for this approximation to be meaningful? Are there important properties that are inherent to

tissues that are made up of discrete cells (other than cell rearrangements) that a continuous treatment cannot capture? Vertex model simulations provide the perfect platform to investigate these questions in future studies. On the theoretical side, future iterations of the model should improve the biological relevancy of the model by including for instance anistoropic average growth and spatially heterogeneous growth.

More generally, there are many open questions left regarding size coordination in biological tissues. A major question that remains to be answered is how the length scale of organ sizes is set. In Chapter 2 we started with the assumption that organs know this length scale, but how they know it is still an open question. Morphogen gradients can provide a length scale; however, by which mechanism organs can infer length scale from morphogens is not clear yet [24]. Would studying robustness of different mechanisms against noise help distinguish between them?

We only focused on coordination between organs. However, there are important organ-body communications as well. A related concept in insect development is the apparent existence of a larval "critical weight," a size after which the larva fully commits to pupal transition [21, 25]. In *Drosophila* for example, this size is thought to be in the middle of the last larval instar and is linked to nutrition and a spike in ecdysone [168], and may be connected to disc growth as well [169]. It is interesting to see how critical weight affects disc growth and is perhaps affected by Dilp8. Again in *Drosophila*, ecdysone interestingly has the opposite effect on the growth of imaginal discs and larval tissue: it promotes growth of imaginal discs but inhibits growth of larval tissues. Thus by virtue of this common player, organs and the body can communicate. Can we somehow coordinate final sizes if we include organ-body communications? Another important parameter we ignored in our model of organ growth was how target size is affected by systemic signals and nutrition. How does nutrition dynamically affect not only the target size, but also growth rate of organs and the body, and global growth checkpoints (e.g. the critical weight in insects)?

It would have been naive to think that the question we posed in the beginning of this thesis could be answered in the span of a few years of PhD research. It would have been equally as naive to think that phenomenological modeling can ever provide complete answers to questions in biology. Details do matter after all. Rather, phenomenology can help us focus on those details that matter more and are universally shared among many organisms. And this is indeed what we aimed for in this work. our main goal in this thesis was to provide simple toy models of growth regulation and organ size coordination based upon basic assumptions about the fundamental biological principles that govern those processes and to elucidate consequences of our assumptions. We hope that our work serves as a guide for future theoretical and experimental studies as well as a step, as small as it may be,

towards unlocking the mysteries of life.

APPENDIX A
Further Discussion of Organ Size Coordination

A.1 Introduction

In this Appendix, we discuss in more detail some of the calculations that we skipped in Chapter 2. We start by introducing the noisy version of the dynamics and briefly going over the small noise approximation that we used for our results particularly in Section 2.4. Then we will discuss an alternative signal normalization for the FR-P model, where instead of taking V to be proportional to the sum of organ sizes, we assume it is a constant throughout growth. We will show that it is not qualitatively different than the version we studied in Chapter 2. Next we will further discuss the FR-I model and in particular how to derive Eq. 2.16 and why the feedback is positive. We will then briefly explore the possibility that the coordination signal controls noise in target size or the strength of the noise, ϵ. Finally, we will provide a way to distinguish between the FS-P and FR-P models based on the fact that one is a positive feedback mechanism and the other is negative.

A.2 Noisy Growth Rate and Small Noise Approximation

In this section, we introduce our noisy growth framework, which we use to study the noisy versions of NC model (Section 2.3.1), FS-P model (Section 2.3.3) and FR-I model (Section 2.3.5), and also for our study of Dilp8 in *Drosophila* in Section 2.4. We start with a general noisy growth model and use small noise approximation to analytically quantify FA.

Consider the general stochastic differential equation (SDE)

$$\dot{A}_i = \gamma_i(A_1, A_2) + \xi_i(t), \tag{A.1}$$

where $\gamma_i(A_1, A_2)$ is the growth rate of organ i, which includes any coupling between the organs by feedback, and $\xi_i(t)$ represents the noise. Growth is roughly a Poisson random process, and it easily follows that $\xi_i(t)$ is a Gaussian random process (i.e. white noise) with a strength proportional to $\sqrt{\gamma_i}$ [170]. In particular, the noise correlators are $\langle \xi_i(t)\xi_j(t')\rangle \propto \gamma_i\, \delta_{ij}\delta(t-t')$. If noise was due to fully random cell divisions each contributing the same area δA, the proportionality constant would be δA. However, in general there are many sources of noise and cells continuously grow. Therefore, at each time step, a variable area will be added to the total area A_i and noise strength is affected. To account for this variability, we introduce a dimensionless free parameter ϵ which we call noise strength, and write $\langle \xi_i(t)\xi_j(t')\rangle = \epsilon^2 \bar{A}_\infty \gamma_i\, \delta_{ij}\delta(t-t')$, where $\bar{A}_\infty$ is the mean target size, which is included merely to fix the dimensions.

To better emphasize the multiplicative structure of the noise, we write the SDE (also called the Langevin equation) as

$$\mathrm{d}A_i = \gamma_i(A_1, A_2)\,\mathrm{d}t + \epsilon\sqrt{\bar{A}_\infty \gamma_i(A_1, A_2)}\,\mathrm{d}W_i, \tag{A.2}$$

where $\mathrm{d}W_i$ is the Wiener process representing the temporally uncorrelated Gaussian white noise ($\mathrm{d}W_i^2 \sim \mathrm{d}t$).

A key feature of this model is that the noise in Eq. A.2 approaches zero as the growth rate goes to zero. In fact this is only true if there is no apoptosis as having apoptosis would introduce fluctuations around the fixed point. This feature allows two organs with the same target size A_∞ to reach similar final sizes even without any continuous feedback loop if they are given enough time to grow. Inclusion of feedback is then expected to facilitate the decrease in noise helping the animal to mature sooner as we explicitly showed in Chapter 2.

Now we are in a position to quantify the size asymmetry between left/right organs. We define the following FA index (FAi)

$$\mathrm{FAi} = \frac{\sigma\{A_1 - A_2\}}{\langle \bar{A}\rangle} = \frac{(\mathrm{Var}(A_1) + \mathrm{Var}(A_2) - 2[\langle A_1A_2\rangle - \langle A_1\rangle\langle A_2\rangle])^{\frac{1}{2}}}{\langle \bar{A}\rangle} \tag{A.3}$$

where $\sigma\{\cdots\}$ denotes the standard deviation, $\mathrm{Var}(\cdots)$ the variance, $\langle\cdots\rangle$ the ensemble average and $\langle \bar{A}\rangle = (\langle A_1\rangle + \langle A_2\rangle)/2$ is the average organ size. For two organs growing independently (no feedback), $\langle A_1A_2\rangle = \langle A_1\rangle\langle A_2\rangle$. A lower FAi means that organs are more symmetrical in size.

Because of the nonlinearity of Eq. A.2, closed form solutions for $\langle A_i\rangle$ and $\langle A_iA_j\rangle$ cannot be obtained. Therefore, we make an additional assumption that noise is weak ($\epsilon \ll 1$) and

use the so-called small noise approximation, as outlined below [104], to make the dynamics analytically tractable.

Assuming $\epsilon \ll 1$, we can $A_i(t) = a_i(t) + \epsilon\ X_i(t) + \mathcal{O}(\epsilon^2)$, where $a_i(t)$ is the solution to the deterministic equation $\mathrm{d}a_i/\mathrm{d}t = \gamma_i(a_1, a_2)$. Plugging the series expansion into Eq. A.2 and equating terms of the same order in ϵ, we find to first order in ϵ

$$\begin{aligned} \frac{\mathrm{d}a_i}{\mathrm{d}t} &= \gamma_i(a_1, a_2), \\ \mathrm{d}X_i &= X_i \frac{\partial \gamma_i(a_1, a_2)}{\partial a_i}\mathrm{d}t + \sqrt{\bar{A}_\infty \gamma_i(a_1, a_2)}\ \mathrm{d}W_i. \end{aligned} \tag{A.4}$$

The first equation is simply the deterministic growth law for the average area a_i. The second equation gives the deviation from a_i. Also, note that only a_i appears in the noise term; this is expected because the noise is already first order in ϵ meaning that the first order noise is additive.

Eq. A.4 is linear in X_i, hence it is straightforward to find $\langle X_i X_j \rangle$. It follows that $\langle A_i \rangle = a_i$ and $\langle A_i A_j \rangle - \langle A_i \rangle \langle A_j \rangle = \epsilon^2 \langle X_i X_j \rangle$ to lowest order in ϵ. In fact, one can see that the probability distribution function $P(A_i)$ is a Gaussian distribution up to $\mathcal{O}(\epsilon)$ [104]. With this approximation, FAi can be easily found for a given growth law.

A.3 On the Choice of V in FR Models

In Chapter 2 the hormone concentration was found for FR models to be $[h] \propto \dot{\bar{A}}/V$ where V is the volume of the blood available to the organs for the feedback. We decided to choose $V \propto 2\bar{A}$ for FR models as it is a more natural choice and makes the model more symmetric. Here we show that at least for FR-P model, setting V to be a constant does not affect the behavior of the model qualitatively.

It seems reasonable to assume that a constant blood volume is proportional to the average target size (the largest size the organs can get), $V \propto \bar{A}_\infty$. Then the dynamics for the FR-P model will be

$$\frac{\dot{A}_i}{A_i} = k(A_\infty^{(i)} - A_i) + \lambda \left(c_i \frac{\dot{\bar{A}}}{\bar{A}_\infty} - \frac{\dot{A}_i}{A_i} \right), \tag{A.5}$$

while FR-I model will now look like

$$\begin{aligned} \frac{\dot{A}_i}{A_i} &= k(A_\infty^{(i)} - A_i) + \lambda\, f_i(t) \\ \dot{f}_i(t) &= c_i \frac{\dot{\bar{A}}}{\bar{A}_\infty} - \frac{\dot{A}_i}{A_i}. \end{aligned} \tag{A.6}$$

It is easy to see that the error signal $\dot{f}_i < 0$ at all times, which means that in the FR-I model, the integrated error that the both organs will receive is negative and will never decay to zero. This is similar to the behavior of the knockout mutants that we discussed in Section 2.3.6. The fact that the error signal is negative at all times is much less problematic in FR-P model since it does decay to zero and is not accumulated like in the case of FR-I model. This means that organs are allowed to reach their target size as the magnitude of error signal near steady state is small. The effect is that growth is accelerated compared to the version in Chapter 2 ($\lambda < 0$ in FR-P model so both organs will see a positive error that up-regulates their growth) but reaches the same fixed point (Fig. A.1A). Again, as expected, errors in c_i do not affect the dynamics of this version of FR-P model significantly.

We now study noisy version of Eq. A.5 look at how the knockout behaves in this alternative version of FR-P model (setting $c_i = 1$ for wild type). Firstly, because feedback changes the average growth rate compared to the version in Chapter 2, maturation needs to happen earlier in this version. Then, in the mutant $c_i = 0$, which has an even higher growth rate, we ask organs to stop growing at the same average size as wild type. The FA at this point is higher as seen from (Fig. A.1B-D). Note that unlike the version of FR-P model in Chapter 2, the requirement"stop at the same average size as wild types" is not equivalent to "set $\lambda = 0$ and stop at the same time as wild type." These two statements are only equivalent when the average growth rate of wild type is independent of λ, which was the case for Chapter 2 version of the model but not here.

Overall, normalizing the hormone signal by a constant volume does not seem to qualitatively change the results of the FR-P model, however it makes the FR-I model pathological, which reiterates the sensitivity of that model to model parameters.

A.4 Further Discussion of Error Signal in FR Models

A.4.1 Dependence of Feedback Coefficient on Dynamics of Error Signal

In this section, we take a closer look at the error signal in the FR models to better understand the sign of λ in the models. For convenience, we rewrite the FR-P model as

$$\frac{\dot{A}_i}{A_i} = k(A_\infty^{(i)} - A_i) + \lambda \dot{f}_i, \tag{A.7}$$

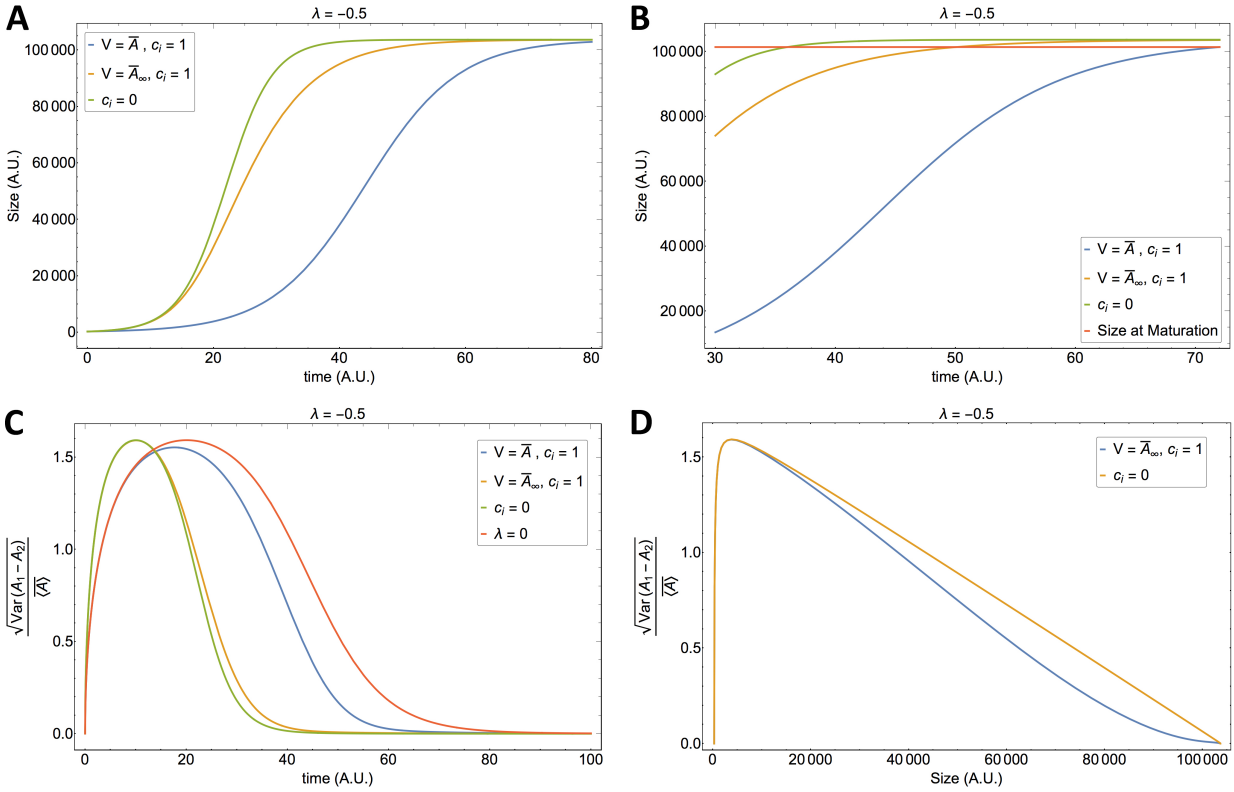

Figure A.1: FR-P model with normalization volume $V = \bar{A}_\infty$. (A) Average growth curves of FR-P model with $V = \bar{A}$ normalization (main text), FR-P model with $V = \bar{A}_\infty$ normalization, and FR-P knockout. (B) To stop growing at the same size as Chapter 2 version of FR-P model, organs with $V = \bar{A}_\infty$ normalization must stop earlier, indicated by the crossing of the red line and the yellow curve. The knockouts must stop even earlier. (C) The FAi curves ($\epsilon = 0.06$ shows that in the $V = \bar{A}_\infty$ version of the model, FA goes down much earlier due to the faster growth rate. Interestingly, the knockout has lower FA at all times, however, since the developmental timing is also accelerated, we should compare the FA at equal sizes. The blue and red dots correspond to the FA at the same average size for wild type and knockout respectively. (D) If we plot the FAi with respect to average size and not time, we see that the knockout mutant shows higher FA at any average size.

where $\dot{f}_i$ is the error signal:

$$\dot{f}_i = \frac{\dot{\bar{A}}}{\bar{A}} - \frac{\dot{A}_i}{A_i}, \tag{A.8}$$

with $c_i = 1$ for simplicity, and FR-I model is defined as before (Eq. 2.15). Understanding the dynamics of the error signal and its integral f_i can give us a better intuition into FR-P and FR-I models.

If feedback is small, the sign of $\dot{f}_i$ is mainly determined by $A_\infty^{(i)} - A_i$. Near the fixed point, the organ that is closer to its target size has a smaller growth rate, so if $A_1 > A_2$, $\dot{f}_1 > 0$ and $\dot{f}_2 < 0$. Thus in the FR-P model, as we discussed in Chapter 2, $\lambda < 0$ is appropriate because we want the larger organ to slow down and smaller organ to speed up. Early dynamics can behave a bit differently. If $A_1(0) > A_2(0)$ and $A_\infty^{(1)} = A_\infty^{(2)}$, $A_\infty^{(1)} - A_1(0) < A_\infty^{(2)} - A_2(0)$ and thus $\dot{f}_1 > 0$ and $\dot{f}_2 < 0$ from the beginning (Fig. A.2A). However, if for example $A_1(0) = A_2(0)$ and $A_\infty^{(1)} > A_\infty^{(2)}$, initially A_1 has a higher growth rate and $\dot{f}_1(0) < 0$ and $\dot{f}_2(0) > 0$ while the late time behavior is the same as before, meaning that $\dot{f}_i$ change sign (Fig. A.2C). Therefore, the FR-P model will favor $\lambda > 0$ early on but again a $\lambda < 0$ is favored later in growth. However, in this case, feedback ultimately fails regardless of the sign of feedback because FR-P cannot correct errors in target size.

The situation for FR-I model is different because the integral of error signal is the important parameter. In the first example ($A_1(0) > A_2(0)$ and $A_\infty^{(1)} = A_\infty^{(2)}$), since $\dot{f}_1 > 0$ and $\dot{f}_2 < 0$ at all times, $f_1(t) > 0$ and $f_2(t) < 0$ as can be seen in Fig. A.2B (assuming $f_i(0) = 0$). Then, clearly $\lambda > 0$ increases the size difference as we saw in Chapter 2. However, $\lambda < 0$ is not good either because it will force A_1 to become smaller than A_2 and instead of reaching the same target size, organs will reach different sizes with $A_1(t \to \infty) < A_2(t \to \infty)$ even though $A_\infty^{(1)} = A_\infty^{(2)}$. In the second example, even though $\dot{f}_i$ change sign during the growth, the sign of f_i is determined by $\dot{f}_i(0)$ because the magnitude of $\dot{f}_i$ is smaller later on as the organs approach steady state (Fig. A.2D). Thus, $f_1(t) < 0$ and $f_2(t) > 0$, thus $\lambda > 0$ is appropriate for FR-I model in this case.

We also add that in a situation where say $A_1(0) > A_2(0)$ and $A_\infty^{(1)} > A_\infty^{(2)}$, f_i also can change sign in addition to $\dot{f}_i$ during the growth, suggesting that $\lambda < 0$ in FR-I can bring down A_1, which then can actually lower the final FA; however, the magnitude of λ is highly dependent on $A_i(0)$, which again is the main issue with FR-I model (Fig. A.3).

Overall, this analysis suggests that when FR-P is helpful (same target sizes), $\lambda < 0$ is favored, and when FR-I is useful (different target sizes but same initial conditions), $\lambda > 0$ is appropriate.

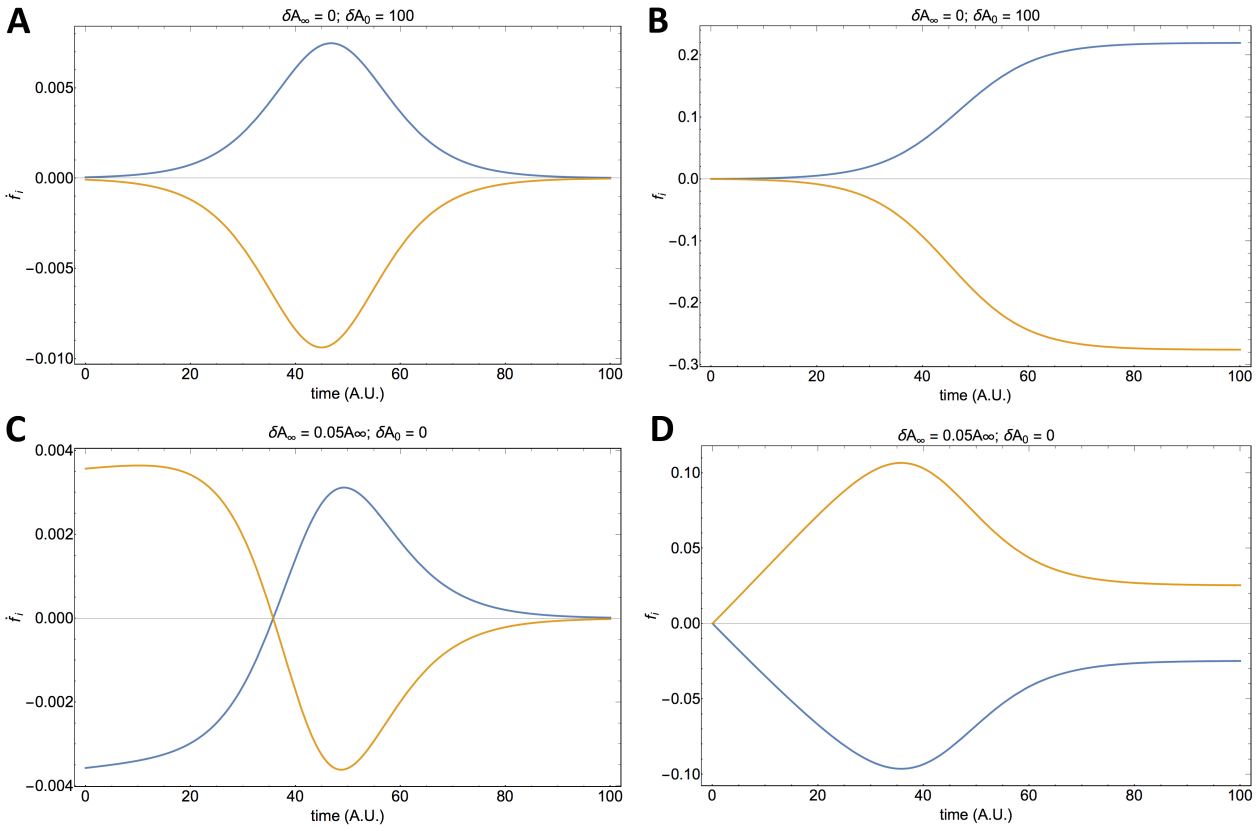

Figure A.2: Behavior of $\dot{f}_i$ and f_i based on different initial conditions. (A-B) If $A_1(0) > A_2(0)$ and $A_\infty^{(1)} = A_\infty^{(2)}$, $\dot{f}_1 > 0$ and $\dot{f}_2 < 0$ at all times. $(A_1(0) = 264, A_2(0) = 164.)$ (C-D) If $A_1(0) = A_2(0)$ and $A_\infty^{(1)} > A_\infty^{(2)}$, $\dot{f}_i$ change sign but f_i do not. Here, blue curves represent $\dot{f}_1$ and f_1 while yellow curves represent $\dot{f}_2$ and f_2.

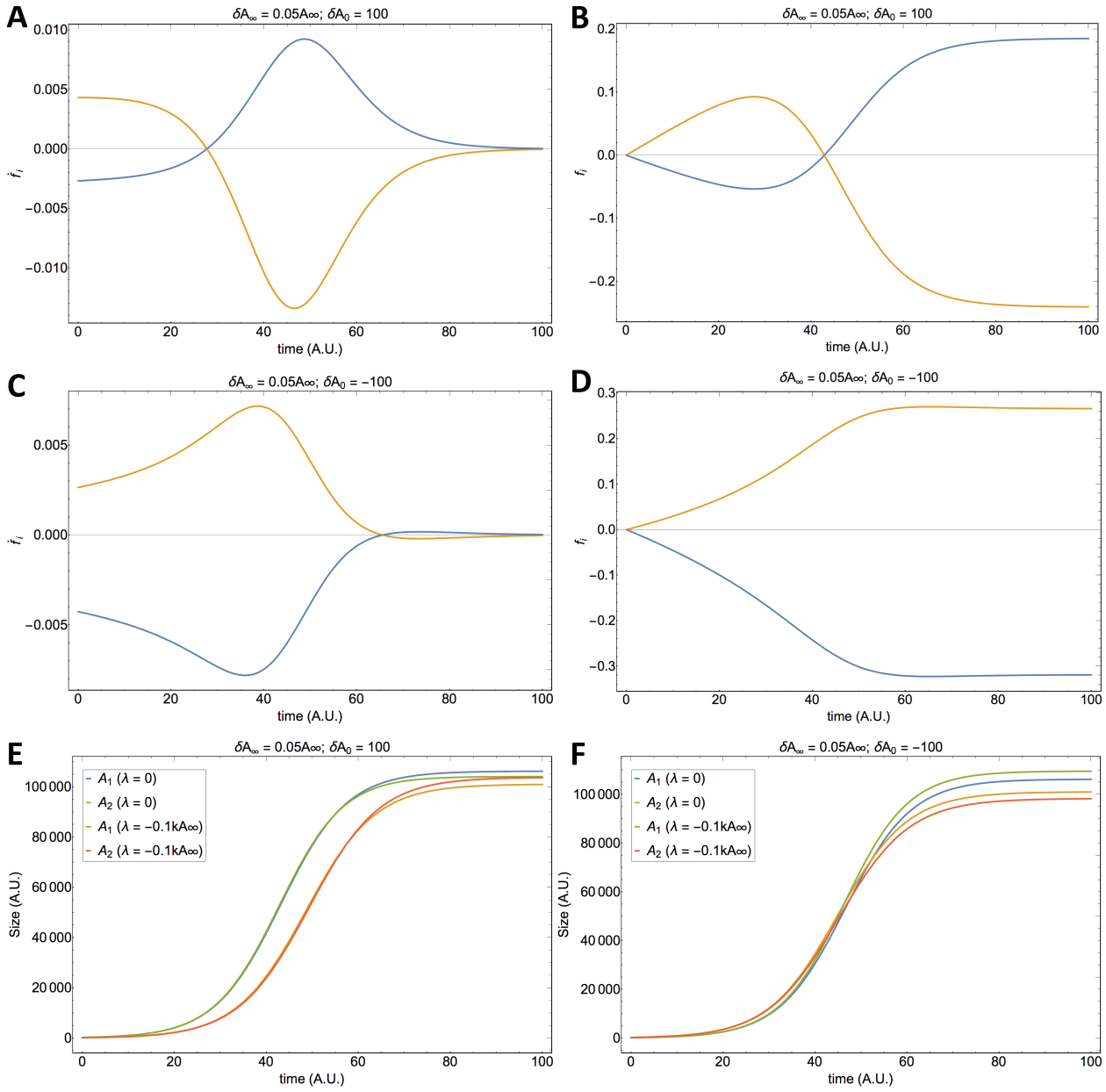

Figure A.3: Negative feedback in FR-I model and its dependence on initial conditions. (A-B) If $A_1(0) > A_2(0)$ and $A_\infty^{(1)} > A_\infty^{(2)}$, negative feedback may be favorable in FR-I model because of f_i's signs near the end (here $A_1(0) = 264, A_2(0) = 164$). (C-D) A different initial condition $(A_1(0) = 164, A_2(0) = 264)$ will change the behavior of f_i, thus can lead to the failure of FR-I model. Here f_i do not change sign anymore. (E-F) FR-I model can correct errors in target size for a specific choice of δA_0 (E) but the same feedback will fail for a different initial condition (F). In (A-D) blue curves represent $\dot{f}_1$ and f_1 while yellow curves represent $\dot{f}_2$ and f_2.

A.4.2 Initial Conditions of f_i in FR-I Model

Here, we derive the initial conditions of f_i that we used in Section 2.3.6 (Eq. 2.16). We can see from Eq. A.8 that

$$\dot{f}_2 = \frac{\dot{A}_1 A_2 - \dot{A}_2 A_1}{(A_1 + A_2)A_2} = -\frac{A_1}{A_2}\dot{f}_1. \tag{A.9}$$

With a bit of algebra we can find $f_2(t)$ in terms of $f_1(t)$ and other parameters.

$$\begin{aligned}
\frac{\dot{A}_1 A_2 - \dot{A}_2 A_1}{A_2} &= A_2 \frac{\mathrm{d}}{\mathrm{d}t}\left[\frac{A_1}{A_2}\right] = A_1 \frac{\mathrm{d}}{\mathrm{d}t}\left[\log\frac{A_1}{A_2}\right] \\
\Rightarrow (A_1 + A_2)\dot{f}_2 &= A_1 \frac{\mathrm{d}}{\mathrm{d}t}\left[\log\frac{A_1}{A_2}\right] \Rightarrow \dot{f}_2 + \frac{A_2}{A_1}\dot{f}_2 = \dot{f}_2 - \dot{f}_1 = \frac{\mathrm{d}}{\mathrm{d}t}\left[\log\frac{A_1}{A_2}\right] \\
\Rightarrow f_2 &= f_1 + \log\frac{A_1}{A_2} + C
\end{aligned} \tag{A.10}$$

We can easily find the constant C by looking at boundary conditions at $t \to \infty$. At steady state, we want the feedback to correct errors in target size, so we ask $A_1(t \to \infty) = A_2(t \to \infty) = \bar{A}_\infty$. Then $C = f_2(t \to \infty) - f_1(t \to \infty)$. From Eq. 2.15 we also have

$$f_i(t \to \infty) = \frac{k(A_\infty^{(i)} - \bar{A}_\infty)}{\lambda}. \tag{A.11}$$

So,

$$C = \frac{k\,\delta A_\infty}{\lambda}. \tag{A.12}$$

Now we can write $f_2(t)$ in terms of $f_1(t)$ and arrive at Eq. 2.16:

$$f_2(t) = f_1(t) + \log\frac{A_1(t)}{A_2(t)} + \frac{k\,\delta A_\infty}{\lambda} \tag{A.13}$$

For initial conditions, we argued that the most natural choice for initial conditions are $f_i(0) = 0$, which constrains $A_1(0) = A_2(0)$ and a $\lambda \gg k\,\delta A_\infty$ for perfect correction of errors in target size. Other choices of $f_i(0)$ will lead to nonbiological dependence of the internal integrator of each organ depending on the other.

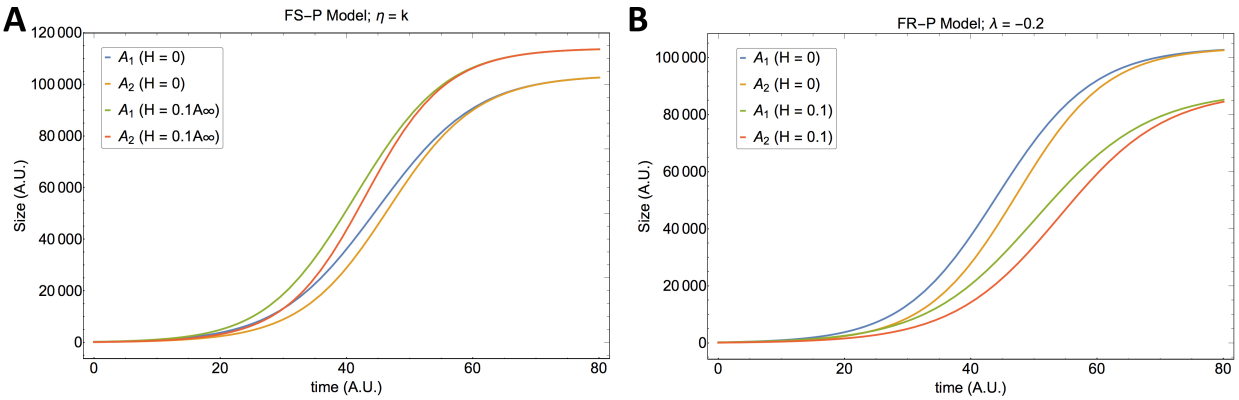

Figure A.4: Overexpression of signal in FS-P and FR-P models. (A) In the FS-P model, overexpression increases the final sizes and the growth rate. (B) overexpression of signal in FR-P model lowers the growth rate and the final sizes. ($\delta A_\infty = 0$, $A_1(0) = 264$, $A_2(0) = 164$.)

A.5 Overexpression of Coordination Signal in FS-P and FR-P Models

In this section, we study the behavior of our proportional feedback models to overexpression of signal. Because the feedback coefficients have the oposite signs in FS-P and FR-P models, we expect them to behave differently in response to overexpression. Overexpression can be achieved by simply adding a constant H to the error signal, which looks like

$$\frac{\dot{A}_i}{A_i} = k(A_\infty^{(i)} - A_i) + \eta(c_i\bar{A} - A_i + H), \tag{A.14}$$

for FS-P model, and

$$\frac{\dot{A}_i}{A_i} = k(A_\infty^{(i)} - A_i) + \lambda\left(c_i\frac{\dot{\bar{A}}}{\bar{A}} - \frac{\dot{A}_i}{A_i} + H\right), \tag{A.15}$$

for FR-P model. Indeed, overexpression can distinguish between these two models: In FS-P model, overexpression leads to growth acceleration and reaching larger final sizes, whereas the in FR-P model,the effect is opposite. Fig. A.4 shows the different behaviors, where we assumed same target sizes for fair comparison. If target sizes are not the same, note that in the steady state, $\delta A(t \to \infty)$ is independent of H in both models. However, since the average size is affected by it, FS-P model would show lower FA while FR-P model would show a higher FA than wild type.

A.6 Regulation of Noise Strength

One could imagine that in the wild type animals the hormone is only involved in regulating homeostasis in an organ autonomous manner to ensure a low noise level across the organ, allowing for a low final FA. Then, by knocking it out, could lead to a higher FA at maturation. Here we outline how one would go about modeling this process using our small noise approximation.

Assume that the coordination signal only regulates ϵ and not the timing and does not play any role in feedback between organs. If then we knock out the hormone, ϵ would go up, leading to higher FA at maturation since FAi is linearly dependent on ϵ as we showed in Eq. 2.19. An interesting experimental result is found if we do the time dependent control of the signal as we did for *Drosophila* in Section 2.4.

Say we have obtained the noise strength for wild type (ϵ) and for knock out ϵ^* from experimental data. Then, if we activate the signal sometime in the middle of growth, T^*, noise strength would go down from $\epsilon^* \to \epsilon$ and final FA will be larger than wild type but lower than knockout. One thing to note is that we want continuity in the variance after changing ϵ. This in the context of small noise approximation means that $\epsilon^* \langle X_i X_j \rangle_{T^*} = \epsilon \langle X_i X_j \rangle_{T^*}$ so that $\langle A_i A_j \rangle_{before} = \langle A_i A_j \rangle_{after}$.

We applied this procedure to the fly data that we used in Section 2.4 to see what the GAL80^{ts} experiment would look like if Dilp8 were to only regulate the strength of noise. The result is shown in Fig. A.5, where we can see a stark difference between this case and the FR-P model explored in Chapter 2 (Fig. 2.7D). Namely, *dilp8* control of final FA is very sensitive to T^*. This means that if somehow *dilp8* is expressed just a few hours late, the final FA would look much more like a knockout which definitely would not be desirable.

In the final section, we will take a brief look at the case that there is no noise in growth rate but in the target size, and ask what role can the coordinating signal play in that scenario.

A.7 Noisy Target Size

In this section, we will briefly look at the scenario in which fluctuations are solely affecting the target sizes and growth rate remains deterministic. We will then assume that the coordination signal only reduces noise in target size.

Assume that each organ grows according to the logistic equation

$$\dot{A}_i = k A_i (a_\infty^{(i)} - A_i), \tag{A.16}$$

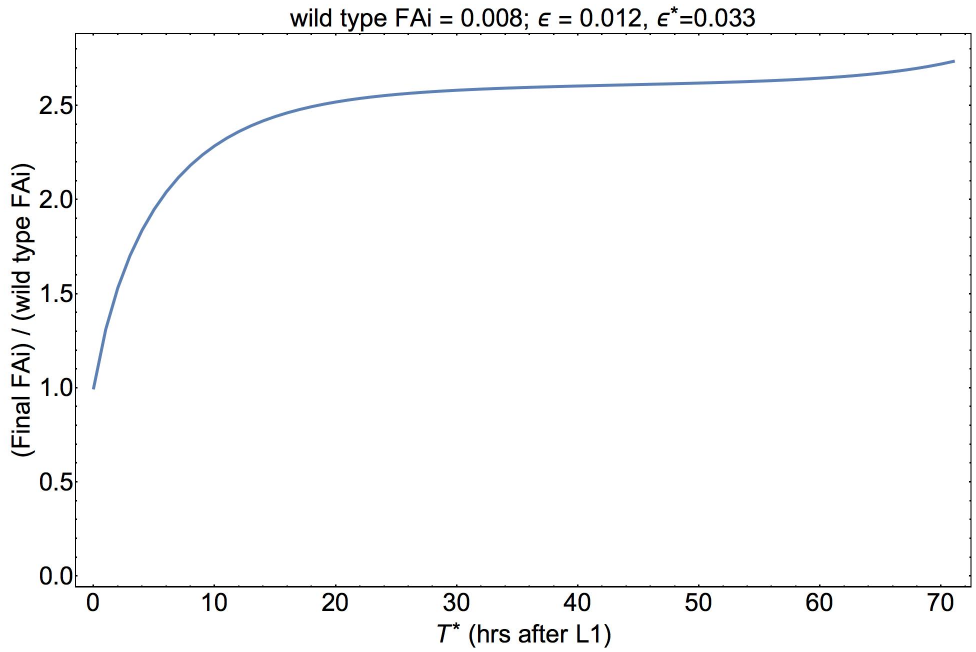

Figure A.5: The effect of time dependent activation of *dilp8* on final FA if it is only involved in an autonomous error correction in normal physiological conditions. In this case, the final FA is very sensitive to the time T^* that *dilp8* is activated early on, so that if it is activated just a few hours late, final FA would be much higher and closer to knockouts.

but with target size $a_\infty^{(i)}$ chosen from a Gaussian distribution with mean $\bar{A}_\infty$ and standard deviation σ_∞:

$$P(a_\infty^{(i)}) \propto \exp\left\{-\frac{(a_\infty^{(i)} - \bar{A}_\infty)^2}{2\sigma_\infty^2}\right\}. \tag{A.17}$$

In this case, the probability of an organ with size $A_(t)$ at time t is given by a convolution:

$$P(A(t)) = \int P(A(t)|a_\infty)P(a_\infty)\ \mathrm{d}a_\infty \tag{A.18}$$

$P(A(t)|a_\infty)$ is the conditional probability, a delta function

$$P(A(t)|a_\infty) = \delta(A(t) - a(t, a_\infty)), \tag{A.19}$$

where $a(t, a_\infty)$ is the solution to $\dot{a} = k\alpha(a_\infty - a)$. In other words, each a_∞ chosen from the distribution $P(a_\infty)$ will lead to a deterministic logistic growth since the assumption is that there is no noise in the growth rate. But we will have a distribution for the organ sizes given by Eq. A.18 leading to an FA at maturation. The FA at maturation will be a function of σ_∞.

In the case of fluctuations in growth rate, we saw that noise decayed to zero as the organs

approach the target size. This property of the noisy dynamics results in a dependence of FA on the timing of maturation: the more maturation is delayed, the less FA we have.

In this case however, unlike noise in growth rate, noise does not decay to zero as the organs approach their final size. Instead, it approaches a fixed value determined by σ_∞. Therefore, the final FA is almost entirely determined by σ_∞.

If the Coordination signal can lower σ_∞, it will decrease the final FA and knocking it out will increase σ_∞ leading to higher FA. It is hard to say anything more about say time dependent expression of the signal as in the GAL80^{ts} experiments without extra assumptions about the mechanism by which σ_∞ is regulated by the signal. It would be interesting for future studies to explore, say, temporal noise in target size, i.e. the organs start with some error in their target size that is lowered as they approach this target size.

APPENDIX B
Further Discussion of Statistics of Growing Tissues

B.1 Introduction

In this Appendix, we present several derivations and calculations that we skipped in Chapter 4 and some theoretical background regarding the quantities of interest. First, we derive our expression for the stress tensor (Eq. 4.1) from the general nonlinear theory of morphoelasticity [59]. Next, we show a linearization of the growth dynamics in Eq. 4.3 leading to Eq. 4.4 in Chapter 4. Then, we discuss our choice of time derivative and some subtleties associated with material time derivatives of tensors. In the same section, we also discuss the equivalence of our model with the fluidization picture proposed by Ranft et al. [6]. After that, we show the full derivation of the spatial density-density correlation function (Eq. 4.7) and derive an expression for the time-dependent density-density correlation function. We then consider the effect of including gradients of the stress tensor in the growth dynamics and verify our claim in Chapter 4 that this is not qualitatively different from the simple stress feedback we presented there. Next, we show the extension of our model for isotropic growth to higher dimensions. Then we move on to anisotropic growth and provide a more detailed derivation of the anisotropic growth dynamics and soft modes (Eqs. 4.14–4.16), which we will then use in our calculation of clone statistics. In the final section of this SI, we return to the special case of no net growth, $\gamma_0 = 0$, recovering several results from [6].

B.2 Derivation of Cauchy Stress from Nonlinear Morphoelasticity

In this section, we show how the expression for the Cauchy stress tensor given in Eq. 4.1 of Chapter 4 (and valid in the limit of small deviations from uniform growth) can be obtained

by linearizing the general, nonlinear theory of morphoelasticity. We quote here without justification a number of well-established results in morphoelasticity; for derivations and a more in-depth explanation, the interested reader is referred to [59]. Following the morphoelasticity literature, we call the fully nonlinear Cauchy stress tensor T_{ij}, reserving σ_{ij} for the linearized version used in Chapter 4.

The theory of morphoelasticity is an extension of finite strain theory, applied when deformations can no longer be considered infinitesimal. Morphoelasticity deals with arbitrary deformations due to growth. The deformation gradient $F_{ij} = \partial r_i/\partial R_j$ is defined which maps the Eulerian to Lagrangian coordinates. The underlying assumption of morphoelasticity [63] is that we can decompose the deformation gradient into a growth part G followed by an elastic deformation denoted by A, F = AG. Then, the Cauchy stress tensor is taken to be related in the usual manner to the elastic part of the deformation:

$$\mathrm{T} = J^{-1}\mathrm{A}\frac{\partial W}{\partial \mathrm{A}} = 2J^{-1}\mathrm{A}\frac{\partial W}{\partial \mathrm{A}^T\mathrm{A}}\mathrm{A}^T$$

where $J = \det(\mathrm{A})$ and W is the elastic energy density per unit volume of the so-called virtual configuration, which we can imagine as the state of the material after growth but before any elastic deformations. For an isotropic, neo-Hookean material,

$$W = \frac{1}{2}\mathcal{A}_{ijkl}\ \epsilon_{ij}\ \epsilon_{kl} = \frac{1}{2}(\lambda\ \epsilon_{ll}^2 + 2\mu\ \epsilon_{ij}^2),$$

where $\mathcal{A}_{ijkl} = \lambda\delta_{ij}\delta_{kl} + \mu(\delta_{ik}\delta_{jl} + \delta_{il}\delta_{jk})$ is the elasticity tensor for an isotropic body, $\epsilon = (\mathrm{A}^T\mathrm{A} - \mathbb{1})/2$ is the morphoelastic strain tensor, and summation over repeated indices is implied. It is helpful to express A in terms of F and G. Therefore we define a new strain tensor

$$\epsilon' = \mathrm{G}^T\epsilon\ \mathrm{G} = (\mathrm{F}^T\mathrm{F} - \mathrm{G}^T\mathrm{G})/2.$$

Then with the new elastic tensor

$$\mathcal{A}'_{ijkl} = \lambda(\mathrm{G}^T\mathrm{G})^{-1}_{ij}(\mathrm{G}^T\mathrm{G})^{-1}_{kl} + \mu\left((\mathrm{G}^T\mathrm{G})^{-1}_{ik}(\mathrm{G}^T\mathrm{G})^{-1}_{jl} + (\mathrm{G}^T\mathrm{G})^{-1}_{il}(\mathrm{G}^T\mathrm{G})^{-1}_{jk}\right),$$

the energy density $W = \mathcal{A}'_{ijkl}\ \epsilon'_{ij}\ \epsilon'_{kl}/2$.

Now we linearize for small $\widetilde{G}_{ij}/\bar{G}$ (and $w_{ij}/\bar{G}$ because deformations are of the same order as growth fluctuations) to get the results in the limit we are interested in. First, we note that $\mathrm{A} = \mathbb{1} + \mathcal{O}(\widetilde{\mathrm{G}}/\bar{G})$ because uniform growth does not cause any deformations. Then $\epsilon = \mathcal{O}(\widetilde{\mathrm{G}}/\bar{G})$ and we can approximate

$$\mathrm{T} \approx 2\ \partial W/\partial(\mathrm{A}^T\mathrm{A}) = \partial W/\partial\epsilon. \tag{B.1}$$

To linear order in $w_{ij}/\bar{G}$ and $\widetilde{G}_{ij}/\bar{G}$, $(\mathrm{F}^T\mathrm{F})_{ij} = \partial_i \mathbf{r} \,.\, \partial_j \mathbf{r} \approx \bar{G}^2\delta_{ij} + 2\bar{G}\; w_{ij}$ and $(\mathrm{G}^T\mathrm{G})_{ij} \approx \bar{G}^2\delta_{ij} + 2\bar{G}\; \widetilde{G}_{ij}$ respectively. Therefore, we can explicitly write out ϵ'_{ij}:

$$\epsilon'_{ij} \approx \bar{G}^2\epsilon_{ij} \approx \bar{G}(w_{ij} - \widetilde{G}_{ij}),$$

and so $\epsilon_{ij} \approx (w_{ij} - \widetilde{G}_{ij})/\bar{G}$. This allows us to express W and thus T in terms of w_{ij} and $\widetilde{G}_{ij}$. The elastic energy density to linear order in $w_{ij}/\bar{G}$ and $\widetilde{G}_{ij}/\bar{G}$ is

$$W \approx \frac{1}{2\bar{G}^2}\left[\lambda(w_{ll} - \widetilde{G}_{ll})^2 + 2\mu(w_{ij} - \widetilde{G}_{ij})^2\right].$$

Using Eq. B.1, the linearized Cauchy stress tensor is

$$T_{ij} \approx \sigma_{ij} = \frac{1}{\bar{G}}\left[\lambda(w_{ll} - \widetilde{G}_{ll})\delta_{ij} + 2\mu(w_{ij} - \widetilde{G}_{ij})\right], \tag{B.2}$$

which is Eq. 4.1 in Chapter 4.

As a side note, the target metric formalism, an equivalent framework to morphoelasticity, also leads to the same result [64]. In fact, the new strain tensor ϵ' that we defined is the strain tensor used in that formalism. In target metric formalism, a target metric $\bar{g}_{ij}$ is defined denoting the grown, stress free configuration, which often cannot be embedded in real space. $\bar{g}_{ij} = (\mathrm{G}^T\mathrm{G})_{ij}$ in morphoelasticity formalism. The metric defining the final configuration (denoted by g_{ij}) is indeed $(\mathrm{F}^T\mathrm{F})_{ij}$, and the strain tensor is $\epsilon'_{ij} = (g_{ij} - \bar{g}_{ij})/2$. We found it easier to work with ϵ'_{ij} than with ϵ_{ij} because we had explicit expressions for g_{ij} and $\bar{g}_{ij}$ to linear order.

B.3 Linearized Growth Dynamics

In this section, we show how to get to the linearized growth dynamics equation (Eq. 4.4 in Chapter 4) starting from the tensorial dynamics in Eq. 4.3.

Γ in Eq. 4.3 could be a 4th rank tensor in the most general case, but here we show that it simplifies to a 2nd rank tensor in the limit of small fluctuations. In particular we write:

$$\Gamma_{ijkl} = \gamma_0\delta_{ij}\delta_{kl} + K_{ijkl}(\sigma) + \xi_{ijkl}$$

where $K_{ijkl}(\sigma)$ is first order in the stress tensor and ξ_{ijkl} is the noise. Then, knowing $\partial_t\bar{G} = \gamma_0\bar{G}$ we find from $\partial_t\mathrm{G} = \Gamma\mathrm{G}$

$$\partial_t\widetilde{G}_{ij} = \gamma_0\widetilde{G}_{ij} + K_{ijkl}G_{kl} + \xi_{ijkl}G_{kl}$$

or

$$\partial_t \left[\frac{\widetilde{G}_{ij}}{\bar{G}} \right] = (K_{ijkl} + \xi_{ijkl}) \left(\delta_{kl} + \frac{\widetilde{G}_{kl}}{\bar{G}} \right)$$

Since K_{ijkl} is first order in the stress tensor and thus $\mathcal{O}(\widetilde{G}_{ij}/\bar{G})$, we can ignore $K_{ijkl}\widetilde{G}_{kl}/\bar{G}$. Thus, to lowest order in $\widetilde{G}_{kl}/\bar{G}$, the most general form of feedback allowed by symmetries of the system is $K_{ijkl}\delta_{kl} = K_{ijll} \approx c\ \sigma_{ll}\ \delta_{ij}/2 + c^{(d)}\ \sigma_{ij}^{(d)}$, where $\sigma_{ij}^{(d)}$ denotes the traceless part of the stress tensor and the superscript (d) stands for deviatoric. The noise term is evaluated in the weak noise limit, meaning that we can write $G_{kl} \approx \bar{G}\delta_{kl}$ and $\xi_{ijkl}G_{kl}/\bar{G} \approx \xi_{ijkl}\delta_{kl} = \xi_{ij}$ where ξ_{ij} is now a 2nd rank tensorial noise. Putting all of this together we arrive at the following growth equation, Eq. 4.4 in Chapter 4:

$$\partial_t \left[\frac{\widetilde{G}_{ij}}{\bar{G}} \right] = c\ \sigma_{ll}\ \frac{\delta_{ij}}{2} + c^{(d)}\sigma_{ij}^{(d)} + \xi_{ij}. \tag{B.3}$$

B.4 On the Choice of Time Derivative and Connection to Ranft et al. [6]

In this section and this section only, we redefine ∂_t to be the time derivative at fixed Eulerian, not Lagrangian, coordinates. Therefore, the time derivative at fixed Lagrangian coordinates used in every other section becomes $\partial_t + \mathbf{v}.\nabla_{\mathbf{r}} \equiv \mathrm{d}/\mathrm{d}t$, where $\mathbf{v}$ is the velocity of dilation (i.e. flow velocity).

In specifying the dynamics of the tensor G in Chapter 4, we suggested that it should have the form $\mathrm{dG}/\mathrm{d}t = \Gamma\mathrm{G}$ (compare Eq. 4.3; here, as just explained, we have written the time derivative at fixed Lagrangian coordinates as $\mathrm{d}/\mathrm{d}t$). It has been argued, however (e.g. ref. [6]), that a better choice would be $\mathrm{DG}/\mathrm{D}t = \Gamma\mathrm{G}$, where $\mathrm{D}/\mathrm{D}t$ is the convected corotational time derivative defined, for any tensor A_{ij}, as $(\mathrm{D}A_{ij}/\mathrm{D}t) = \partial_t A_{ij} + v_l\partial_{r_l}A_{ij} + \omega_{il}A_{lj} + \omega_{jl}A_{il}$, where v_i is the velocity and $\omega_{ij} = (\partial_{r_i}v_j - \partial_{r_j}v_i)/2$ is the vorticity of the flow. This derivative differs from $\mathrm{d}/\mathrm{d}t$ by the terms proportional to ω_{ij}. In the most general case, the choice between these time derivatives is a subtle one, which potentially depends both on the biological assumptions one wants to make and on technical questions like whether G_{ij} is defined to include rigid rotations. (See, e.g., ref. [59] for more on the question of rigid rotations and the growth tensor.) To leading order in small deviations from uniform growth (and thus in small displacements), however, it turns out we can sidestep this issue entirely: the two time derivatives agree to this order, as we now demonstrate.

First, notice that any time derivative of G contains a derivative of $\bar{G}$ and a derivative of $\widetilde{G}$. The former is the same for all of the possible time derivatives, because $\bar{G}$ has no space

dependence and the parts proportional to ω_{ij} must vanish because of its antisymmetry. For the part proportional to $\widetilde{G}$, to leading order we can drop any terms where $\widetilde{G}$ is multiplied by something small. Now the velocity field is $v_l = \gamma_0 r_l + \mathcal{O}(w_l)$. Thus, noting that w_l is first order small and that $\gamma_0 r_l$ is an irrotational flow, we conclude that ω_{ij} is first order small and so can be dropped when it multiplies $\widetilde{G}$. We are then left with the bare time derivative and a convection term proportional to γ_0 (i.e. $\partial_t + \gamma_0 r_l \partial_{r_l}$), which are the same for the two proposed choices $\mathrm{d}/\mathrm{d}t$ and $\mathrm{D}/\mathrm{D}t$.

Now, we show that, in the limit of small growth non-uniformities, our formalism is equivalent to that of Ranft et al., who show fluidization of growing tissues. In particular, we derive Eqs. 12 and 13 in their paper. Working in Eulerian coordinates, they show in Eq. 12 that in a growing tissue, the trace of the stress tensor follows

$$\frac{\mathrm{d}}{\mathrm{d}t}\sigma_{ll} = 2\chi[v_{ll} - \kappa(\rho)], \tag{B.4}$$

where $\mathrm{d}/\mathrm{d}t = \partial_t + \mathbf{v}.\nabla_{\mathbf{r}}$ is the convected time derivative, $\chi = \lambda + \mu$ is the bulk modulus in two dimensions, κ the growth rate, and v_{ij} is the rate of strain tensor, defined with respect to the Eulerian coordinates. This means that in contrast to our spatial derivatives, theirs is taken with respect to r_i. In Eq. 13 of their paper, they show that the traceless part of the stress tensor relaxes, which they use to conclude that the tissue acts viscoelastic:

$$\left(1 + \tau_a \frac{\mathrm{D}}{\mathrm{D}t}\right) \sigma_{ij}^{(d)} = 2\tau_a \mu \, v_{ij}^{(d)}, \tag{B.5}$$

where τ_a is the relaxation time.

First, we simplify their equation for the trace, Eq. B.4, in the limit of small growth non-uniformities. They have shown in their Eq. 11 that near the isotropic homeostatic state, the trace of stress relaxes in a similar fashion to the traceless part, with relaxation time τ. Here, we show that we only really need mostly uniform growth with small deviations to see the relaxation.

Looking at Eq. B.4, we can see that if ρ is uniform, $\sigma_{ll} = 0$. We use this fact to expand both v_{ll} and κ for small non-uniformities (i.e. $\rho = \rho_0 + \delta\rho$ and $\delta\rho \ll \rho_0$) keeping in mind that at $\rho = \rho_0$, $v_{ll} = \kappa(\rho_0) = \bar{\kappa}$. We write $\kappa = \bar{\kappa} + \delta\kappa$ and $v_i = \bar{v}_i + \delta v_i$ with $\bar{v}_i = \gamma_0 r_i$ and $\bar{\kappa} = 2\gamma_0$. From v_i we find $v_{ij} = \gamma_0 \delta_{ij} + \delta v_{ij}$. We also write $\delta\kappa$ in terms of $\delta\rho$ as $\delta\kappa \approx \tau^{-1}\delta\rho/\rho_0$ just as Ranft et al. did in the homeostatic case. We then use $\sigma_{ll} = -2\chi\delta\rho/\rho_0$ from Eq. 6 in their paper to put all of this together and arrive at the following equation that shows relaxation

of the trace of stress for almost uniform growth in a similar manner to the traceless part:

$$\left(1+\tau\frac{\mathrm{d}}{\mathrm{d}t}\right)\sigma_{ll}=2\tau\chi\delta v_{ll}. \tag{B.6}$$

Now, we bring our attention to our formalism and show that we get the same relaxations as Eqs. B.5 and B.6. Firstly, we ignore the noise in the growth dynamics and assume the density fluctuations are given as an initial condition. Starting from Eq. B.2, we can take the time derivative to get:

$$\frac{\mathrm{d}}{\mathrm{d}t}\sigma_{ij}=\left[\lambda\left(\frac{\mathrm{d}}{\mathrm{d}t}\left[\frac{w_{ll}}{\bar{G}}\right]-\frac{\mathrm{d}}{\mathrm{d}t}\left[\frac{\widetilde{G}_{ll}}{\bar{G}}\right]\right)\delta_{ij}+2\mu\left(\frac{\mathrm{d}}{\mathrm{d}t}\left[\frac{w_{ij}}{\bar{G}}\right]-\frac{\mathrm{d}}{\mathrm{d}t}\left[\frac{\widetilde{G}_{ij}}{\bar{G}}\right]\right)\right].$$

$(\mathrm{d}/\mathrm{d}t)[w_{ij}/\bar{G}]$ in our framework is actually δv_{ij}. The factor of $1/\bar{G}$ comes from the fact that δv_{ij} is defined in the Eulerian coordinates and $\partial_{r_i}\approx\partial_{R_i}/\bar{G}$. Replacing $(\mathrm{d}/\mathrm{d}t)[\widetilde{G}/\bar{G}]$ with Eq. B.3 and dropping the noise term, we get the following equations for the trace and traceless parts of the stress tensor:

$$\begin{aligned}\left(1+\frac{1}{2\chi c}\frac{\mathrm{d}}{\mathrm{d}t}\right)\sigma_{ll} &= \frac{1}{c}\delta v_{ll}\\ \left(1+\frac{1}{2\mu\, c^{(d)}}\frac{\mathrm{d}}{\mathrm{d}t}\right)\sigma^{(d)}_{ij} &= \frac{1}{c^{(d)}}\delta v^{(d)}_{ij}\end{aligned}$$

The first equation is the same as Eq. B.6 if we define $\tau=1/(2\chi c)$. Setting $\tau_a=1/(2\mu c^{(d)})$, the second equation is also the same as Eq. B.5 if we replace $\mathrm{D}/\mathrm{D}t$ with $\mathrm{d}/\mathrm{d}t$ (which we may do to leading order in growth non-uniformities, as explained at the beginning of this section), and notice that $v^{(d)}_{ij}=\delta v^{(d)}_{ij}$, easy to see from $v_{ij}=\gamma_0\delta_{ij}+\delta v_{ij}$.

B.5 Isotropic Density-density Correlations

In Chapter 4 we claimed that the spatial density-density correlation shows a power law behavior (Eq. 4.7) while the time correlations decay exponentially. Here, we show the full calculations and express the correlation functions including the prefactors, which we omitted in Chapter 4. We will only focus on the isotropic case as the dynamics of density fluctuations is the same in isotropic and anisotropic growth, and effectively we just need to change $k\to k+k^{(d)}$ to go from isotropic to anisotropic, as can be seen by comparing Eqs. 4.6 and 4.14.

Starting from Eq. 4.6, we first do the calculations in fixed Lagrangian coordinates to bypass the complexities associated with large convected terms due to the uniform tissue

dilation. ξ is naturally defined in the Eulerian coordinates, but in the weak noise limit, we can easily find the noise correlators in the Lagrangian coordinates. First, let us naïvely take the noise to be delta correlated in both time and space, so that in Eulerian coordinates $\langle \xi(\mathbf{r},t)\xi(\mathbf{r}',t')\rangle = D\delta(\mathbf{r}-\mathbf{r}')\delta(t-t')$. In Lagrangian coordinates, we approximate $\mathbf{r} \approx \bar{G}\mathbf{R}$ and write $\langle \xi(\mathbf{R},t)\xi(\mathbf{R}',t')\rangle = D\delta(\mathbf{R}-\mathbf{R}')\delta(t-t')/\bar{G}^2$, where D is the noise strength. We now solve for $\delta\rho(\mathbf{R},t)$ from Eq. 6:

$$\delta\rho(\mathbf{R},t) = \rho_0 \frac{\mu}{\lambda+2\mu} e^{-kt} \int_0^t \xi(\mathbf{R},t_1) e^{kt_1} \mathrm{d}t_1.$$

Here, the initial condition is omitted because it will not matter at long time, where we expect to reach a steady state. Then, for the correlation function, we have:

$$\begin{aligned} \frac{1}{\rho_0^2}\langle \delta\rho(\mathbf{R},t)\delta\rho(\mathbf{R}',t)\rangle &= e^{-2kt}\frac{\mu^2}{(\lambda+2\mu)^2}\int_0^t \mathrm{d}t_1\ \mathrm{d}t_2\ \langle \xi(\mathbf{R},t_1)\xi(\mathbf{R}',t_2)\rangle\, e^{k(t_1+t_2)} \\ &= \frac{\mu^2}{(\lambda+2\mu)^2} D e^{-2kt}\int_0^t \mathrm{d}t_1 \delta(\mathbf{R}-\mathbf{R}') e^{-2\gamma_0 t_1} e^{2kt_1} \end{aligned} \tag{B.7}$$

From now on use $D' = \mu^2 D/(\lambda+2\mu)^2$. Because we want to find the correlation at fixed Eulerian coordinates at time t, we can write $\mathbf{R} = e^{-\gamma_0 t}\mathbf{r}$:

$$\frac{1}{\rho_0^2}\langle \delta\rho(\mathbf{r},t)\delta\rho(\mathbf{r}',t)\rangle = \frac{D'}{2(\gamma_0-k)}\left(e^{2(\gamma_0-k)t}-1\right)\delta(\mathbf{r}-\mathbf{r}').$$

The long time behavior of this expression is pathological: for $k<\gamma_0$, the correlation function blows up as $t\to\infty$ while for $k>\gamma_0$ it tends to a delta function. The reason for this pathological behavior is that the dynamics actually never reaches steady state for fixed Eulerian coordinates due to the fact that early fluctuations that are delta correlated in space never have time to reach any finite distance in Eulerian coordinates even if $t\to\infty$.

Therefore, we need to consider a small correlation length for the noise to regularize the growth as we did in Chapter 4. In Lagrangian coordinates, the noise correlator now becomes $\langle \xi(\mathbf{R},t)\xi(\mathbf{R}',t')\rangle = De^{-\frac{\bar{G}(t)^2(\mathbf{R}-\mathbf{R}')^2}{a^2}}\delta(t-t')/\pi a^2$, where a is a small length scale for correlations. Eq. B.7 now yields

$$\frac{1}{\rho_0^2}\langle \delta\rho(\mathbf{R},t)\delta\rho(\mathbf{R}',t)\rangle = \frac{D'}{\pi a^2}\ e^{-2kt}\int_0^t \mathrm{d}t_1 e^{-\frac{(\mathbf{R}-\mathbf{R}')^2}{a^2}} e^{2\gamma_0 t_1} e^{2kt_1},$$

or in Eulerian coordinates

$$\frac{1}{\rho_0^2}\langle \delta\rho(\mathbf{r},t)\delta\rho(\mathbf{r}',t)\rangle = \frac{D'}{\pi a^2}\ \int_0^t \mathrm{d}t_1 e^{-\frac{(\mathbf{r}-\mathbf{r}')^2}{a^2}} e^{-2\gamma_0(t-t_1)} e^{-2k(t-t_1)}.$$

With the change of variable $u = e^{-2\gamma_0(t-t_1)}$ and setting $r' = 0$ without loss of generality, we can see that for $t \to \infty$ (i.e. in steady state), the integral simplifies to $\int_0^1 \mathrm{d}u\, u^{k/\gamma_0 - 1} e^{-r^2 u/a^2}$, which is in fact the integral representation of the lower incomplete gamma function defined as $\gamma(s,x) = \int_0^x u^{s-1}e^{-u}\mathrm{d}u$. The full expression for the density-density correlation function is

$$\frac{1}{\rho_0^2}\langle \delta\rho(\mathbf{r},t)\delta\rho(\mathbf{0},t)\rangle_{t\to\infty} = \frac{D'}{(2\gamma_0)\pi a^2}\,\gamma\left(k/\gamma_0, (r/a)^2\right)\,\left(\frac{r}{a}\right)^{\frac{-2k}{\gamma_0}} \xrightarrow{r\gg a} \frac{D'}{(2\gamma_0)\pi a^2}\,\Gamma\left(\frac{k}{\gamma_0}\right)\,\left(\frac{r}{a}\right)^{\frac{-2k}{\gamma_0}}, \tag{B.8}$$

where we have used the fact that for $r \gg a$, $\gamma\left(k/\gamma_0, (r/a)^2\right)$ tends to $\Gamma\left(k/\gamma_0\right)$. Compare this to Eq. 4.7 in Chapter 4.

We can also estimate the prefactor. Firstly, we expect the tissue to behave similarly under bulk and shear strains so that $\mu^2/(\lambda+2\mu)^2$ is of order 1 and $D' \sim D$. For the purposes of a first estimate, we assume that cells divide independently according to a Poisson process and that they instantaneously double their size upon division. Each division then contributes a fixed area of order $\pi a^2/2$ to the tissue. It is a standard result (e.g. [162]) that this discretized, Poissonian growth process can be approximated by a Langevin equation with noise strength $D = (2\gamma_0)\pi a^2/8$. We emphasize that this is only a very rough estimate for the prefactor because in reality, divisions are not perfectly random, and cells add mass throughout the cell cycle rather than only at the moment of division. With this in mind, our estimate for the prefactor is

$$\frac{D'}{(2\gamma_0)\pi a^2}\,\Gamma\left(\frac{k}{\gamma_0}\right) \sim \frac{1}{8}\Gamma\left(k/\gamma_0\right).$$

For $k \sim \gamma_0$, $\Gamma\left(k/\gamma_0\right) \sim 1$, while for $k \ll \gamma_0$ or $k \gg \gamma_0$, $\Gamma\left(k/\gamma_0\right) \to \infty$. We note, however, that for the case of $k \gg \gamma_0$ (strong feedback), the expression of Eq. B.8 as a whole tends to zero, which is expected from a strong feedback.

Finally, we consider density-density time correlations, i.e., correlation between a point initially at $\mathbf{R}$ and itself at a later time τ. This means that in Eulerian coordinates, we are looking at two different points, i.e. $(\mathbf{r},t)$ and $(\mathbf{r}',t+\tau)$, such that both points originate from $(\mathbf{R},0)$. We show that this correlator decays exponentially in time as expected from the negative feedback. Taking $t' = t+\tau$, we can see that

$$\frac{1}{\rho_0^2}\langle \delta\rho(\mathbf{R},t)\delta\rho(\mathbf{R},t+\tau)\rangle = \frac{D'}{\pi a^2}\,e^{-k\tau}\int_0^t \mathrm{d}t_1 e^{2k(t_1-t)} = \frac{D'}{(2k)\pi a^2}\,e^{-k\tau}\left(1-e^{-2kt}\right).$$

Again, we are interested in long time behavior ($t \gg k^{-1}$), which shows exponential decay, $\langle \delta\rho(\mathbf{R},t)\delta\rho(\mathbf{R},t+\tau)\rangle \sim e^{-k\tau}$; using the same estimate for D' as in the previous paragraph, we find that the prefactor is roughly $\gamma_0/8k$.

B.6 Laplacian Feedback

In Chapter 4 and above, we only considered mechanical feedbacks proportional to stress. However, in principle, spatial derivatives of stress could also feed back on the growth. Continuing to work to linear order in the stress, the lowest order term allowed by symmetry in a gradient expansion is the Laplacian of the stress. We show here that this term has the effect of regularizing the model's short distance behavior so that the correlation functions are well-behaved in the limit that the noise is delta-function correlated in space. In particular, we explicitly calculate the density-density correlation functions for isotropic growth and find that they exhibit the same power law behavior at large distances as we found in Chapter 4 without the Laplacian feedback but with noise that is colored in space. Because cells most naturally measure local stress differences in the current state of the tissue, not with respect to the initial state, the Laplacian should be taken with respect to the Eulerian coordinates. Eq. 4.6 must then be modified to read

$$\partial_t \delta\rho(\mathbf{R},t) = -k_1\delta\rho + k_2\nabla^2_{\mathbf{r}}\delta\rho + \rho_0\frac{\mu}{\lambda+2\mu}\xi(\mathbf{R},t), \tag{B.9}$$

where k_2 is the strength of Laplacian feedback, and the noise is chosen to be delta correlated in time and space, i.e. $\langle\xi(\mathbf{r},t)\xi(\mathbf{r}',t')\rangle = D\ \delta(t-t')\ \delta(\mathbf{r}-\mathbf{r}')$ or in Lagrangian coordinates $\langle\xi(\mathbf{R},t)\xi(\mathbf{R}',t')\rangle = D\ \delta(t-t')\ \delta(\mathbf{R}-\mathbf{R}')/\bar{G}^2$, as before. Note that $k_2 > 0$ otherwise the dynamics would not be stable. To leading order in $\delta\rho$, we can approximate $\nabla^2_{\mathbf{r}}\delta\rho \approx \nabla^2_{\mathbf{R}}\delta\rho/\bar{G}^2$ because $\delta\rho$ is of the same order as $\mathbf{w}/\bar{G}$.

To solve Eq. B.9 we go to Fourier space, using the convention

$$f(\mathbf{Q},t) = \int \mathrm{d}\mathbf{R}\ e^{-i\mathbf{Q}.\mathbf{R}} f(\mathbf{R},t)\ ,$$

and define a particular solution

$$\delta\rho^{(p)}(\mathbf{Q},t) = e^{-k_1 t}\ e^{\frac{k_2 Q^2}{2\gamma_0\bar{G}(t)^2}}\ e^{-\frac{k_2 Q^2}{2\gamma_0}}.$$

Then, it is easy to see that the full solution of Eq. B.9 in Fourier space is

$$\delta\rho(\mathbf{Q},t) = \rho_0\frac{\mu}{\lambda+2\mu}\ \delta\rho^{(p)}(\mathbf{Q},t)\int_0^t \frac{\xi(\mathbf{Q},t_1)}{\delta\rho^{(p)}(\mathbf{Q},t_1)}\mathrm{d}t_1$$

with $\langle\xi(\mathbf{Q},t)\xi(\mathbf{Q}',t')\rangle = (2\pi)^2 D\ \delta(t-t')\ \delta(\mathbf{Q}+\mathbf{Q}')/\bar{G}^2$. We can then find $\langle\delta\rho(\mathbf{Q},t)\delta\rho(\mathbf{Q}',t)\rangle$. We are interested to find $\langle\delta\rho(\mathbf{r},t)\delta\rho(\mathbf{0},t)\rangle_{t\to\infty}$, but we need to be careful about when to take

the limit $t \to \infty$. We proceed as follows: First, we take the inverse Fourier transform to find $\langle \delta\rho(\mathbf{R},t)\delta\rho(\mathbf{R}',t)\rangle$, then make the change $\mathbf{R} = \mathbf{r}/\bar{G}(t)$ and $\mathbf{R}' = \mathbf{r}'/\bar{G}(t)$ to arrive at

$$\frac{1}{\rho_0^2}\langle \delta\rho(\mathbf{r},t)\delta\rho(\mathbf{r}',t)\rangle = \frac{D'}{(2\pi)^2}\int_0^t \frac{\mathrm{d}t_1}{\bar{G}(t_1)^2} e^{-2k_1(t-t_1)} \int \mathrm{d}\mathbf{Q}\; e^{\frac{i\mathbf{Q}.(\mathbf{r}-\mathbf{r}')}{\bar{G}(t)}}\; e^{\frac{k_2}{\gamma_0}\left(\frac{1}{\bar{G}(t)^2}-\frac{1}{\bar{G}(t_1)^2}\right)Q^2}.$$

Here, it is easier to take the Q integral first. Also setting $\mathbf{r}' = 0$ we find

$$\frac{1}{\rho_0^2}\langle \delta\rho(\mathbf{r},t)\delta\rho(\mathbf{0},t)\rangle = \frac{D'\;\gamma_0}{4\pi k_2}\int_0^t \mathrm{d}t_1\; e^{-2k_1(t-t_1)} \frac{e^{-\frac{r^2}{\frac{4k_2}{\gamma_0}\left(\frac{\bar{G}(t)^2}{\bar{G}(t_1)^2}-1\right)}}}{\bar{G}(t_1)^2\left(\frac{1}{\bar{G}(t_1)^2}-\frac{1}{\bar{G}(t)^2}\right)}.$$

With the change of variable $t_2 = t - t_1$, we eliminate any explicit dependence on t in the integrand, allowing us to easily take the limit $t \to \infty$ in the limits of integration. The resulting integral is

$$\frac{1}{\rho_0^2}\langle \delta\rho(\mathbf{r},t)\delta\rho(\mathbf{0},t)\rangle_{t\to\infty} = \frac{D'\;\gamma_0}{4\pi k_2}\int_0^\infty \mathrm{d}t_2\; e^{-2k_1 t_2}\frac{e^{2\gamma_0 t_2}}{e^{2\gamma_0 t_2}-1}\; e^{-\frac{r^2}{\frac{4k_2}{\gamma_0}\left(e^{2\gamma_0 t_2}-1\right)}}.$$

With a final change of variable $y = 1/(e^{2\gamma_0 t_2}-1)$, we arrive at

$$\frac{1}{\rho_0^2}\langle \delta\rho(\mathbf{r},t)\delta\rho(\mathbf{0},t)\rangle_{t\to\infty} = \frac{D'}{8\pi k_2}\int_0^\infty \mathrm{d}y\; y^{\frac{k_1}{\gamma_0}-1}(1+y)^{-\frac{k_1}{\gamma_0}}\; e^{-\frac{\gamma_0\, r^2}{4k_2}y},$$

which is the integral representation of the so-called confluent hypergeometric function of the second kind defined as $U(a,b,x) = 1/\Gamma(a)\int_0^\infty \mathrm{d}y\; y^{a-1}(1+y)^{b-a-1}\; e^{-xy}$ with the asymptotic behavior $\lim_{x\to\infty} U(a,b,x) \sim x^{-a}[1+\mathcal{O}(1/x)]$ [171]. Defining $a^2 := 4k_2/\gamma_0$, we get

$$\frac{1}{\rho_0^2}\langle \delta\rho(\mathbf{r},t)\delta\rho(\mathbf{0},t)\rangle_{t\to\infty} = \frac{D'}{(2\gamma_0)\pi a^2}\;\Gamma\left(\frac{k_1}{\gamma_0}\right)\; U\left(\frac{k_1}{\gamma_0},1,\left(\frac{r}{a}\right)^2\right). \tag{B.10}$$

For $r \gg a$, using the asymptotic form of $U(a,b,x)$, we arrive at the same power law as in Eq. B.8:

$$\frac{1}{\rho_0^2}\langle \delta\rho(\mathbf{r},t)\delta\rho(\mathbf{0},t)\rangle_{\substack{t\to\infty \\ r\gg a}} = \frac{D'}{(2\gamma_0)\pi a^2}\;\Gamma\left(\frac{k_1}{\gamma_0}\right)\;\left(\frac{r}{a}\right)^{\frac{-2k_1}{\gamma_0}}.$$

As we can see, in this case, the length scale $a = \sqrt{4k_2/\gamma_0}$ was determined by the Laplacian feedback strength instead of by a correlation length for the noise. This length scale could span several cells depending on how strong the feedback is relative to the average growth rate γ_0. The power law then is regulated purely by k_1/γ_0 as before. In other words, the role of the Laplacian feedback is to provide a length scale for the early fluctuations to be carried

over the tissue as it dilates. We note that the Laplacian feedback with delta correlated noise is only valid for separations greater than cell size: for large distances, we can take the limit of cell size $\to 0$ and use a delta correlated noise, with Laplacian feedback providing a correlation length $\sqrt{4k_2/\gamma_0}$ for the dynamics; however, for distances close to a cell size, we cannot assume a delta correlated noise anymore and need to have the colored noise as before to regularize the correlations. This is evident by noticing that $U(a, b, x)$ blows up like $\log 1/x$ as $x \to 0$ meaning that without a cut off density-density correlations diverge for $r \to 0$ which is nonphysical.

Fig. B.1 compares the density-density correlation function with Laplacian feedback and without ($k_2 = 0$). As can be seen, both follow a power law for large r/a, but the Laplacian feedback has a slower convergence to the power law. This plot assumes that both cases have the same length scale a, while the source of this length scale is very different: for the Laplacian feedback, it is given by the strength of the feedback, whereas for $k_2 = 0$ it comes from having a colored noise in space.

B.7 Generalization of Isotropic Growth to d dimensions

It is fairly straightforward to generalize the results for density-density correlation to d dimensions. In this section, we will introduce quantities with subscript d (e.g. k_d), which are the d dimensional version of quantities that we have defined before; subscript d should not be confused with superscript (d) that stands for deviatoric and is reserved for traceless tensors or scalars associated with such tensors (e.g. $k^{(d)}$).

Here, we show that the power-law behavior derived in Chapter 4 (Eq. 4.7) and in the Laplacian Feedback section above still hold in arbitrary d dimensions. Writing $\widetilde{G}_{ij} = \widetilde{G}\,\delta_{ij}$, we find from Eq. 4.2 that

$$w_{ll} = \frac{d\lambda + 2\mu}{\lambda + 2\mu}\widetilde{G}.$$

Then from Eq. 4.5, we have

$$\delta\rho = \rho_0 \left(\frac{2(d-1)\mu}{\lambda + 2\mu}\right) \frac{\widetilde{G}}{\bar{\widetilde{G}}}.$$

Eq. 4.4 in d dimensions looks like

$$\partial_t \left[\frac{\widetilde{G}_{ij}}{\bar{\widetilde{G}}}\right] = c\ \sigma_{ll}\ \frac{\delta_{ij}}{d} + c^{(d)}\sigma_{ij}^{(d)} + \xi_{ij}(\mathbf{R}, t),$$

and so for isotropic growth in d dimensions we get

$$d\,\partial_t \begin{bmatrix} \widetilde{G} \\ \overline{\bar{G}} \end{bmatrix} = c\ \sigma_{ll} + \xi(\mathbf{R}, t),$$

where $\xi(\mathbf{R}, t) = \xi_{ll}(\mathbf{R}, t)$. Therefore, the dynamics of $\delta\rho$ will be

$$\partial_t \delta\rho = -k_d \delta\rho + \rho_0 \frac{2(d-1)\mu}{d(\lambda + 2\mu)} \xi(\mathbf{R}, t), \tag{B.11}$$

where $k_d = 2(d-1)\mu(d\lambda + 2\mu)c/(d\lambda + 2d\mu)$. For $d = 2$, we recover Eq. 4.6. To solve Eq. B.11 and find the density-density correlator, we first need to rewrite the noise correlator in d dimension (and remember that we are in the case of no Laplacian feedback and so need to use a colored noise): $\langle \xi(\mathbf{R}, t)\xi(\mathbf{R}', t')\rangle = D_d\, e^{-\frac{\bar{G}(t)^2(\mathbf{R}-\mathbf{R}')^2}{a^2}} \delta(t - t')/(\pi a^2)^{d/2}$. After some straightforward algebra (see Section 4.4.1), we find:

$$\begin{aligned} \frac{1}{\rho_0^2}\langle \delta\rho(\mathbf{r}, t)\delta\rho(\mathbf{0}, t)\rangle_{t\to\infty} &= \frac{D'_d}{(2\gamma_0)(\pi a^2)^{d/2}}\ \gamma\left(k_d/\gamma_0, (r/a)^2\right)\ \left(\frac{r}{a}\right)^{\frac{-2k_d}{\gamma_0}} \\ &\xrightarrow{r\gg a} \frac{D'_d}{(2\gamma_0)(\pi a^2)^{d/2}}\ \Gamma\left(\frac{k_d}{\gamma_0}\right)\ \left(\frac{r}{a}\right)^{\frac{-2k_d}{\gamma_0}}, \end{aligned} \tag{B.12}$$

with $D'_d = [2(d-1)\mu/(d\lambda + 2d\mu)]^2\, D_d$. Comparing this with Eq. B.8, we see that the density-density correlator shows the same power-law behavior in any dimensions with d-dependent exponent and prefactors. To estimate the prefactor in this case, we follow the same argument presented in Isotropic Density-density Correlation section, namely, we estimate the noise to be due to random Poisson divisions each contributing the same d dimensional volume ΔV_d to the tissue. In particular, $D_d = \Delta V_d(d\gamma_0)/d^2$. $d\gamma_0$ comes from the fact that in a Poisson-like growth, noise is proportional square root of volumetric growth rate, which is precisely $d\gamma_0$. The factor of $1/d^2$ comes from change of variable from volumetric growth to density. ΔV_d on the other hand is assumed to be the volume of a d dimensional sphere with radius $a/\sqrt{2}$, or $\Omega_d a^d/(2^{d/2}d)$ where Ω_d is the solid angle in d dimensions. Therefore, our estimate for D_d is $D_d = \gamma_0 \Omega_d\, a^d/(d^2\, 2^{d/2})$.

Now, we show that the same power law of Eq. B.12 is achieved with Laplacian feedback and delta correlated noise in d dimensions. The differential equation for $\delta\rho$ is

$$\partial_t \delta\rho = -k_{d,1}\delta\rho + k_{d,2}\nabla^2_{\mathbf{r}}\delta\rho + \rho_0 \frac{2(d-1)\mu}{d(\lambda + 2\mu)} \xi(\mathbf{R}, t), \tag{B.13}$$

and the noise correlator is $\langle \xi(\mathbf{R}, t)\xi(\mathbf{R}', t')\rangle = D\ \delta(t - t')\ \delta(\mathbf{R} - \mathbf{R}')/\bar{G}^d$. We follow the exact

same steps we did in Laplacian Feedback section to solve Eq. B.13. The only difference is that the $\mathbf{Q}$ integrals are now d dimensional. After some algebra, we get

$$\frac{1}{\rho_0^2}\langle\delta\rho(\mathbf{r},t)\delta\rho(\mathbf{0},t)\rangle = \frac{D'_d\ \pi}{(2\pi)^d}\left(\frac{\gamma_0}{k_{d,2}}\right)^{d/2}\int_0^t \mathrm{d}t_1\ e^{-2k_{d,1}(t-t_1)}\frac{e^{-\frac{r^2}{\frac{4k_{d,2}}{\gamma_0}\left(\frac{\bar{G}(t)^2}{\bar{G}(t_1)^2}-1\right)}}}{\bar{G}(t_1)^d\left(\frac{1}{\bar{G}(t_1)^2}-\frac{1}{\bar{G}(t)^2}\right)^{d/2}}.$$

Now we eliminate the explicit t dependence with the change of variable $t_2 = t - t_1$ allowing us to take $t \to \infty$, and do another change of variable $y = 1/(e^{2\gamma_0 t_2} - 1)$ just like we did before to find

$$\frac{1}{\rho_0^2}\langle\delta\rho(\mathbf{r},t)\delta\rho(\mathbf{0},t)\rangle_{t\to\infty} = \frac{D'_d\ \pi}{(2\pi)^d(2\gamma_0)}\left(\frac{\gamma_0}{k_{d,2}}\right)^{d/2}\int_0^\infty \mathrm{d}y\ y^{\frac{k_{d,1}}{\gamma_0}-1}(1+y)^{\frac{d}{2}-\frac{k_{d,1}}{\gamma_0}-1}\ e^{-\frac{\gamma_0}{4k_{d,2}}r^2 y}.$$

In terms of $U(a,b,x)$, we have

$$\begin{aligned}\frac{1}{\rho_0^2}\langle\delta\rho(\mathbf{r},t)\delta\rho(\mathbf{0},t)\rangle_{t\to\infty} &= \frac{D'_d}{(2\gamma_0)\pi^{d-1}a^d}\ \Gamma\left(\frac{k_{d,1}}{\gamma_0}\right)\ U\left(\frac{k_{d,1}}{\gamma_0},\frac{d}{2},\left(\frac{r}{a}\right)^2\right)\\ &\xrightarrow{r\gg a} \frac{D'_d}{(2\gamma_0)\pi^{d-1}a^d}\ \Gamma\left(\frac{k_{d,1}}{\gamma_0}\right)\ \left(\frac{r}{a}\right)^{\frac{-2k_{d,1}}{\gamma_0}},\end{aligned} \tag{B.14}$$

which shows the same power law as Eq. B.10. Here $a = \sqrt{4k_{d,2}/\gamma_0}$. This concludes the extension of isotropic growth to d dimensions.

B.8 Anisotropic Growth Equations

Going back to $d = 2$, here we discuss the decomposition we used for $\widetilde{G}_{ij}$ in Fourier space (Eq. 4.10), and the derivation of the mode structure and growth equations when anisotropic growth is allowed (Eqs. 4.14–4.16).

We first find $\mathbf{w}$ in terms of $\widetilde{G}_{ij}$ from Eq. 2 in Fourier space:

$$(\lambda+2\mu)(\mathbf{Q}.\mathbf{w})\mathbf{Q} - \mu(\mathbf{Q}\times\mathbf{Q}\times\mathbf{w}) = -i[\lambda\ \widetilde{G}_{ll}\ \mathbf{Q} + 2\mu\ \mathbf{Q}.\widetilde{\mathrm{G}}], \tag{B.15}$$

where $[\mathbf{Q}.\widetilde{\mathrm{G}}]_i = Q_j\widetilde{G}_{ij}$. To solve this equation, we proposed the following decomposition, Eq. 4.10:

$$\widetilde{G}_{ij} = \widetilde{G}_{ll}\frac{\delta_{ij}}{2} + (\widetilde{G}_{\parallel}\delta_{ik} - \widetilde{G}_{\perp}\epsilon_{ik})\left[\frac{2Q_kQ_j}{Q^2} - \delta_{kj}\right].$$

Here, we have decomposed $\widetilde{G}_{ij}$ into the trace and nematic components parallel and perpen-

dicular to $\mathbf{Q}$. $\widetilde{G}_{\parallel}$ and $\widetilde{G}_{\perp}$ are Q-dependent, and the traceless symmetric tensor made with them as its basis is related to the traceless part of $\widetilde{G}_{ij}$ by a rotation in Q-space, i.e.

$$\begin{bmatrix} \widetilde{G}_{\parallel} & \widetilde{G}_{\perp} \\ \widetilde{G}_{\perp} & -\widetilde{G}_{\parallel} \end{bmatrix} = \begin{bmatrix} \cos\beta & -\sin\beta \\ \sin\beta & \cos\beta \end{bmatrix} \begin{bmatrix} \frac{1}{2}(\widetilde{G}_{11} - \widetilde{G}_{22}) & \widetilde{G}_{12} \\ \widetilde{G}_{12} & \frac{1}{2}(\widetilde{G}_{22} - \widetilde{G}_{11}) \end{bmatrix} \begin{bmatrix} \cos\beta & \sin\beta \\ -\sin\beta & \cos\beta \end{bmatrix}, \quad \text{(B.16)}$$

where $2\beta = \sin^{-1}(-2Q_1Q_2/Q^2)$. This rotation takes any tensor decomposed in this specific way to a basis without explicit Q-dependence, which will prove useful later on when deriving the growth dynamics.

The lefthand side of Eq. B.15 is already decomposed into a longitudinal term $(\mathbf{Q}.\mathbf{w})\mathbf{Q}$ and a transverse term $\mathbf{Q} \times \mathbf{Q} \times \mathbf{w}$. Therefore, with the aforementioned decomposition of $\widetilde{G}_{ij}$ we can easily find $\mathbf{w}^{\parallel}$ and $\mathbf{w}^{\perp}$ in terms of the growth tensor as we did in Eq. 4.11.

Next, we can find the stress tensor in terms of the 3 components of $\widetilde{G}_{ij}$ and then write down the dynamics for these components starting from Eq. 4.4. One can see easily that the strain tensor in terms of the growth factor is

$$w_{ij} = \frac{1}{\lambda + 2\mu} \left((\lambda + \mu)\widetilde{G}_{ll} + 2\mu\ \widetilde{G}_{\parallel} \right) \frac{Q_i Q_j}{Q^2} - \widetilde{G}_{\perp} \epsilon_{ik} \left[\frac{2Q_k Q_j}{Q^2} - \delta_{kj} \right].$$

It's immediately clear that the transverse part of w_{ij} is exactly the same as the transverse part of $\widetilde{G}_{ij}$, which means that the stress tensor $\sigma_{ij} = [\lambda(w_{ll} - \widetilde{G}_{ll})\delta_{ij} + 2\mu(w_{ij} - \widetilde{G}_{ij})]/\bar{G}$ is not going to have a transverse component. After some algebra we get

$$\sigma_{ij} = \frac{2\mu(\lambda + \mu)}{(\lambda + 2\mu)\bar{G}}\ (\widetilde{G}_{ll} - 2\widetilde{G}_{\parallel}) \left[\frac{Q_i Q_j}{Q^2} - \delta_{ij} \right].$$

Noticing that

$$\delta\rho = \frac{\rho_0}{\bar{G}}(\widetilde{G}_{ll} - w_{ll}) = \rho_0 \frac{\mu}{\lambda + 2\mu} \left(\frac{\widetilde{G}_{ll} - 2\widetilde{G}_{\parallel}}{\bar{G}} \right),$$

we can now rewrite the stress tensor above in terms of $\delta\rho$ to arrive at the expression given in Eq. 4.12.

To solve the growth dynamics equation (Eq. 4.4), we first go to Fourier space and find ODEs for $\widetilde{G}_{ll}$, $\widetilde{G}_{\parallel}$ and $\widetilde{G}_{\perp}$. To do so, it is convenient to rotate the tensors in Q-space with angle β to go to the basis where there is no explicit Q-dependence as we showed above in Eq. B.16. Note that the stress can be written as $\sigma_{ij} = \sigma_{ll}\ \delta_{ij}/2 + (\sigma_{\parallel}\delta_{ik} - \sigma_{\perp}\epsilon_{ik})(2Q_kQ_j/Q^2 - \delta_{kj})$ where $\sigma_{\parallel} = \mu(\lambda+\mu)(\widetilde{G}_{ll} - 2\widetilde{G}_{\parallel})/[(\lambda+2\mu)\bar{G}]$ and $\sigma_{\perp} = 0$ as stress has no transverse component.

Similarly, we write the noise in the same basis as

$$\xi_{ij} = \xi_{ll}\frac{\delta_{ij}}{2} + (\xi_{\parallel}\delta_{ik} - \xi_{\perp}\epsilon_{ik})\left[\frac{2Q_kQ_j}{Q^2} - \delta_{kj}\right]. \tag{B.17}$$

To find the correlators of ξ_{ll}, $\xi_{\parallel}$ and $\xi_{\perp}$, we first need to find the correlators in real space. Note that since Eq. 4.4 is a first order perturbation about an isotropic growth, we require the noise to be rotationally invariant. Therefore, if we write the noise in real space as

$$\xi_{ij} = \xi_{ll}\frac{\delta_{ij}}{2} + \xi_1\begin{bmatrix}1 & 0\\ 0 & -1\end{bmatrix} + \xi_2\begin{bmatrix}0 & 1\\ 1 & 0\end{bmatrix},$$

where ξ_{ll}, ξ_1 and ξ_2 are independent random variables, then ξ_1 and ξ_2 need to have the same variance (which could in general be different from the variance of ξ_{ll}). In other words, we have the following correlators for the noise components:

$$\begin{aligned}
\langle\xi_{ll}(\mathbf{r},t)\xi_{nn}(\mathbf{r}',t')\rangle &= D_1\frac{e^{-\frac{(\mathbf{r}-\mathbf{r}')^2}{a^2}}}{\pi a^2}\,\delta(t-t'),\\
\langle\xi_1(\mathbf{r},t)\xi_1(\mathbf{r}',t')\rangle &= D_2\frac{e^{-\frac{(\mathbf{r}-\mathbf{r}')^2}{a^2}}}{\pi a^2}\,\delta(t-t'),\\
\langle\xi_2(\mathbf{r},t)\xi_2(\mathbf{r}',t')\rangle &= D_2\frac{e^{-\frac{(\mathbf{r}-\mathbf{r}')^2}{a^2}}}{\pi a^2}\,\delta(t-t'),
\end{aligned}$$

and all cross correlations are zero. Here, we assumed for simplicity that a is the same for $\xi_{1,2}$ and ξ_{ll}, but the correlation lengths for these 3 components could be different in general.

In Q-space, the correlators will involve $\delta(\mathbf{Q}+\mathbf{Q}')$, therefore different Q's don't mix. This along with rotational invariance leads to statistical independence of ξ_{ll}, $\xi_{\parallel}$ and $\xi_{\perp}$, and we get the following correlators:

$$\begin{aligned}
\langle\xi_{ll}(\mathbf{Q},t)\xi_{nn}(\mathbf{Q}',t')\rangle &= (2\pi)^2\,D_1\frac{e^{-(\frac{aQ}{2\bar{G}})^2}}{\bar{G}^2}\,\delta(t-t')\,\delta(\mathbf{Q}+\mathbf{Q}'),\\
\langle\xi_{\parallel}(\mathbf{Q},t)\xi_{\parallel}(\mathbf{Q}',t')\rangle &= (2\pi)^2\,D_2\frac{e^{-(\frac{aQ}{2\bar{G}})^2}}{\bar{G}^2}\,\delta(t-t')\,\delta(\mathbf{Q}+\mathbf{Q}'),\\
\langle\xi_{\perp}(\mathbf{Q},t)\xi_{\perp}(\mathbf{Q}',t')\rangle &= (2\pi)^2\,D_2\frac{e^{-(\frac{aQ}{2\bar{G}})^2}}{\bar{G}^2}\,\delta(t-t')\,\delta(\mathbf{Q}+\mathbf{Q}'),
\end{aligned} \tag{B.18}$$

with all the cross correlators zero. Now that we have the noise correlators for $\xi_{\parallel}$ and $\xi_{\perp}$, we

can apply the rotation in Eq. B.16 to both sides of Eq. 4.4 and find:

$$\partial_t \begin{pmatrix} 1 \\ \bar{\widetilde{G}} \end{pmatrix} \begin{bmatrix} \frac{\widetilde{G}_{ll}}{2} + \widetilde{G}_{\parallel} & \widetilde{G}_{\perp} \\ \widetilde{G}_{\perp} & \frac{\widetilde{G}_{ll}}{2} - \widetilde{G}_{\parallel} \end{bmatrix} = -\frac{k}{2\bar{\widetilde{G}}} \begin{bmatrix} \widetilde{G}_{ll} - 2\widetilde{G}_{\parallel} & 0 \\ 0 & \widetilde{G}_{ll} - 2\widetilde{G}_{\parallel} \end{bmatrix} + \frac{k^{(d)}}{2\bar{\widetilde{G}}} \begin{bmatrix} \widetilde{G}_{ll} - 2\widetilde{G}_{\parallel} & 0 \\ 0 & -\widetilde{G}_{ll} + 2\widetilde{G}_{\parallel} \end{bmatrix} + \begin{bmatrix} \frac{\xi_{ll}}{2} + \xi_{\parallel} & \xi_{\perp} \\ \xi_{\perp} & \frac{\xi_{ll}}{2} - \xi_{\parallel} \end{bmatrix}$$

where $k = 2\mu(\lambda+\mu)c/(\lambda+2\mu)$ and $k^{(d)} = 2\mu(\lambda+\mu)c^{(d)}/(\lambda+2\mu)$. And, finally, by writing $\widetilde{G}_{ll} - 2\widetilde{G}_{\parallel}$ in terms of $\delta\rho$, we arrive at the differential equations describing the growth:

$$\begin{aligned} \partial_t\, \delta\rho &= -(k + k^{(d)})\delta\rho + \rho_0 \frac{\mu}{\lambda + 2\mu} \left(\xi_{ll} - 2\xi_{\parallel}\right), \\ \partial_t \left[\frac{\widetilde{G}_{\perp}}{\bar{\widetilde{G}}}\right] &= \xi_{\perp}, \\ \partial_t \left[\frac{\widetilde{G}_{ll} + 2\frac{k}{k^{(d)}}\widetilde{G}_{\parallel}}{\bar{\widetilde{G}}}\right] &= \xi_{ll} + 2\frac{k}{k^{(d)}}\xi_{\parallel}. \end{aligned}$$

The bottom two equations describe soft modes with diffusive dynamics. We define the amplitudes of the transverse soft mode $Z_T = \widetilde{G}_{\perp}/\bar{G}$ and the longitudinal soft mode $Z_L = [\widetilde{G}_{ll} + (2k/k^{(d)})\widetilde{G}_{\parallel}]/\bar{G}$. The interpretation of these modes is given in Chapter 4. Finally, in terms of these three amplitudes, $\widetilde{G}_{ij}$ is given by

$$\widetilde{G}_{ij} = \bar{G}\left[\frac{k^{(d)}}{k + k^{(d)}}\left(Z_L + \frac{k(\lambda+2\mu)}{k^{(d)}\mu\,\rho_0}\delta\rho\right)\frac{\delta_{ij}}{2} + \frac{k^{(d)}}{2(k+k^{(d)})}\left(Z_L - \frac{\lambda+2\mu}{\mu\,\rho_0}\delta\rho\right)\left(\frac{2Q_iQ_j}{Q^2} - \delta_{ij}\right) - Z_T\epsilon_{ik}\left(\frac{2Q_kQ_j}{Q^2} - \delta_{kj}\right)\right].$$

B.9 Clone Statistics

In this section, we derive the results for clone size and shape statistics given, for the general case of anisotropic growth, in Chapter 4 Eqs. 4.18 and 4.19. First, starting from Eq. 4.8 of Chapter 4, we derive the variance of the clone size (Eq. 4.18) and show that this variance scales with clone size when there are growth anisotropies but not in the isotropic limit. Next, we follow the same steps for clone shape starting from Eq. 4.9 to derive the scaling relation in Eq. 4.19. Finally, we discuss the correlation, or lack thereof, between the areas of two adjacent clones in our model.

B.9.1 Clone Size

To simplify Eq. 8, note that $\nabla.\mathbf{w} = w_{ll}$. In the previous section, we found w_{ll} in Q-space to be

$$w_{ll} = \frac{1}{\lambda + 2\mu}\left((\lambda+\mu)\widetilde{G}_{ll} + 2\mu\ \widetilde{G}_{\parallel}\right).$$

We rewrite this expression in terms of $\delta\rho$ and Z_L

$$w_{ll} = \bar{G}\left[\alpha_1\frac{\delta\rho}{\rho_0} + \alpha_2 Z_L\right],$$

where $\alpha_1 = [(\lambda+\mu)k - \mu k^{(d)}]/[\mu(k+k^{(d)})]$ and $\alpha_2 = k^{(d)}/(k+k^{(d)})$. As we can see, this quantity has no explicit Q dependence, so we can formally take the inverse Fourier transform of the scalars w_{ll}, $\delta\rho$, and Z_L. Although it is not easy to interpret Z_L in real space, it is nevertheless useful for us to work in real space. By expressing w_{ll} in terms of $\delta\rho$ and Z_L, now in real space, we can write $\mathrm{Var}(A)$ in Eq. 4.8 as:

$$\mathrm{Var}(A) = \bar{G}^4\int_{R,R'\le R_c}\left[\frac{\alpha_1^2}{\rho_0^2}\langle\delta\rho(\mathbf{R},t)\delta\rho(\mathbf{R}',t)\rangle + \frac{2\alpha_1\alpha_2}{\rho_0}\langle\delta\rho(\mathbf{R},t)Z_L(\mathbf{R}',t)\rangle + \alpha_2^2\langle Z_L(\mathbf{R},t)Z_L(\mathbf{R}',t)\rangle\right]\mathrm{d}\mathbf{R}\,\mathrm{d}\mathbf{R}'.$$

Note that the cross correlation term is not zero because the noises of $\delta\rho$ and Z_L are correlated (see Eqs. 4.14 and 4.16). However, as we will shortly see, the long time behavior of the integral is dominated by the Z_L autocorrelation term and the other two terms are negligible in comparison. Let us look at the three correlators one by one. For $\langle\delta\rho(\mathbf{R},t)\delta\rho(\mathbf{R}',t)\rangle$ we have

$$\frac{1}{\rho_0^2}\langle\delta\rho(\mathbf{R},t)\delta\rho(\mathbf{R}',t)\rangle =$$

$$e^{-2(k+k^{(d)})t}\frac{\mu^2}{(\lambda+2\mu)^2}\int_0^t \mathrm{d}t_1\,\mathrm{d}t_2\, e^{(k+k^{(d)})(t_1+t_2)}\left[\langle\xi_{ll}(\mathbf{R},t_1)\xi_{ll}(\mathbf{R}',t_1)\rangle + 4\langle\xi_{\parallel}(\mathbf{R},t_1)\xi_{\parallel}(\mathbf{R}',t_1)\rangle\right]$$

$$= e^{-2(k+k^{(d)})t}\frac{\mu^2}{(\lambda+2\mu)^2}\,\frac{D_1+4D_2}{\pi a^2}\int_0^t e^{-\frac{(\mathbf{R}-\mathbf{R}')^2\bar{G}(t_1)}{a^2}}\, e^{2(k+k^{(d)})t_1}\mathrm{d}t_1.$$

Notice that here we are working in fixed Lagrangian coordinates because we are only interested in points within a circular clone of Lagrangian radius R_c independent of time. This is in contrast to our calculation of $\langle\delta\rho(\mathbf{r},t)\delta\rho(\mathbf{r}',t)\rangle$ that needed to be carried out in Eulerian coordinates. One benefit of working in Lagrangian coordinates is that we can take the noise to be delta correlated in $\mathbf{r}$ (i.e. work in the $a\to 0$ limit) without introducing any pathological behavior. This simplifies the calculations, so we will take noise to be white in time and space

similar to our calculation for Laplacian feedback, i.e.

$$\begin{aligned}
\langle \xi_{ll}(\mathbf{R},t)\xi_{nn}(\mathbf{R}',t')\rangle &= \frac{D_1}{\bar{G}^2}\,\delta(t-t')\,\delta(\mathbf{R}-\mathbf{R}'),\\
\langle \xi_{\parallel}(\mathbf{R},t)\xi_{\parallel}(\mathbf{R}',t')\rangle &= \frac{D_2}{\bar{G}^2}\,\delta(t-t')\,\delta(\mathbf{R}-\mathbf{R}'),\\
\langle \xi_{\perp}(\mathbf{R},t)\xi_{\perp}(\mathbf{R}',t')\rangle &= \frac{D_2}{\bar{G}^2}\,\delta(t-t')\,\delta(\mathbf{R}-\mathbf{R}'). \qquad \text{(B.19)}
\end{aligned}$$

With this, we have

$$\frac{1}{\rho_0^2}\,\langle \delta\rho(\mathbf{R},t)\delta\rho(\mathbf{R}',t)\rangle = \frac{\mu^2}{(\lambda+2\mu)^2}\,\frac{D_1+4D_2}{2(k+k^{(d)}-\gamma_0)}\left(e^{-2\gamma_0 t}-e^{-2(k+k^{(d)})t}\right)\delta(\mathbf{R}-\mathbf{R}').$$

Similarly, for $\langle \delta\rho(\mathbf{R},t)Z_L(\mathbf{R}',t)\rangle$ we get

$$\frac{1}{\rho_0}\,\langle \delta\rho(\mathbf{R},t)Z_L(\mathbf{R}',t)\rangle = \frac{\mu}{\lambda+2\mu}\,\frac{D_1-4(k/k^{(d)})D_2}{k+k^{(d)}-2\gamma_0}\left(e^{-2\gamma_0 t}-e^{-(k+k^{(d)})t}\right)\delta(\mathbf{R}-\mathbf{R}').$$

Finally for $\langle Z_L(\mathbf{R},t)Z_L(\mathbf{R}',t)\rangle$ we find

$$\langle Z_L(\mathbf{R},t)Z_L(\mathbf{R}',t)\rangle = \frac{D_1+4(k/k^{(d)})^2 D_2}{2\gamma_0}\left(1-e^{-2\gamma_0 t}\right)\delta(\mathbf{R}-\mathbf{R}').$$

Before we go any further, we note that $\langle Z_L(\mathbf{R},t)Z_L(\mathbf{R}',t)\rangle$ does not grow linearly with time as one would naïvely expect given the apparently diffusive dynamics of Z_L. The reason is that, as Eq. B.19 makes clear, the amplitude of the noise decays with time like $1/\bar{G}^2$. This behavior, in turn, arises from the fact that the noise is defined to have constant strength in Eulerian coordinates. But a region of fixed size in Lagrangian coordinates will grow larger and larger in Eulerian coordinates as time progresses, leading overall variation in that region to go down. The growth hence puts a limit on how large the soft mode variances can get, and at long times, $\langle Z_L(\mathbf{R},t)Z_L(\mathbf{R}',t)\rangle$ approaches a constant. (There is in fact one further subtlety here: The noise correlators of the form $\langle \xi(\mathbf{R},t)\xi(\mathbf{R}',t')\rangle$ have an explicit prefactor of $1/\bar{G}^2$ only when we take the limit $a \to 0$ and convert Gaussian correlation functions in space into delta functions. In fact, for finite a, the mean-squared mode displacement at a single point $\mathbf{R}$, $\langle Z_L(\mathbf{R},t)^2\rangle$, does grow linearly in time. The integral of $\langle Z_L(\mathbf{R},t)Z_L(\mathbf{R}',t)\rangle$ over any fixed region in $\mathbf{R}$, however, still approaches a constant, just as in the limit $a \to 0$, because the range of spatial correlations in $\mathbf{R}$ decreases exponentially in time. Similarly, the noise correlations in $\mathbf{Q}$ space, Eq. B.18, always have an explicit prefactor of $1/\bar{G}^2$, even for finite a, so that the mean-squared value of of $Z_L(\mathbf{Q},t)$ remains bounded for all time.)

Now, if we compare the three correlators at long times, we see that $\langle Z_L(\mathbf{R},t)Z_L(\mathbf{R}',t)\rangle$

dominates the growth as the other two correlators decay exponentially and so can be ignored in the long time limit. In particular, with $\langle A\rangle = \bar{G}^2\pi R_c^2$, as $t\to\infty$ we can see that the ratio $\mathrm{Var}(A)/\langle A\rangle^2$ is a constant:

$$\left.\frac{\mathrm{Var}(A)}{\langle A\rangle^2}\right|_{t\to\infty} = \alpha_2^2\frac{D_1+4(k/k^{(d)})^2D_2}{(2\gamma_0)\pi R_c^2}\sim\frac{1}{R_c^2},$$

agreeing with Eq. 18. Estimating R_c to be of order of a cell radius, the ratio will be of order 1 with the same assumptions on noise strengths as above in the Isotropic Density-density Correlations section. As a final note, this scaling of variance with clone size is the direct result of having the soft mode Z_L and would not occur in isotropic growth. In that case, the only term we have is $\langle\delta\rho(\mathbf{R},t)\delta\rho(\mathbf{R}',t)\rangle$, which does not scale with size, and the ratio will decay to zero at long times.

B.9.2 Clone Shape

Now we move on to the expression for the amplitudes B_n of the modes specifying clone shape, which involves a few subtleties. For one, notice that the integral involves correlators of w_k, which was found in Q space and has explicit Q dependence. Therefore, we first need to find the correlator $\langle w_k w_j'\rangle$ in Fourier space, then take the inverse transform and finally take the Θ integrals.

We first write out the components of $\mathbf{w}$ (Eq. 4.11) in terms of the modes as we did with w_{ll} for clone size:

$$w_k(\mathbf{Q},t) = -\frac{i\,\bar{G}}{Q^2}\left[(\alpha_1\frac{\delta\rho}{\rho_0}+\alpha_2 Z_L)Q_k - 2Z_T\;\epsilon_{kl}\,Q_l\right].$$

The correlator will look like

$$\begin{aligned}\langle w_k(\mathbf{Q},t)w_j(\mathbf{Q}',t)\rangle \;=\; -\frac{\bar{G}^2}{Q^2\;Q'^2}\Bigg[&\left(\frac{\alpha_1^2}{\rho_0^2}\,\langle\delta\rho(\mathbf{Q},t)\delta\rho(\mathbf{Q}',t)\rangle + \frac{2\alpha_1\alpha_2}{\rho_0}\,\langle\delta\rho(\mathbf{Q},t)Z_L(\mathbf{Q}',t)\rangle\right.\\ &\left.+\alpha_2^2\,\langle Z_L(\mathbf{Q},t)Z_L(\mathbf{Q}',t)\rangle\right)Q_k\,Q_j' + 4\,\langle Z_T(\mathbf{Q},t)Z_T(\mathbf{Q}',t)\rangle\,\epsilon_{kl}\,\epsilon_{js}Q_l\,Q_s'\Bigg].\end{aligned}$$

Note that $\delta\rho$ and Z_L do not mix with Z_T because their respective noises are statistically independent. We use the correlators in Eq. B.19 for noise terms, of which we then take the Fourier transform to go to Q-space. The only dominant terms in $\langle w_k(\mathbf{Q},t)w_j(\mathbf{Q}',t)\rangle$ are the soft mode autocorrelations, with the other two terms involving $\delta\rho$ showing the same exponential decay in time as in the clone size calculation above. Therefore we only focus on

the two soft mode autocorrelators:

$$\begin{aligned}\langle Z_L(\mathbf{Q},t)Z_L(\mathbf{Q}',t)\rangle &= (2\pi)^2\frac{D_1+4(k/k^{(d)})^2D_2}{2\gamma_0}\ \left(1-e^{-2\gamma_0 t}\right)\delta(\mathbf{Q}+\mathbf{Q}'),\\ \langle Z_T(\mathbf{Q},t)Z_T(\mathbf{Q}',t)\rangle &= (2\pi)^2\frac{D_2}{2\gamma_0}\ \left(1-e^{-2\gamma_0 t}\right)\delta(\mathbf{Q}+\mathbf{Q}'),\end{aligned}$$

and

$$\langle w_k(\mathbf{Q},t)w_j(\mathbf{Q}',t)\rangle_{t\to\infty}\approx -(2\pi)^2\frac{\bar{G}^2}{Q^4}\left[\alpha_2^2\frac{D_1+4(k/k^{(d)})^2D_2}{2\gamma_0}\ Q_k\,Q'_j+\frac{2D_2}{\gamma_0}\ \epsilon_{kl}\,\epsilon_{js}Q_l\,Q'_s\right]\times\left(1-e^{-2\gamma_0 t}\right)\delta(\mathbf{Q}+\mathbf{Q}').$$

Now we need to take the inverse Fourier transform before evaluating the integral in Eq. 4.9. We are basically taking the inverse transform of something like Q_kQ_j/Q^4:

$$\begin{aligned}\frac{1}{(2\pi)^4}\int \mathrm{d}\mathbf{Q}\,\mathrm{d}\mathbf{Q}'\frac{Q_k\,Q'_j}{Q^4}e^{i(\mathbf{Q}.\mathbf{R}+\mathbf{Q}'.\mathbf{R}')}\delta(\mathbf{Q}+\mathbf{Q}') &= -\frac{1}{(2\pi)^4}\int \mathrm{d}\mathbf{Q}\,\frac{Q_k\,Q_j}{Q^4}e^{i\mathbf{Q}.(\mathbf{R}-\mathbf{R}')}\\ &= \frac{\partial_{R_k}\partial_{R_j}}{(2\pi)^4}\int \mathrm{d}\mathbf{Q}\,\frac{e^{i\mathbf{Q}.(\mathbf{R}-\mathbf{R}')}}{Q^4}.\end{aligned}$$

The inverse transform of $1/Q^4$ is known from the theory of generalized functions [172] to be

$$\int \mathrm{d}\mathbf{Q}\,\frac{e^{i\mathbf{Q}.(\mathbf{R}-\mathbf{R}')}}{Q^4}=-\frac{\pi}{2}\big\{(1-\gamma+\log 2)(\mathbf{R}-\mathbf{R}')^2-(\mathbf{R}-\mathbf{R}')^2\log|\mathbf{R}-\mathbf{R}'|\big\},$$

where γ is the Euler's constant and not to be confused with the growth rate γ_0. The $\log R$ term is allowed by dimensional analysis and turns out to be part of the solution. There is an ambiguity in the scale l in $\log(R/l)$ but it will not affect the final result.

Taking the double derivative of the integral, we get

$$I_{kj}=\partial_{R_k}\partial_{R_j}\int \mathrm{d}\mathbf{Q}\,\frac{e^{i\mathbf{Q}.(\mathbf{R}-\mathbf{R}')}}{Q^4}=\pi\big\{(\gamma-\frac{1}{2}-\log 2)\delta_{kj}+\frac{(R_j-R'_j)(R_k-R'_k)}{(\mathbf{R}-\mathbf{R}')^2}+\log|\mathbf{R}-\mathbf{R}'|\delta_{kj}\big\}.$$

Now, we just need to put these pieces together to find

$$\langle w_k(\mathbf{R},t)w_j(\mathbf{R}',t)\rangle_{t\to\infty}\approx -\frac{\bar{G}^2}{4\pi\gamma_0}\left[\alpha_2^2\frac{D_1+4(k/k^{(d)})^2D_2}{2}\ I_{kj}+2D_2\ \epsilon_{kl}\,\epsilon_{js}\,I_{ls}\right]\left(1-e^{-2\gamma_0 t}\right),$$

which we then plug into

$$\left\langle |B_n|^2 \right\rangle = \frac{1}{(2\pi)^2} \int_0^{2\pi} \mathrm{d}\Theta \mathrm{d}\Theta' \hat{R}_k(\Theta) \hat{R}_j(\Theta') \langle w_k w_j' \rangle e^{-in(\Theta-\Theta')}.$$

The only nonzero term in this integral is given by the $\log|\mathbf{R}-\mathbf{R}'|$ term in I_{kj} and I_{ls}. The integral becomes

$$\begin{aligned}\left\langle |B_n|^2 \right\rangle_{t\to\infty} \approx & -\frac{\bar{G}^2}{(4\pi)^2\gamma_0}\left[\alpha_2^2 \frac{D_1 + 4(k/k^{(d)})^2 D_2}{2} + 2D_2\right]\left(1 - e^{-2\gamma_0 t}\right) \\ & \times \int_0^{2\pi} \mathrm{d}\Theta\, \mathrm{d}\Theta' (\cos\Theta\cos\Theta' + \sin\Theta\sin\Theta') \log|\mathbf{R}-\mathbf{R}'| e^{-in(\Theta-\Theta')}.\end{aligned}$$

The final integral was evaluated to be $-2n\pi^2/(n^2-1)$ (for $n>1$). With $B_0 = \bar{G}R_c$, we can see that in the limit of $t\to\infty$ we get

$$\left.\frac{\langle |B_n|^2\rangle}{B_0^2}\right|_{t\to\infty} = \left[\alpha_2^2 \frac{D_1 + 4(k/k^{(d)})^2 D_2}{4\gamma_0\, R_c^2} + \frac{D_2}{\gamma_0\, R_c^2}\right]\frac{n}{4(n^2-1)} \sim \frac{1}{R_c^2}\frac{n}{n^2-1},$$

In agreement with Eq. 19. Again, assuming R_c is approximately of order of a cell size, the quantity in square brackets will be of order 1. Similar to the clone size, this scaling relation is purely a result of the soft modes. Here, in contrast to the clone size variance, the transverse soft mode is also involved. This is because w_k , which was the important variable here, depends on both soft modes whereas in the case of clone size the important variable is w_{ll} which depends on only the longitudinal soft mode.

B.9.3 Independence of Adjacent Clone Areas

In this subsection, we discuss the correlation between adjacent clones. We claimed in Chapter 4 at the end of Section 4.4 that the areas of adjacent clones are uncorrelated in our model. This may sound counterintuitive, especially knowing that due to soft modes, boundaries of clones are soft, which could lead us to expect that one clone can grow at the expense of an adjacent clone. We show here that this in fact is not the case.

To understand the statistical independence of clone areas, it is useful first to consider the simpler situation where we have only a delta-like instantaneous growth at the origin with strength ν, i.e. $G_{ij}(\mathbf{R},0) = (1+\nu\,\delta(\mathbf{R}))\delta_{ij}$. (Here, $\bar{G}=1$.) From Eq. 4.2 in Chapter 4, we can find

$$\mathbf{w}(\mathbf{R},0) = \frac{2\nu(\lambda+\mu)}{\lambda+2\mu}\frac{\mathbf{R}}{R^2},$$

which implies a purely deviatoric strain field except at the origin [122] and thus a localized change in density

$$\delta\rho(\mathbf{R},0) = \rho_0[\widetilde{G}_{ll}(\mathbf{R},0) - w_{ll}(\mathbf{R},0)] = \frac{2\mu\rho_0}{\lambda+2\mu}\nu\delta(\mathbf{R}).$$

This bump in the density induces mechanical feedback, leading to density relaxation. More precisely, the dynamics given by Eqs. 4.14–4.16 in Chapter 4 but without noise ($\xi_{ij} = 0$), together with Eq. 4.13 and the initial conditions $\widetilde{G}_{ll}(\mathbf{R},0) = 2\nu\delta(\mathbf{R})$, $\widetilde{G}_{\parallel}(\mathbf{R},0) = \widetilde{G}_{\perp}(\mathbf{R},0) = 0$ allow us to find the growth tensor and the density at time t (note that because there is no explicit Q dependence in Eqs. 4.14–4.16, we can formally take the inverse Fourier transform and work in real space):

$$\begin{aligned}
\widetilde{G}_{ll}(\mathbf{R},t) &= \frac{k^{(d)}}{k+k^{(d)}}2\nu\left(1+\frac{k}{k^{(d)}}e^{-(k+k^{(d)})t}\right)\delta(\mathbf{R}) \\
\widetilde{G}_{\parallel}(\mathbf{R},t) &= \frac{k^{(d)}}{k+k^{(d)}}\nu\left(1-e^{-(k+k^{(d)})t}\right)\delta(\mathbf{R}) \\
\widetilde{G}_{\perp}(\mathbf{R},t) &= 0 \\
\delta\rho(\mathbf{R},t) &= \frac{2\mu\rho_0}{\lambda+2\mu}\nu e^{-(k+k^{(d)})t}\,\delta(\mathbf{R}).
\end{aligned}$$

Now, from Eq. 4.11, we can easily see that $\mathbf{w}(\mathbf{R},t) \sim \mathbf{R}/R^2$ stays divergence free ($\nabla.\mathbf{w} \sim \delta(\mathbf{R})$). Therefore, since $\Delta A = \int \nabla.\mathbf{w}\,\mathrm{d}\mathbf{R}$, any region of the tissue that does not contain the origin will not see any increase in area. In other words, if we have two adjacent clones and introduce a small amount of incremental growth at the origin, only the area of the clone containing the origin will increase; the size of the other will be unchanged, though its shape will be distorted (see Fig. 4.2A in Chapter 4). This implies that the areas of any two clones are uncorrelated. There is an additional subtlety worth mentioning: While $\widetilde{G}_{ll}(\mathbf{R},t)$ and $\widetilde{G}_{\parallel}(\mathbf{R},t)$ remain local, $\widetilde{G}_{ij}(\mathbf{R},t)$ in general is not localized to the origin. This is due to the fact that $\widetilde{G}_{\parallel}$ lives in Fourier space and does not have a well-defined physical meaning in real space. To see the non-locality of $\widetilde{G}_{ij}(\mathbf{R},t)$, we start from Eq. 4.10, noticing that $\widetilde{G}_{\parallel}$ is flat in Fourier space and thus, $\widetilde{G}_{ij}(\mathbf{Q},t)$ is Q-dependent and not local in real space. For instance, $\widetilde{G}_{12}(\mathbf{Q},t) \propto Q_1Q_2/Q^2$ which yields $\widetilde{G}_{12}(\mathbf{R},t) \propto R_1R_2/R^4$. Nonetheless, since $\nabla.\mathbf{w}$ is localized to the origin (at least in the absence of effects from boundary conditions that we neglect throughout this paper), clone areas remain uncorrelated.

Returning to our full calculation with arbitrary growth tensor G, we can explicitly see this decoupling if we take two adjacent clones of sizes A_1 and A_2 and look at $\langle\Delta A_1\Delta A_2\rangle$. We define $\Delta A_k = \bar{G}\int_{\mathbf{R}_k\in\text{clone k}} \nabla_k.\mathbf{w}_k\,\mathrm{d}\mathbf{R}_k$ with $k = 1,2$, $\mathbf{w}_k = \mathbf{w}(\mathbf{R}_k)$ and $\nabla_k = \nabla_{\mathbf{R}_k}$. Then,

the correlation of clone 1 and 2 will be

$$\langle \Delta A_1 \Delta A_2 \rangle = \bar{G}^2 \int \langle \nabla_1 . \mathbf{w}_1 \ \nabla_2 . \mathbf{w}_2 \rangle \ \mathrm{d}\mathbf{R_1} \mathrm{d}\mathbf{R_2}$$

This quantity involves noise correlators $\langle \xi_{ll}(\mathbf{R}_1, t)\xi_{ll}(\mathbf{R}_2, t)\rangle$ and $\langle \xi_{\parallel}(\mathbf{R}_1, t)\xi_{\parallel}(\mathbf{R}_2, t)\rangle$ that give $\delta(\mathbf{R}_1 - \mathbf{R}_2)$, and because we are integrating over two separate regions, the integral is zero as claimed in Chapter 4. We note that if instead of delta correlated noise, we consider colored noise with a small width a, within our continuum model clones that actually share a boundary must show small but nonzero area correlation because the correlations in the noise stretch across the boundary: $\langle \Delta A_1 \Delta A_2 \rangle \sim \mathcal{O}(L^2 a^2)$ where L is the length of the shared boundary. However, in reality, the interface is where the cells of clone 1 meet the cells of clone 2, and assuming independent divisions of discrete cells, there is no correlation between noise in clone 1 and 2 and $\langle \Delta A_1 \Delta A_2 \rangle$ will again be zero.

B.10 The Limit of No Net Growth

Here, we derive expressions for fluctuations in density and velocity in the limit of no net growth ($\gamma_0 = 0$ or $\bar{G} = 1$) and show that in this limit, our model is equivalent to the fluctuating homeostatic tissue described in Ranft et al. [6]. In particular, we will derive expressions of the same form as Eqs. 21 and 22 in [6], which related the Fourier transformed (in space and time) density and velocity fluctuations $\delta\rho(\mathbf{q}, \omega)$ and $\mathbf{v}(\mathbf{q}, \omega)$ to appropriate noise terms.

Since we are interested in fluctuations about the steady state of no growth, the distinction between Lagrangian and Eulerian coordinates vanishes to linear order in small quantities, so we will use lower-case $\mathbf{q}$ to denote the wavevector for consistency with [6].

Starting from Eq. 4.14 of Chapter 4 and Fourier transforming in time, we get

$$\left(-i\omega + \frac{2\mu(\lambda + \mu)}{\lambda + 2\mu}(c + c^{(d)}) \right) \delta\rho = \rho_0 \frac{\mu}{\lambda + 2\mu}(\xi_{ll} - 2\xi_{\parallel}).$$

Now, writing $\lambda + \mu = \chi$, $1/c = 2\chi\tau$ and $1/c^{(d)} = 2\mu\tau_a$, and also noting that the traceless part of the noise tensor $\xi_{ij}^{(d)} = \xi_{ij} - \xi_{ll}\delta_{ij}/2$ is related to $\xi_{\parallel}$ via $\xi_{\parallel} = q_i \xi_{ij}^{(d)} q_j / q^2$ (Eq. B.17), we arrive at an expression of the same form as Eq. 21 in [6]:

$$\delta\rho = \frac{\tau\, \rho_0 (\tau_a \mu)}{(1 - i\omega\tau_a)\tau\chi + (1 - i\omega\tau)\tau_a\mu} \left[\xi_{ll} - 2\frac{q_i \xi_{ij}^{(d)} q_j}{q^2} \right]. \tag{B.20}$$

We note that the extra factors of 4/3 in [6] appear because their calculation was carried

out in 3d. The prefactor to $\xi_{ij}^{(d)}$ is also different here from [6] because we have defined the noise to be acting on the growth tensor (see Eq. B.3), whereas Ranft et al. have the traceless noise act directly on the traceless stress tensor.

We now find the velocity fluctuations. We have

$$v_k(\mathbf{q},t) = \partial_t w_k(\mathbf{q},t) = -\frac{i}{q^2}\left[(\alpha_1\,\partial_t\frac{\delta\rho}{\rho_0} + \alpha_2\,\partial_t Z_L)q_k - 2\,\partial_t Z_T\;\epsilon_{kl}\,q_l\right].$$

Denoting the component of velocity parallel to $\mathbf{q}$ as $v^{\parallel} = v_l q_l/q$, we find

$$iq\,v^{\parallel} = \alpha_1\left[-\frac{2\mu\chi}{\chi+\mu}\left(\frac{1}{2\tau\chi}+\frac{1}{2\tau_a\mu}\right)\frac{\delta\rho}{\rho_0} + \frac{\mu}{\chi+\mu}\left(\xi_{ll} - 2\frac{q_i\xi_{ij}^{(d)}q_j}{q^2}\right)\right] + \alpha_2\left(\xi_{ll} + 2\frac{\tau_a\mu}{\tau\chi}\,\frac{q_i\xi_{ij}^{(d)}q_j}{q^2}\right),$$

where, in terms of τ and τ_a, $\alpha_1 = (\tau_a - \tau)\chi/(\tau\chi + \tau_a\mu)$ and $\alpha_2 = \tau\chi/(\tau\chi+\tau_a\mu)$. Using the expression for $\delta\rho$ in Eq. B.20 and after some manipulation, we arrive at the following (compare with $v_{\parallel}$ in Eq. 22 of [6])

$$iq\,v^{\parallel} = \frac{1}{(1-i\omega\tau_a)\tau\chi + (1-i\omega\tau)\tau_a\mu}\left[\tau\chi(1-i\omega\tau_a)\xi_{ll} + \tau_a\mu(1-i\omega\tau)2\frac{q_i\xi_{ij}^{(d)}q_j}{q^2}\right]. \quad \text{(B.21)}$$

Finally, we have, for the component of velocity perpendicular to $\mathbf{q}$

$$v_k^{\perp} = \partial_t w_k^{\perp} = 2i\epsilon_{kl}\frac{q_l}{q^2}\xi_{\perp}.$$

It is easy to see that $\xi_{\perp}$ is related to $\xi_{ij}^{(d)}$ by $\epsilon_{kl}q_l\xi_{\perp} = q_k q_m \xi_{mj}^{(d)} q_j/q^2 - \xi_{kj}^{(d)}q_j$. Plugging this in, we obtain

$$v_k^{\perp} = \frac{2i}{q^2}(q_k q_m \xi_{mj}^{(d)} q_j/q^2 - \xi_{kj}^{(d)}q_j). \quad \text{(B.22)}$$

Comparing B.22 to Eq. 22 in [6], we see that they again only differ by prefactors that can be absorbed in the noise strength by redefinition of $\xi_{\perp}$.

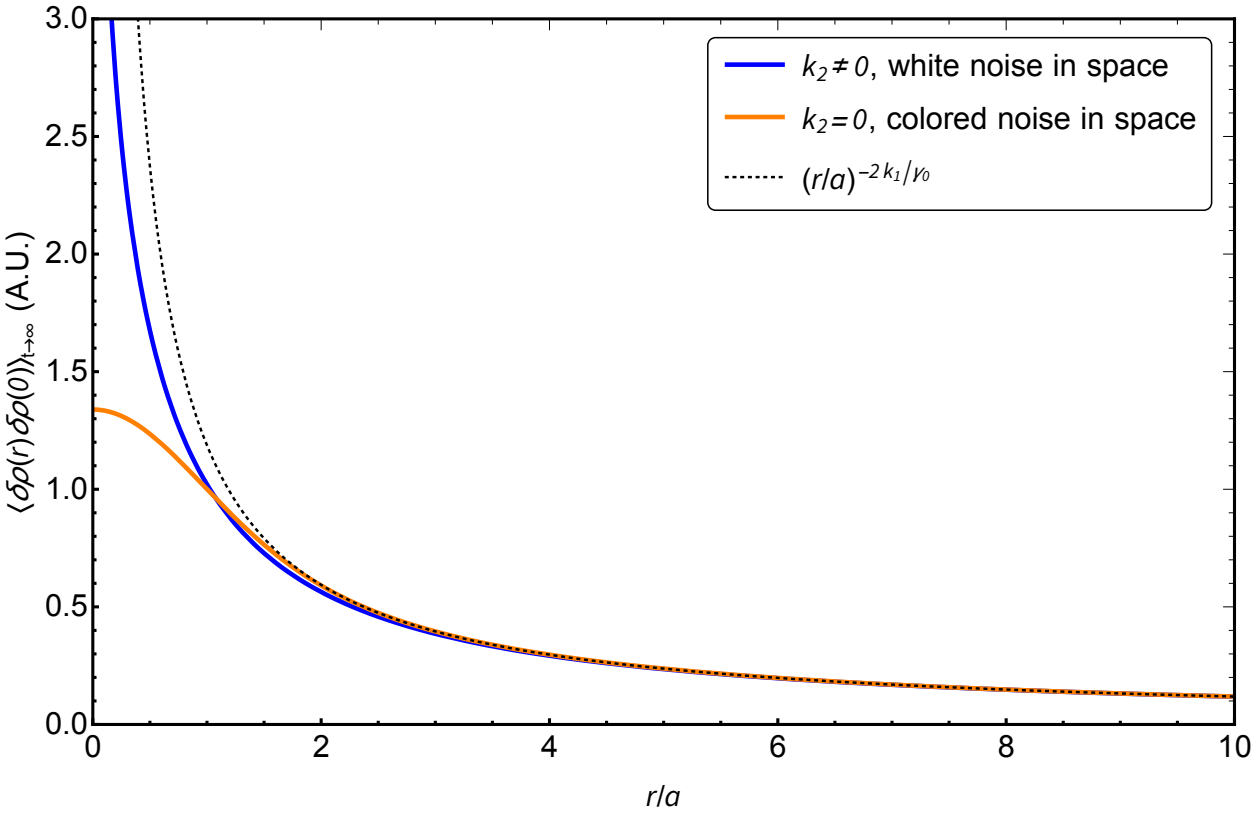

Figure B.1: Plot of density-density correlation function for Laplacian feedback ($k_2 \neq 0$) and the simple stress feedback ($k_2 = 0$) discussed in Chapter 4. In the case of $k_2 \neq 0$, the approach to the power law is slower. The plot is for $k_1 = \gamma_0/2$. For $k_2 = 0$, a is the width of the colored noise, whereas for $k_2 \neq 0$, $a = \sqrt{4k_2/\gamma_0}$.

APPENDIX C

MATLAB Codes for Chapter 3

In this appendix, we list the image analysis codes discussed in Chapter 3. The codes were tested in MATLAB edition R2018a.

C.1 Adult Wing Segmentation

Listing C.1: Adult Wing Segmentation

```
filename = 'image0001'; %type the name of the input image here
E = imread(strcat(filename,'.tif'));

Image = rgb2gray(E);

%manual segmentation of wing hinge
J =roipoly(Image);

BWs = 1-imbinarize(Image); %global threshold

%%morphological operations on the global threshold
BWdfill = imfill(BWs, 'holes'); %fill the holes

seD = strel('diamond',10); %size of erosion. recommended: 10
seC = strel('disk',3); %radius of closing. recommended: 3
seO = strel('disk',5); %radius of opening. recommended: 5
BWfinal = imclose(BWdfill,seC);
BWfinal = imopen(BWfinal,seO);
BWfinal = imfill(BWfinal, 'holes'); %fill any remaining holes
%erodes the image
BWfinal = imerode(BWfinal,seD);

Iblur = imgaussfilt(Image, 10); %blurring the image with standard ...
    deviation 10
```

```
%adaptive threshold with sensitivity = 0.78
BWs2 = 1-imbinarize(Iblur,'adaptive','Sensitivity',0.78);

skeleton = bwmorph(BWs2,'thin',inf); %thinning the skeleton
%make a cut through the initial segmentation
BWfinal2 = (1-skeleton).*BWfinal;

%remove the cut out bristles with morphological opening
BWfinal2 = imopen(BWfinal2,strel('disk',20));
%pick the largest connected component. Useful when there are leftover ...
    pieces that we don't want
BWfinal2 = bwareafilt(logical(BWfinal2),1,4);

%morphologically close to fill out the interior cuts
BWfinal2 = imclose(BWfinal2,strel('disk',30));
BWfinal2 = imfill(BWfinal2, 'holes'); %fill any remaining holes

BWfinal3 = BWfinal2;
blurryImage = imgaussfilt(double(BWfinal3), 50);
BWfinal3 = blurryImage > 0.5;
BWfinal3 = J.*BWfinal3;

A=bwarea(BWfinal3)
csvwrite(strcat(filename,'.csv'),A)
```

C.2 Finding Vein Crossing Landmarks

Listing C.2: Finding Landmarks

```
filename = 'image0001'; %type the name of the input image here
E = imread(strcat(filename,'.tif'));

E = fliplr(E);   %use for left wing images to orient them the same way ...
    as right wings
Image = rgb2gray(E);

Iblur = imgaussfilt(Image, 10);
BWs2 = 1-imbinarize(Iblur,'adaptive','Sensitivity',0.78);
skeleton = bwmorph(BWs2,'thin',inf);

```

```
%pick landmarks in the same order for all images
x = zeros(1,7);
y = zeros (1,7);
for i =1:7
    roi = roipoly(skeleton);
    crossing = bwmorph(roi .* skeleton,'branchpoints');
    [y(1,i),x(1,i)] = find(crossing);
end

M = [x',y']

%the name of the .csv files should start from 1
csvwrite('results_1.csv',M)
```

C.3 Procrustes Analysis

Listing C.3: Procrustes

```
%%import csv files of the positions of 7 landmarks
m=76; %number of csv files
M = cell(m,1);
% Read results_1.csv through results_m.csv.
% Files are in the "crossings/" directory.
for k = 1:m
  csvFilename = sprintf('results_%d.csv', k);
  fullFileName = fullfile('¬/crossings/', csvFilename);
  csvData = csvread(fullFileName);
  M{k} = csvData;

end

%%translate points to have the same origin
TM = cell(m,1);
for k = 1:m
    TM{k} = M{k} - sum(M{k})/7;
end

%%scale each wing to be get rid of variabilities in size
SM = cell(m,1);
S_list = cell(1,1);
```

```
23
24 meanS = 0;
25 for k = 1:m
26     S = sqrt(sum(TM{k}(:,1).^2)+sum(TM{k}(:,2).^2))
27     S_list{1}(k) = S;
28     meanS = meanS + S;
29     SM{k} = TM{k}/S;
30 end
31
32 meanS = meanS/m;
33
34 %%rotate each wing onto a reference (average) wing
35 refSM = zeros(7,2);
36 for k = 1:m
37     refSM = refSM + SM{k};
38 end
39 refSM = refSM/m;
40 %refSM = SM{1};
41
42 RM = cell(m,1);
43
44 for k = 1:m
45     Theta = atan((sum(SM{k}(:,1).*refSM(:,2))
46     -sum(SM{k}(:,2).*refSM(:,1)))/(sum(SM{k}(:,1).*refSM(:,1))
47     +sum(SM{k}(:,2).*refSM(:,2))));
48     RM{k}(:,1) = cos(Theta)*SM{k}(:,1) - sin(Theta)*SM{k}(:,2);
49     RM{k}(:,2) = sin(Theta)*SM{k}(:,1) + cos(Theta)*SM{k}(:,2);
50 end
51
52 %%calculate the variability in landmark positions
53 xyList = cell(7,1); %list of x-y coordinates sorted based on each ...
       landmarks and not different wings
54 TrC = 0; %Trace of 14x14 Covariance matrix
55 for i = 1:7
56     for k = 1:m
57         xyList{i}(k,1) = RM{k}(i,1);
58         xyList{i}(k,2) = RM{k}(i,2);
59     end
60     TrC = TrC + sum(var(xyList{i}));
61  end
62  Sigma_pixels = meanS * sqrt(TrC/10) %Sigma in pixels
63  Sigma_microns = Sigma_pixels*0.66 %each pixel in the original image ...
       was calculated to be 0.66 microns. Can vary based on the resolution ...
```

```
       of the image.
64
65
66  %% calculate L-R difference for the same fly
67 Delta_LR = cell(m/2,1);
68 RM_left = cell(m/2,1);  %list of left wings
69 RM_right = cell(m/2,1); %list of right wings
70
71 Area_FA = 0;
72
73  for k = 1:m/2
74      RM_left{k} = RM{2*k-1};
75      RM_right{k} = RM{2*k};
76  end
77
78  for k = 1:m/2
79      Delta_LR{k} = RM_left{k} - RM_right{k};
80  end
81
82  %%calculate the variability  for L-R
83 xyList_LR = cell(7,1); %list of x-y coords sorted based on each ...
       landmarks and not different wings
84 TrC_LR = 0; %Trace of 14x14 Covariance matrix
85 for i = 1:7
86     for k = 1:m/2
87         xyList_LR{i}(k,1) = Delta_LR{k}(i,1);
88         xyList_LR{i}(k,2) = Delta_LR{k}(i,2);
89     end
90     TrC_LR = TrC_LR + sum(var(xyList_LR{i}));
91  end
92  Sigma_pixels_LR = meanS * sqrt(TrC_LR/10)
93  Sigma_microns_LR = Sigma_pixels_LR*0.66 %each pixel in the original ...
       image was calculated to be 0.66 microns
94
95
96 % %only use the following for results from the same wing with only ...
       changing threshold cutoffs
97 %
98  xyList = cell(7,1); %list of x-y coords sorted based on each landmarks ...
       and not different wings
99  TrC = 0; %Trace of 14x14 Covariance matrix
100  for i = 1:7
101      for k = 6:5+m
```

```
102             xyList{i}(k-5,1) = M{k-5}(i,1);
103             xyList{i}(k-5,2) = M{k-5}(i,2);
104         end
105         TrC = TrC + sum(var(xyList{i}));
106     end
107     Sigma_pixels = sqrt(TrC/14) %devided by 14 (instead of 10) because M ...
            has all 14 degrees of freedom
108     Sigma_microns = Sigma_pixels*0.66 %each pixel in the original image ...
            was calculated to be 0.66 microns
```

Bibliography

[1] A. Garelli, A. M. Gontijo, V. Miguela, E. Caparros, and M. Dominguez. Imaginal discs secrete insulin-like peptide 8 to mediate plasticity of growth and maturation. *Science*, 336(6081):579–82, 2012.

[2] E. Boone, J. Colombani, D. S. Andersen, and P. Leopold. The hippo signalling pathway coordinates organ growth and limits developmental variability by controlling dilp8 expression. *Nat Commun*, 7:13505, 2016.

[3] Natalie A. Dye, Marko Popović, Stephanie Spannl, Raphaël Etournay, Dagmar Kainmüller, Suhrid Ghosh, Eugene W. Myers, Frank Jülicher, and Suzanne Eaton. Cell dynamics underlying oriented growth of the drosophila wing imaginal disc. *Development*, 144(23):4406, 2017.

[4] I. Heemskerk, T. Lecuit, and L. LeGoff. Dynamic clonal analysis based on chronic in vivo imaging allows multiscale quantification of growth in the drosophila wing disc. *Development*, 141(11):2339–48, 2014.

[5] T. Bittig, O. Wartlick, M. Gonzalez-Gaitan, and F. Julicher. Quantification of growth asymmetries in developing epithelia. *Eur Phys J E Soft Matter*, 30(1):93–9, 2009.

[6] J. Ranft, M. Basan, J. Elgeti, J. F. Joanny, J. Prost, and F. Jülicher. Fluidization of tissues by cell division and apoptosis. *Proc Natl Acad Sci USA*, 107(49):20863–20868, 2010.

[7] N. T. Ingolia. Topology and robustness in the drosophila segment polarity network. *PLoS Biol*, 2(6):e123, 2004.

[8] L. Michaelis, M. L. Menten, K. A. Johnson, and R. S. Goody. The original michaelis constant: translation of the 1913 michaelis-menten paper. *Biochemistry*, 50(39):8264–9, 2011.

[9] A. M. Turing. The chemical basis of morphogenesis. *Philosophical Transactions of the Royal Society of London. Series B, Biological Sciences*, 237(641):37–72, 1952.

[10] Britton Chance. The kinetics of the enzyme-substrate compound of peroxidase. *Journal of Biological Chemistry*, 151(2):553–577, 1943.

[11] S. Kondo and T. Miura. Reaction-diffusion model as a framework for understanding biological pattern formation. *Science*, 329(5999):1616–20, 2010.

[12] T. M. Yi, Y. Huang, M. I. Simon, and J. Doyle. Robust perfect adaptation in bacterial chemotaxis through integral feedback control. *Proc Natl Acad Sci U S A*, 97(9):4649–53, 2000.

[13] A. D. Lander, K. K. Gokoffski, F. Y. Wan, Q. Nie, and A. L. Calof. Cell lineages and the logic of proliferative control. *PLoS Biol*, 7(1):e15, 2009.

[14] J. J. Tyson, K. C. Chen, and B. Novak. Sniffers, buzzers, toggles and blinkers: dynamics of regulatory and signaling pathways in the cell. *Curr Opin Cell Biol*, 15(2):221–31, 2003.

[15] E. M. Ozbudak, M. Thattai, H. N. Lim, B. I. Shraiman, and A. Van Oudenaarden. Multistability in the lactose utilization network of escherichia coli. *Nature*, 427(6976):737–40, 2004.

[16] W Thompson d'Arcy. *On growth and form*, volume 1. Cambridge UP, 1952.

[17] W. F. Marshall. Subcellular size. *Cold Spring Harb Perspect Biol*, 7(6), 2015.

[18] T. Ryan Gregory. The bigger the c-value, the larger the cell: Genome size and red blood cell size in vertebrates. *Blood Cells, Molecules, and Diseases*, 27(5):830–843, 2001.

[19] A. A. Amodeo and J. M. Skotheim. Cell-size control. *Cold Spring Harb Perspect Biol*, 8(4):a019083, 2016.

[20] D. L. Levy and R. Heald. Biological scaling problems and solutions in amphibians. *Cold Spring Harb Perspect Biol*, 8(1):a019166, 2015.

[21] Rewatee H. Gokhale and Alexander W. Shingleton. Size control: the developmental physiology of body and organ size regulation. *Wiley Interdisciplinary Reviews: Developmental Biology*, 4(4):335–356, 2015.

[22] H. Tsukaya. Leaf development. *Arabidopsis Book*, 11:e0163, 2013.

[23] H. Czesnick and M. Lenhard. Size control in plants–lessons from leaves and flowers. *Cold Spring Harb Perspect Biol*, 7(8):a019190, 2015.

[24] Iswar K Hariharan. Organ size control: Lessons from drosophila. *Developmental Cell*, 34(3):255–265, 2015.

[25] C. K. Mirth and L. M. Riddiford. Size assessment and growth control: how adult size is determined in insects. *Bioessays*, 29(4):344–55, 2007.

[26] D. S. Andersen, J. Colombani, and P. Leopold. Coordination of organ growth: principles and outstanding questions from the world of insects. *Trends Cell Biol*, 23(7):336–44, 2013.

[27] A. I. Penzo-Mendez and B. Z. Stanger. Organ-size regulation in mammals. *Cold Spring Harb Perspect Biol*, 7(9):a019240, 2015.

[28] V. Debat, S. Bloyer, F. Faradji, N. Gidaszewski, N. Navarro, P. Orozco-Terwengel, V. Ribeiro, C. Schlotterer, J. S. Deutsch, and F. Peronnet. Developmental stability: a major role for cyclin g in drosophila melanogaster. *PLoS Genet*, 7(10):e1002314, 2011.

[29] J. Colombani, D. S. Andersen, L. Boulan, E. Boone, N. Romero, V. Virolle, M. Texada, and P. Leopold. Drosophila lgr3 couples organ growth with maturation and ensures developmental stability. *Curr Biol*, 25(20):2723–9, 2015.

[30] L. Abouchar, M. D. Petkova, C. R. Steinhardt, and T. Gregor. Fly wing vein patterns have spatial reproducibility of a single cell. *J R Soc Interface*, 11(97):20140443, 2014.

[31] John H. Graham, Shmuel Raz, Hagit Hel-Or, and Eviatar Nevo. Fluctuating asymmetry: Methods, theory, and applications. *Symmetry*, 2010.

[32] V. Debat and F. Peronnet. Asymmetric flies: the control of developmental noise in drosophila. *Fly (Austin)*, 7(2):70–7, 2013.

[33] A. Raj and A. van Oudenaarden. Nature, nurture, or chance: stochastic gene expression and its consequences. *Cell*, 135(2):216–26, 2008.

[34] Mukund Thattai and Alexander van Oudenaarden. Intrinsic noise in gene regulatory networks. *Proceedings of the National Academy of Sciences*, 98(15):8614, 2001.

[35] Ertugrul M. Ozbudak, Mukund Thattai, Iren Kurtser, Alan D. Grossman, and Alexander van Oudenaarden. Regulation of noise in the expression of a single gene. *Nature Genetics*, 31(1):69–73, 2002.

[36] I. Golding, J. Paulsson, S. M. Zawilski, and E. C. Cox. Real-time kinetics of gene activity in individual bacteria. *Cell*, 123(6):1025–36, 2005.

[37] Arjun Raj, Charles S. Peskin, Daniel Tranchina, Diana Y. Vargas, and Sanjay Tyagi. Stochastic mrna synthesis in mammalian cells. *PLOS Biology*, 4(10):e309, 2006.

[38] Nitzan Rosenfeld, Jonathan W. Young, Uri Alon, Peter S. Swain, and Michael B. Elowitz. Gene regulation at the single-cell level. *Science*, 307(5717):1962, 2005.

[39] A. M. Klein, D. P. Doupe, P. H. Jones, and B. D. Simons. Kinetics of cell division in epidermal maintenance. *Phys Rev E Stat Nonlin Soft Matter Phys*, 76(2 Pt 1):021910, 2007.

[40] P. J. Bryant and P. Simpson. Intrinsic and extrinsic control of growth in developing organs. *Q Rev Biol*, 59(4):387–415, 1984.

[41] P. J. Bryant and P. Levinson. Intrinsic growth control in the imaginal primordia of drosophila, and the autonomous action of a lethal mutation causing overgrowth. *Dev Biol*, 107(2):355–63, 1985.

[42] S. J. Silber. Growth of baby kidneys transplanted into adults. *Arch Surg*, 111(1):75–7, 1976.

[43] I. K. Hariharan, D. B. Wake, and M. H. Wake. Indeterminate growth: Could it represent the ancestral condition? *Cold Spring Harb Perspect Biol*, 8(2):a019174, 2015.

[44] N. F. Parker and A. W. Shingleton. The coordination of growth among drosophila organs in response to localized growth-perturbation. *Dev Biol*, 357(2):318–25, 2011.

[45] Alberto Roselló-Díez, Linda Madisen, Sébastien Bastide, Hongkui Zeng, and Alexandra L. Joyner. Cell-nonautonomous local and systemic responses to cell arrest enable long-bone catch-up growth in developing mice. *PLOS Biology*, 16(6):e2005086, 2018.

[46] Laura Boulan, Ditte Andersen, Julien Colombani, Emilie Boone, and Pierre Léopold. Inter-organ growth coordination is mediated by the xrp1-dilp8 axis in drosophila. *Developmental Cell*, 2019.

[47] J. Colombani, D. S. Andersen, and P. Leopold. Secreted peptide dilp8 coordinates drosophila tissue growth with developmental timing. *Science*, 336(6081):582–5, 2012.

[48] T. Katsuyama, F. Comoglio, M. Seimiya, E. Cabuy, and R. Paro. During drosophila disc regeneration, jak/stat coordinates cell proliferation with dilp8-mediated developmental delay. *Proc Natl Acad Sci U S A*, 112(18):E2327–36, 2015.

[49] L. Herboso, M. M. Oliveira, A. Talamillo, C. Perez, M. Gonzalez, D. Martin, J. D. Sutherland, A. W. Shingleton, C. K. Mirth, and R. Barrio. Ecdysone promotes growth of imaginal discs through the regulation of thor in d. melanogaster. *Sci Rep*, 5:12383, 2015.

[50] Daniel Aguilar-Hidalgo, Steffen Werner, Ortrud Wartlick, Marcos González-Gaitán, Benjamin M. Friedrich, and Frank Jülicher. Critical point in self-organized tissue growth. *Physical Review Letters*, 120(19):198102, 2018.

[51] Boris I. Shraiman. Mechanical feedback as a possible regulator of tissue growth. *Proc Natl Acad Sci USA*, 102(9):3318–23, 2005.

[52] L. Legoff, H. Rouault, and T. Lecuit. A global pattern of mechanical stress polarizes cell divisions and cell shape in the growing drosophila wing disc. *Development*, 140(19):4051–9, 2013.

[53] K. D. Irvine and B. I. Shraiman. Mechanical control of growth: ideas, facts and challenges. *Development*, 144(23):4238–4248, 2017.

[54] Alexander D. Golden. *Feedback models in biological physics*. Phd thesis, University of Michigan, 2018.

[55] S. M. Zehnder, M. Suaris, M. M. Bellaire, and T. E. Angelini. Cell volume fluctuations in mdck monolayers. *Biophys J*, 108(2):247–50, 2015.

[56] S. M. Zehnder, M. K. Wiatt, J. M. Uruena, A. C. Dunn, W. G. Sawyer, and T. E. Angelini. Multicellular density fluctuations in epithelial monolayers. *Phys Rev E Stat Nonlin Soft Matter Phys*, 92(3):032729, 2015.

[57] N. Hervieux, M. Dumond, A. Sapala, A. L. Routier-Kierzkowska, D. Kierzkowski, A. H. K. Roeder, R. S. Smith, A. Boudaoud, and O. Hamant. A mechanical feedback restricts sepal growth and shape in arabidopsis. *Curr Biol*, 26(8):1019–1028, 2016.

[58] Matthew C. Gibson, Ankit B. Patel, Radhika Nagpal, and Norbert Perrimon. The emergence of geometric order in proliferating metazoan epithelia. *Nature*, 442(7106):1038–41, 2006.

[59] A. Goriely. *The Mathematics and Mechanics of Biological Growth*. Springer, 2017.

[60] E. H. Lee. Elastic-plastic deformation at finite strains. *Journal of Applied Mechanics*, 36(1):1–6, 1969.

[61] Raymond E. Goldstein and Alain Goriely. Dynamic buckling of morphoelastic filaments. *Physical Review E*, 74(1):010901, 2006.

[62] A. Goriely and M. Ben Amar. Differential growth and instability in elastic shells. *Phys Rev Lett*, 94(19):198103, 2005.

[63] Edward K. Rodriguez, Anne Hoger, and Andrew D. McCulloch. Stress-dependent finite growth in soft elastic tissues. *Journal of Biomechanics*, 27(4):455–467, 1994.

[64] E. Efrati, E. Sharon, and R. Kupferman. Elastic theory of unconstrained non-euclidean plates. *J Mech Phys Sol*, 57(4):762–775, 2009.

[65] Eran Sharon and Efi Efrati. The mechanics of non-euclidean plates. *Soft Matter*, 6(22):5693–5704, 2010.

[66] Benoit B Mandelbrot. *The fractal geometry of nature*, volume 1. W. H. Freeman and Company, 1982.

[67] Fereydoon Family and Tamas Vicsek. *Dynamics of fractal surfaces*. World Scientific, 1991.

[68] A-L Barabási and Harry Eugene Stanley. *Fractal concepts in surface growth*. Cambridge university press, 1995.

[69] Mehran Kardar, Giorgio Parisi, and Yi-Cheng Zhang. Dynamic scaling of growing interfaces. *Phys Rev Lett*, 56(9):889–892, 1986.

[70] J Maunuksela, M Myllys, O-P Kähkönen, J Timonen, N Provatas, MJ Alava, and T Ala-Nissila. Kinetic roughening in slow combustion of paper. *Physical review letters*, 79(8):1515, 1997.

[71] Jun-ichi Wakita, Hiroto Itoh, Tohey Matsuyama, and Mitsugu Matsushita. Self-affinity for the growing interface of bacterial colonies. *Journal of the Physical Society of Japan*, 66(1):67–72, 1997.

[72] Kazumasa A Takeuchi and Masaki Sano. Universal fluctuations of growing interfaces: evidence in turbulent liquid crystals. *Physical review letters*, 104(23):230601, 2010.

[73] Peter J Yunker, Matthew A Lohr, Tim Still, Alexei Borodin, Douglas J Durian, and Arjun G Yodh. Effects of particle shape on growth dynamics at edges of evaporating drops of colloidal suspensions. *Physical review letters*, 110(3):035501, 2013.

[74] T. A. Witten and L. M. Sander. Diffusion-limited aggregation, a kinetic critical phenomenon. *Phys. Rev. Lett.*, 47:1400–1403, Nov 1981.

[75] M Batty, P Longley, and S Fotheringham. Urban growth and form: Scaling, fractal geometry, and diffusion-limited aggregation. *Environment and Planning A: Economy and Space*, 21(11):1447–1472, 1989.

[76] A.R. Liddle and D.H. Lyth. *Cosmological Inflation and Large-Scale Structure*. Cambridge UP, 2000.

[77] H. F. Nijhout and V. Callier. Developmental mechanisms of body size and wing-body scaling in insects. *Annu Rev Entomol*, 60:141–56, 2015.

[78] Casper J. Breuker, James S. Patterson, and Christian Peter Klingenberg. A single basis for developmental buffering of drosophila wing shape. *PLOS ONE*, 1(1):e7, 2006.

[79] John H. Graham, Kunio Shimizu, John M. Emlen, D. Carl Freeman, and John Merkel. Growth models and the expected distribution of fluctuating asymmetry. *Biological Journal of the Linnean Society*, 80(1):57–65, 2003.

[80] STEVEN W Gangestad and RANDY Thornhill. Fluctuating asymmetry, developmental instability, and fitness: Toward model-based interpretation. *Developmental instability: Causes and consequences*, pages 62–80, 2003.

[81] G. A. Babbitt. Inbreeding reduces power-law scaling in the distribution of fluctuating asymmetry: an explanation of the basis of developmental instability. *Heredity*, 97(4):258–268, 2006.

[82] S. V. Dongen. Fluctuating asymmetry and developmental instability in evolutionary biology: past, present and future. *J Evol Biol*, 19(6):1727–43, 2006.

[83] C. P. Klingenberg. Analyzing fluctuating asymmetry with geometric morphometrics: Concepts, methods, and applications. *Symmetry-Basel*, 7(2):843–934, 2015.

[84] Christian Peter Klingenberg and H. Frederik Nijhout. Genetics of fluctuating asymmetry: A developmental model of developmental instability. *Evolution*, 53(2):358–375, 1999.

[85] Christian Peter Klingenberg. *A developmental perspective on developmental instability: theory, models and mechanisms*, pages 14–34. Oxford UP, Oxford, 2003.

[86] Larry J. Leamy and Christian Peter Klingenberg. The genetics and evolution of fluctuating asymmetry. *Annual Review of Ecology, Evolution, and Systematics*, 36(1):1–21, 2005.

[87] P. A. Haas, Ssmh Hohn, A. R. Honerkamp-Smith, J. B. Kirkegaard, and R. E. Goldstein. The noisy basis of morphogenesis: Mechanisms and mechanics of cell sheet folding inferred from developmental variability. *PLoS Biol*, 16(7):e2005536, 2018.

[88] T. P. Neufeld, A. F. de la Cruz, L. A. Johnston, and B. A. Edgar. Coordination of growth and cell division in the drosophila wing. *Cell*, 93(7):1183–93, 1998.

[89] J. S. Jaszczak, J. B. Wolpe, A. Q. Dao, and A. Halme. Nitric oxide synthase regulates growth coordination during drosophila melanogaster imaginal disc regeneration. *Genetics*, 2015.

[90] J. S. Jaszczak, J. B. Wolpe, R. Bhandari, R. G. Jaszczak, and A. Halme. Growth coordination during drosophila melanogaster imaginal disc regeneration is mediated by signaling through the relaxin receptor lgr3 in the prothoracic gland. *Genetics*, 2016.

[91] Laura Boulan, Marco Milán, and Pierre Léopold. The systemic control of growth. *Cold Spring Harbor Perspectives in Biology*, 7(12), 2015.

[92] A. A. Green, K. R. Mosaliganti, I. A. Swinburne, N. D. Obholzer, and S. G. Megason. Recovery of shape and size in a developing organ pair. *Dev Dyn*, 246(6):451–465, 2017.

[93] R. H. Gokhale, T. Hayashi, C. D. Mirque, and A. W. Shingleton. Intra-organ growth coordination in drosophila is mediated by systemic ecdysone signaling. *Dev Biol*, 418(1):135–145, 2016.

[94] Y. Demay, J. Perochon, S. Szuplewski, B. Mignotte, and S. Gaumer. The perk pathway independently triggers apoptosis and a rac1/slpr/jnk/dilp8 signaling favoring tissue homeostasis in a chronic er stress drosophila model. *Cell Death Dis*, 5:e1452, 2014.

[95] H. F. Nijhout and D. E. Wheeler. Growth models of complex allometries in holometabolous insects. *The American Naturalist*, 148(1):40–56, 1996.

[96] H. F. Nijhout and D. J. Emlen. Competition among body parts in the development and evolution of insect morphology. *Proc Natl Acad Sci U S A*, 95(7):3685–9, 1998.

[97] C. P. Klingenberg and H. F. Nijhout. Competition among growing organs and developmental control of morphological asymmetry. *Proceedings of the Royal Society B-Biological Sciences*, 265(1401):1135–1139, 1998.

[98] D. J. Emlen, Q. Szafran, L. S. Corley, and I. Dworkin. Insulin signaling and limb-patterning: candidate pathways for the origin and evolutionary diversification of beetle 'horns'. *Heredity (Edinb)*, 97(3):179–91, 2006.

[99] M. Scott, C. W. Gunderson, E. M. Mateescu, Z. Zhang, and T. Hwa. Interdependence of cell growth and gene expression: origins and consequences. *Science*, 330(6007):1099–102, 2010.

[100] M. Mori, T. Hwa, O. C. Martin, A. De Martino, and E. Marinari. Constrained allocation flux balance analysis. *PLoS Comput Biol*, 12(6):e1004913, 2016.

[101] L. Mohapatra, T. J. Lagny, D. Harbage, P. R. Jelenkovic, and J. Kondev. The limiting-pool mechanism fails to control the size of multiple organelles. *Cell Syst*, 4(5):559–567.e14, 2017.

[102] O. Wartlick, P. Mumcu, A. Kicheva, T. Bittig, C. Seum, F. Julicher, and M. Gonzalez-Gaitan. Dynamics of dpp signaling and proliferation control. *Science*, 331(6021):1154–9, 2011.

[103] O. Karin, A. Swisa, B. Glaser, Y. Dor, and U. Alon. Dynamical compensation in physiological circuits. *Mol Syst Biol*, 12(11):886, 2016.

[104] C.W. Gardiner. *Handbook of Stochastic Methods for Physics, Chemistry, and the Natural Sciences*. Springer, third edition, 2004.

[105] P. R. Somvanshi, A. K. Patel, S. Bhartiya, and K. V. Venkatesh. Implementation of integral feedback control in biological systems. *Wiley Interdiscip Rev Syst Biol Med*, 7(5):301–16, 2015.

[106] Morten E. Moeller, Stanislav Nagy, Stephan U. Gerlach, Karen C. Soegaard, E. Thomas Danielsen, Michael J. Texada, and Kim F. Rewitz. Warts signaling controls organ and body growth through regulation of ecdysone. *Current Biology*, 27(11):1652–1659.e4, 2017.

[107] A. R. Palmer and C. Strobeck. Fluctuating asymmetry: Measurement, analysis, patterns. *Annual Review of Ecology and Systematics*, 17(1):391–421, 1986.

[108] J. Parker. Morphogens, nutrients, and the basis of organ scaling. *Evol Dev*, 13(3):304–14, 2011.

[109] T. Aegerter-Wilmsen, M. B. Heimlicher, A. C. Smith, P. B. de Reuille, R. S. Smith, C. M. Aegerter, and K. Basler. Integrating force-sensing and signaling pathways in a model for the regulation of wing imaginal disc size. *Development*, 139(17):3221–31, 2012.

[110] L. Setiawan, X. Pan, A. L. Woods, M. B. O'Connor, and I. K. Hariharan. The bmp2/4 ortholog dpp can function as an inter-organ signal that regulates developmental timing. *Life Sci Alliance*, 1(6):e201800216, 2018.

[111] Osvaldo Chara, Elly M. Tanaka, and Lutz Brusch. *Chapter Ten - Mathematical Modeling of Regenerative Processes*, volume Volume 108, pages 283–317. Academic Press, 2014.

[112] Z. R. Zhou, H. Alegot, and K. D. Irvine. Oriented cell divisions are not required for drosophila wing shape. *Current Biology*, 29(5):856–+, 2019.

[113] S. Juarez-Carreño, J. Morante, and M. Dominguez. Systemic signalling and local effectors in developmental stability, body symmetry, and size. *Cell Stress*, 2(12):340–361, 2018.

[114] Roshan K. Vijendravarma, Sunitha Narasimha, and Tadeusz J. Kawecki. Adaptation to larval malnutrition does not affect fluctuating asymmetry in *Drosophila* melanogaster. *Biological Journal of the Linnean Society*, 104(1):19–28, 2011.

[115] N. Otsu. A threshold selection method from gray-level histograms. *IEEE Transactions on Systems, Man, and Cybernetics*, 9(1):62–66, 1979.

[116] O. K. Damavandi and D. K. Lubensky. Statistics of noisy growth with mechanical feedback in elastic tissues. *Proc Natl Acad Sci U S A*, 116(12):5350–5355, 2019.

[117] M. Milán, S. Campuzano, and A. García-Bellido. Cell cycling and patterned cell proliferation in the wing primordium of drosophila. *Proc Natl Acad Sci USA*, 93(2):640–645, 1996.

[118] Heather M. Meyer and Adrienne H. K. Roeder. Stochasticity in plant cellular growth and patterning. *Front Plant Sci*, 5:420, 2014.

[119] A. M. Klein and B. D. Simons. Universal patterns of stem cell fate in cycling adult tissues. *Development*, 138(15):3103–11, 2011.

[120] Joaquín de Navascués, Carolina N Perdigoto, Yu Bian, Markus H Schneider, Allison J Bardin, Alfonso Martínez-Arias, and Benjamin D Simons. Drosophila midgut homeostasis involves neutral competition between symmetrically dividing intestinal stem cells. *EMBO J*, 31(11):2473–2485, 2012.

[121] S. Rulands, F. Lescroart, S. Chabab, C. J. Hindley, N. Prior, M. K. Sznurkowska, M. Huch, A. Philpott, C. Blanpain, and B. D. Simons. Universality of clone dynamics during tissue development. *Nat Phys*, 14(5):469–474, 2018.

[122] Y. Pan, I. Heemskerk, C. Ibar, B. I. Shraiman, and K. D. Irvine. Differential growth triggers mechanical feedback that elevates hippo signaling. *Proc Natl Acad Sci USA*, 113(45):E6974–E6983, 2016.

[123] P. Greulich and B. D. Simons. Dynamic heterogeneity as a strategy of stem cell self-renewal. *Proc Natl Acad Sci USA*, 113(27):7509–7514, 2016.

[124] S. Tsugawa, N. Hervieux, D. Kierzkowski, A. L. Routier-Kierzkowska, A. Sapala, O. Hamant, R. S. Smith, A. H. K. Roeder, A. Boudaoud, and C. B. Li. Clones of cells switch from reduction to enhancement of size variability in arabidopsis sepals. *Development*, 144(23):4398–4405, 2017.

[125] A. Puliafito, L. Hufnagel, P. Neveu, S. Streichan, A. Sigal, D. K. Fygenson, and B. I. Shraiman. Collective and single cell behavior in epithelial contact inhibition. *Proc Natl Acad Sci USA*, 109(3):739–44, 2012.

[126] S. J. Streichan, C. R. Hoerner, T. Schneidt, D. Holzer, and L. Hufnagel. Spatial constraints control cell proliferation in tissues. *Proc Natl Acad Sci USA*, 111(15):5586–91, 2014.

[127] A. Puliafito, L. Primo, and A. Celani. Cell-size distribution in epithelial tissue formation and homeostasis. *J R Soc Interface*, 14(128):20170032, 2017.

[128] D. Y. Chen, W. Y. Aw, D. Devenport, and S. Torquato. Structural characterization and statistical-mechanical model of epidermal patterns. *Biophys J*, 111(11):2534–2545, 2016.

[129] N. Hervieux, S. Tsugawa, A. Fruleux, M. Dumond, A. L. Routier-Kierzkowska, T. Komatsuzaki, A. Boudaoud, J. C. Larkin, R. S. Smith, C. B. Li, and O. Hamant. Mechanical shielding of rapidly growing cells buffers growth heterogeneity and contributes to organ shape reproducibility. *Curr Biol*, 27(22):3468–3479.e4, 2017.

[130] A. Garcia-Bellido, P. Ripoll, and G. Morata. Developmental compartmentalisation of the wing disk of drosophila. *Nat New Biol*, 245(147):251–3, 1973.

[131] A. Garcia-Bellido, P. Ripoll, and G. Morata. Developmental compartmentalization in the dorsal mesothoracic disc of drosophila. *Dev Biol*, 48(1):132–147, 1976.

[132] Romain Levayer, Barbara Hauert, and Eduardo Moreno. Cell mixing induced by myc is required for competitive tissue invasion and destruction. *Nature*, 524(7566):476, 2015.

[133] Lars Hufnagel, Aurelio A. Teleman, Hervé Rouault, Stephen M. Cohen, and Boris I. Shraiman. On the mechanism of wing size determination in fly development. *Proc Natl Acad Sci USA*, 104(10):3835–40, 2007.

[134] T. Aegerter-Wilmsen, C. M. Aegerter, E. Hafen, and K. Basler. Model for the regulation of size in the wing imaginal disc of drosophila. *Mech Dev*, 124(4):318–26, 2007.

[135] Ashok Ramasubramanian and Larry A. Taber. Computational modeling of morphogenesis regulated by mechanical feedback. *Biomech Model Mechanobiol*, 7(2):77–91, 2008.

[136] Tinri Aegerter-Wilmsen, Alister C. Smith, Alix J. Christen, Christof M. Aegerter, Ernst Hafen, and Konrad Basler. Exploring the effects of mechanical feedback on epithelial topology. *Development*, 137(3):499–506, 2010.

[137] K. Alim, O. Hamant, and A. Boudaoud. Regulatory role of cell division rules on tissue growth heterogeneity. *Front Plant Sci*, 3:174, 2012.

[138] E. Hannezo, J. Prost, and J. F. Joanny. Growth, homeostatic regulation and stem cell dynamics in tissues. *J R Soc Interface*, 11(93):20130895, 2014.

[139] J. Kursawe, P. A. Brodskiy, J. J. Zartman, R. E. Baker, and A. G. Fletcher. Capabilities and limitations of tissue size control through passive mechanical forces. *PloS Comput Biol*, 11(12):26, 2015.

[140] S. W. Lee and Y. Morishita. Possible roles of mechanical cell elimination intrinsic to growing tissues from the perspective of tissue growth efficiency and homeostasis. *PLoS Comput Biol*, 13(7):e1005651, 2017.

[141] Amy Buchmann, Mark Alber, and Jeremiah J. Zartman. Sizing it up: The mechanical feedback hypothesis of organ growth regulation. *Semin Cell Dev Biol*, 35:73–81, 2014.

[142] M. Ma, X. Cao, J. Dai, and J. C. Pastor-Pareja. Basement membrane manipulation in drosophila wing discs affects dpp retention but not growth mechanoregulation. *Dev Cell*, 42(1):97–106 e4, 2017.

[143] Thomas Schluck, Ulrike Nienhaus, Tinri Aegerter-Wilmsen, and Christof M. Aegerter. Mechanical control of organ size in the development of the drosophila wing disc. *PLOS ONE*, 8(10):e76171, 2013.

[144] Tom P. J. Wyatt, Andrew R. Harris, Maxine Lam, Qian Cheng, Julien Bellis, Andrea Dimitracopoulos, Alexandre J. Kabla, Guillaume T. Charras, and Buzz Baum. Emergence of homeostatic epithelial packing and stress dissipation through divisions oriented along the long cell axis. *Proc Natl Acad Sci USA*, 112(18):5726–31, 2015.

[145] S. A. Gudipaty, J. Lindblom, P. D. Loftus, M. J. Redd, K. Edes, C. F. Davey, V. Krishnegowda, and J. Rosenblatt. Mechanical stretch triggers rapid epithelial cell division through piezo1. *Nature*, 543(7643):118–121, 2017.

[146] Y. Mao, A. L. Tournier, A. Hoppe, L. Kester, B. J. Thompson, and N. Tapon. Differential proliferation rates generate patterns of mechanical tension that orient tissue growth. *EMBO J*, 32(21):2790–803, 2013.

[147] Loïc LeGoff and Thomas Lecuit. Mechanical forces and growth in animal tissues. *Cold Spring Harb Perspect Biol*, 8(3):a019232, 2016.

[148] Georgina C. Fletcher, Maria-del-Carmen Diaz-de-la Loza, Nerea Borreguero-Muñoz, Maxine Holder, Mario Aguilar-Aragon, and Barry J. Thompson. Mechanical strain regulates the hippo pathway in drosophila. *Development*, 145(5):dev159467, 2018.

[149] Yuanwang Pan, Herve Alégot, Cordelia Rauskolb, and Kenneth D. Irvine. The dynamics of hippo signaling during drosophila wing development. *Development*, 145(20):dev165712, 2018.

[150] E. Marinari, A. Mehonic, S. Curran, J. Gale, T. Duke, and B. Baum. Live-cell delamination counterbalances epithelial growth to limit tissue overcrowding. *Nature*, 484(7395):542–5, 2012.

[151] Laura Wagstaff, Maja Goschorska, Kasia Kozyrska, Guillaume Duclos, Iwo Kucinski, Anatole Chessel, Lea Hampton-O/'Neil, Charles R. Bradshaw, George E. Allen, Emma L. Rawlins, Pascal Silberzan, Rafael E. Carazo Salas, and Eugenia Piddini. Mechanical cell competition kills cells via induction of lethal p53 levels. *Nat Commun*, 7:11373, 2016.

[152] Romain Levayer, Carole Dupont, and Eduardo Moreno. Tissue crowding induces caspase-dependent competition for space. *Curr Biol*, 26(5):670–677, 2016.

[153] M. Uyttewaal, A. Burian, K. Alim, B. T. Landrein, D. Borowska-Wykret, A. Dedieu, A. Peaucelle, M. Ludynia, J. Traas, A. Boudaoud, D. Kwiatkowska, and O. Hamant. Mechanical stress acts via katanin to amplify differences in growth rate between adjacent cells in arabidopsis. *Cell*, 149(2):439–451, 2012.

[154] M. Delarue, J. F. Joanny, F. Jülicher, and J. Prost. Stress distributions and cell flows in a growing cell aggregate. *Interface Focus*, 4(6):20140033, 2014.

[155] M. Delarue, F. Monte, D. Vignjevic, J. Prost, J. F. Joanny, and G. Cappello. Compressive stress inhibits proliferation in tumor spheroids through a volume limitation. *Biophys J*, 107(8):1821–1828, 2014.

[156] Alessandro Taloni, Martine Ben Amar, Stefano Zapperi, and A. M. Caterina La Porta. The role of pressure in cancer growth. *The European Physical Journal Plus*, 130(11):1–10, 2015.

[157] J. J. Winkle, O. A. Igoshin, M. R. Bennett, K. Josic, and W. Ott. Modeling mechanical interactions in growing populations of rod-shaped bacteria. *Phys Biol*, 14(5):055001, 2017.

[158] M. Delarue, J. Hartung, C. Schreck, P. Gniewek, L. Hu, S. Herminghaus, and O. Hallatschek. Self-driven jamming in growing microbial populations. *Nat Phys*, 12(8):762–766, 2016.

[159] Antoine Fruleux and Arezki Boudaoud. Modulation of tissue growth heterogeneity by responses to mechanical stress. *bioRxiv*, 2018.

[160] L. D. Landau and E. M. Lifshitz. *Theory of elasticity*. Butterworth-Heinemann, 1986.

[161] Witold Nowacki. *Thermoelasticity (Second Edition)*. Pergamon Press, 1986.

[162] N.G. Van Kampen. *Stochastic Processes in Physics and Chemistry*. Elsevier Science, 2011.

[163] Nicholas E. Baker. Mechanisms of cell competition emerging from drosophila studies. *Curr Opin Cell Biol*, 48:40–46, 2017.

[164] G. Mitchison. Conformal growth of arabidopsis leaves. *J Theor Biol*, 408:155–66, 2016.

[165] K. Alim, S. Armon, B. I. Shraiman, and A. Boudaoud. Leaf growth is conformal. *Phys Biol*, 13(5):05LT01, 2016.

[166] C. Blanch-Mercader, J. Casademunt, and J. F. Joanny. Morphology and growth of polarized tissues. *The European Physical Journal E*, 37(5):1–11, 2014.

[167] Reza Farhadifar, Jens-Christian Röper, Benoit Aigouy, Suzanne Eaton, and Frank Jülicher. The influence of cell mechanics, cell-cell interactions, and proliferation on epithelial packing. *Curr Biol*, 17(24):2095–2104, 2007.

[168] Takashi Koyama, Marisa A. Rodrigues, Alekos Athanasiadis, Alexander W. Shingleton, and Christen K. Mirth. Nutritional control of body size through foxo-ultraspiracle mediated ecdysone biosynthesis. *eLife*, 3:e03091, 2014.

[169] B. C. Stieper, M. Kupershtok, M. V. Driscoll, and A. W. Shingleton. Imaginal discs regulate developmental timing in drosophila melanogaster. *Dev Biol*, 321(1):18–26, 2008.

[170] Daniel T. Gillespie. The chemical langevin equation. *The Journal of Chemical Physics*, 113(1):297–306, 2000.

[171] Milton Abramowitz and Irene A. Stegun. *Handbook of Mathematical Functions with Formulas, Graphs, and Mathematical Tables*. Dover Publications, 1972.

[172] D. S. Jones. *The Theory of Generalised Functions*. Cambridge UP, 1982.